UNIVERSITY OF CASSINO AND SOUTHERN LAZIO

DOCTORAL THESIS

Multiscale Study of Ductile Cast Iron by Numerical Method

Author:
Ehsan KHADEMI

Supervisor:
Dr. Nicola BONORA

A thesis submitted in fulfillment of the requirements for the degree of Doctor of Philosophy

in the

Mechanical engineering
Department of civil and mechanical engineering

February 26, 2023

Abstract

Ductile Cast Irons (DCIs), because of their material characteristics, are increasingly being considered as an alternative to cast, forged, and welded steels for structural applications. In this thesis, an integrated multiscale numerical study is performed on different DCIs to obtain material properties at the higher scale, the continuum scale where the material can be seen as homogeneous, and the lower scale, in this case, the microscale where the dispersed nodules can be distinguished from the matrix. Numerical analysis is performed using the finite element method. To make up for the lack of information on the physical-thermomechanical properties of the constituents, the available literature data were integrated with the results obtained from the CALPHAD methodology applied to both the cast iron and steel that make up the matrix. For the macroscale study, a pressure-dependent material model with a non-associated flow rule is proposed for DCI. The model is calibrated to provide satisfactory results with both uniaxial tensile test and cylinder compression experiments. The local stress and strain tensors at the integration points and the gradient of deformation are recorded to calibrate the matrix and nodule materials.

The micromechanical approach, which takes advantage of the composite nature of DCIs, has established itself over the years as a tool for analyzing their behavior. This approach is based on the definition of a representative volume element (RVE), which corresponds to the smallest volume of material that can reproduce the properties of DCI. For the definition of RVE to be effective, all microstructural aspects that influence the overall behavior must be modeled appropriately. These certainly include the volume fraction, the constitutive response of the components, and the behavior of the nodule-matrix interface.

In the local residual stress calculations, the behavior of the nodule was assumed to be linear elastic because of the low stresses to which it is subjected during cooling. For the matrix, on the other hand, elasto-plastic-viscous behavior was assumed considering both the primary and secondary creep regimes. To fully exploit the potential of the micromechanical approach, progressively more refined models have been developed to consider the various mechanisms involved in the solidification process. In this context, the effect of viscous creep, which occurs in the early part of the solidification process, on the state of residual stresses, accumulated inelastic deformations, and the macroscopic stress-strain response is analyzed.

This thesis is mainly devoted to characterizing the mechanical properties of the nodule, especially at high strain levels. To calibrate the RVE, local loading conditions of the macroscale model are selected where, in the presence of large deformations, the stress state is complex. To impose these conditions on the micro model, displacements of RVE boundaries are calculated based on the deformation gradient of the macro model. In this way, the same strain state is created at both scales. Numerical analysis shows that nodule behavior under compressive conditions is a function of pressure. Therefore, a pressure-dependent material model is assumed for the nodule. Through optimization, unknown material constants are calculated to provide a satisfactory agreement between the stress field of the RVE and that of the macro medium. In addition, the morphology of the nodule in various strain states is investigated.

To verify the functionality of the proposed constitutive models and the validity of the assumptions, two different DCI materials are considered. The Comparison between the predictions of the numerical model and experimental results in the literature demonstrates the effectiveness of the applied methodology.

Acknowledgements

First, I would like to express gratitude to my supervisor, Prof. Nicola Bonora, for giving me the opportunity to do high-level research at Cassino and Southern Lazio University. My special appreciation is dedicated to Prof. Andrew Ruggiero for defining the research plan and for his continuous support, he had always been a great resource of concrete related knowledge without whom I wouldn't be able to tackle most of the numerical and theoretical problems faced with. I want to thank Prof. Gianluca Iannitti and Prof. Gabriel Testa for their guidance and helpful advice, especially on simulation problems.

I have been fortunate to meet some incredible people at Cassino and Southern Lazio University. Laura Morone, thank you for all the support and attempts you performed for me and for solving the residence problems of my family. You are one of the most professional people I've ever met who resolves students' problems like a family member. Prof. Wilma Polini and Prof. Fabrizio Marignetti for the careful and expert coordination of the Ph.D. program.

Finally, I want to thank my wife, Hedieh, and our daughter Kimia who were always pushing and motivating me. Their accompaniment as a family was my biggest motivation to overcome any problems and without them, this Ph.D. literally would have never started.

Contents

List of Figures

List of Tables

Chapter 1

Introduction

1.1 Ductile cast iron

Cast irons are Fe-C alloys containing 2.4 to 4 in weight percentage (wt%) of carbon (Cottrell, 1995). They consist of different amounts of elements such as Si, Mo, Mn, P, S, Ti, Sb, and Sn and identify a large family of ferrous alloys
The high carbon content of cast irons provides graphite inclusions in the microstructure surrounded by a ferrite/pearlite matrix. The morphology of the graphite inclusions plays a key role in the mechanical and thermal properties of cast irons (H.T. Angus, 1976). Depends on the chemical composition and casting parameters such as cooling rate, three types of graphite inclusions are observed in the microstructure of cast iron: flake graphite, nodular graphite and compacted graphite (Fig. 1.1).

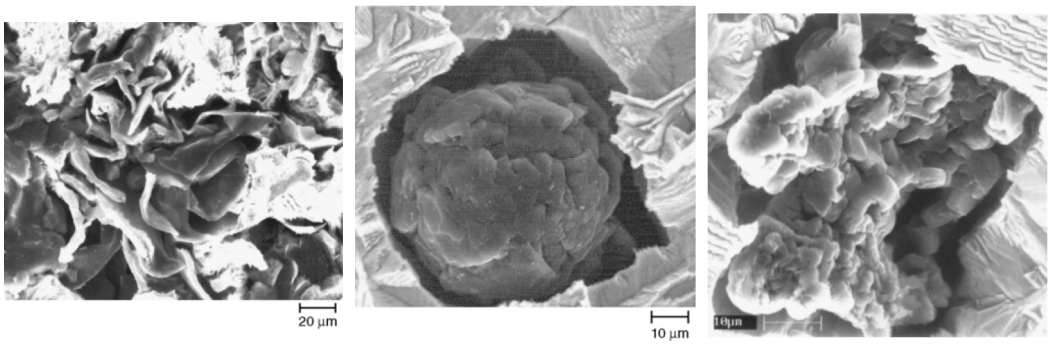

(a) Flake graphite (b) Nodular graphite (c) Compacted graphite

FIGURE 1.1: Different graphite morphology in cast irons (Vander Voort and Buehler Ltd., 2004)

The addition of a small amount of magnesium to the cast iron melt in the ladle causes the graphite to precipitate as nodules rather than flakes. Nodular cast iron is widely known as Ductile Cast Iron (DCI). Other elements such as silicon and nickel are also added to improve the strength and elongation of DCIs. Nodule dimensions and shape perfection vary depending on the composition and cooling rate. Fig. 1.2 shows as-polished surface of as cast ductile iron with maximum nodule diameter of 100 µm.

Because of their good mechanical properties and excellent casting and machining performances, DCIs are increasingly being considered as an alternative to cast, forged and welded steels for structural applications, (Zanardi, Mapelli, and Barella, 2020). Today, DCIs are used

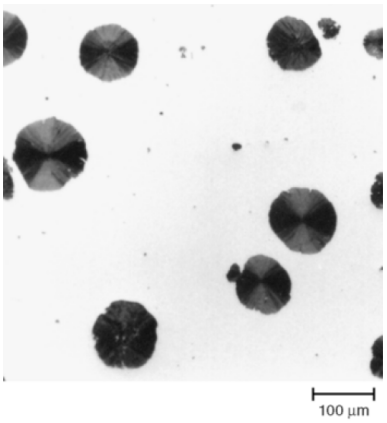

FIGURE 1.2: Ductile cast iron (microscopic examination 100x)

in the construction of: pressure pipes, motor vehicles, farm machinery, engines, pumps and compressors, valves and fittings, metalworking machinery, construction machinery. Other important markets include: textile machinery, wood working and paper machinery, mechanical power and transmission equipment, motors and generators, refrigeration and heating equipment and air conditioning.
Their properties are strongly influenced by: varation in the balance between elements like carbon and silicon, alloying with different metallic and non-metallic elements and varation in casting, melting and heat treatment choices. They can range from a structure characterized by high ductility and impact toughness, as in EN-GJS-350 grade, to pearlitic structures with high strength and hardness, as in EN-GJS-900 grade, (Collini and Pirondi, 2020). Over the years, new classes of high-performing DCIs are continuously being developed and made commercially available. Examples include Austempered Ductile Irons (ADIs) with their strength-to-weight ratio exceeding that of aluminum, (Keough, Hayrynen, and Pioszak, 2010), or the new grades of Si-alloyed DCIs, with increased strength and improved machinability, introduced in the European Standard EN 1563:2012, (Zanardi et al., 2017).

1.2 Multi scale study of DCI

In an arena where optimizing the performance of DCIs is under continuous development, the availability of tools to predict their mechanical behavior is useful to both foundry engineering and design.

1.2.1 Macromechanical approach

Some microstructural features like graphite morphology and volume fraction are considered by researchers to study the macroscopic response of ductile cast irons (Mukherjee et al., 2017; Ruggiero et al., 2018; Steglich and Brocks, 1998; González-Martínez et al., 2018; Hervas, Thuault, and Hug, 2015). For instance, Hervas et al. performed compression tests on cylindrical samples of (silicon, molybde- num) SiMo DCI, to investigate nodule shape evolution during compression in presence of complex stress states(Hervas et al., 2013). They also experimentally measured the compressive and tensile true stress–strain curves of the material in different temperatures. In the case of ductile cast iron, the heterogeneous and

multifaceted microstructure, is a challenge for the comprehension and prediction of its behavior.

1.2.2 Micromechanical approach

Micromenchanical approach to analyze the behavior of DCIs, which takes advantage of the composite nature of the material, has become established over the years, (Brocks, Hao, and Steglich, 1996; Steglich and Brocks, 1997; Bonora and Ruggiero, 2005; Andriollo, Thorborg, and Hattel, 2016; Pereira et al., 2018). In such an approach, the behavior of cast iron is obtained as a result of that of its constituent materials and is therefore particularly suited to assessing the effect of individual microstructural aspects on the overall response.

A Representative Volume Element (RVE) has to be defined at the microscale, in this case the scale at which the dispersed nodules can be distinguished from the matrix, capable of reproducing the properties of the material at the macroscale, the scale of the continuum where the material can be seen as homogeneous. In this definition, all microstructural aspects that influence the global behavior must be appropriately modeled. Among these are certainly to be considered: volume fraction, constitutive response of components, and behavior of nodule–matrix interface.

1.2.3 Local residual stress

In relation to the nodule–matrix interface, since there is no chemical bond between the two components, the most widespread doctrine considers an interaction of pure mechanical nature between them. Bonora and Ruggiero, (Bonora and Ruggiero, 2005), hypothesized that the mechanical interface forces are constituted by the residual stresses generated during the solidification of the DCI due to the mismatch between the thermal expansion coefficients of nodules and matrix. In the same work, for a ferritic cast iron, the residual stresses were calculated by simulating cooling process from the temperature of 1000°C, at which the matrix is considered stress free, to room temperature.

Zhang et al. (Zhang et al., 2016; Zhang et al., 2019), by means of Differential-Aperture X-ray Microscopy (DAXM), measured both local plastic and elastic residual strains in both metal and sand mold DCIs. The results, which confirm the presence of residual stresses, suggest that they cannot be neglected in the analysis of the mechanical behavior of DCI especially in facing applications involving fatigue where their role is of primary importance. In this regard, Krasowsky et al. (Krasowsky, Kramarenko, and Kalaida, 1987), by neutron diffraction monitoring of DCI under cyclic loading, demonstrated that as stress increased, the graphite inclusions promoted the nucleation of microcracks, but the residual compressive stresses surrounding them locally retarded fatigue crack growth.

Numerous studies have addressed the quantification of local residual stresses in DCI and the analysis of their effect on global behavior by pursuing increasing levels of refinement in finite element modeling of the RVE. Iannitti et al. (Iannitti et al., 2017) modeled RVE considering a random dispersion of nodules that reflected the actual distribution measured in an ADI JS/1050-6. Andriollo et al. (Andriollo et al., 2019), using X-ray data, modeled the full microstructure between two sections of a miniaturized DCI specimen and directly applied as boundary conditions the displacement field reconstructed by digital volume correlation.

1.2.4 Mechanical behavior of RVE constituents

- Local residual stress calculation

Another relevant aspect is the appropriate description of the mechanical behavior of the RVE constituents over the whole temperature range spanned in the simulation of the cast iron manufacturing process. The development of plastic strain, confirmed by measurements in (Zhang et al., 2016), affects the resulting residual stress state by relaxation. Thus, correctly quantifying the amount of inelastic deformation is crucial. In this regard, Andriollo et al. (Andriollo et al., 2018), simulating solidification, considered among the different mechanisms also creep by adopting Peric's model.

Clearly, refined models that aim to exploit the full potential of the micromechanical approach must take into account the various mechanisms involved in the solidification process. However, a major limitation to their applicability lies in the lack of data on the physical-mechanical properties of the constituents at different temperatures.

The first problem is the unavailability of constituent materials for experimentation. Some attempts have been made to obtain a steel with the same microstructure as the matrix of the considered cast iron, e.g. the ferritic steel manufactured in (Andriollo et al., 2018). However, if with some limitations it can be done for the matrix, to date it is not possible to obtain the graphite that makes up the nodules as a stand-alone material. Secondly, even in the event that the correct material is available, performing a complete characterization, especially at high temperatures, can be extremely complicated and, when possible, very expensive.

- Large strain deformations

Literature review reveals that less attention has been paid to presenting reliable models for RVE constituents to predict large strain deformations of DCI. The Matrix is a type of ferritic/pearlitic steel alloy. The mechanical behavior of steel alloys have been well investigated by the researchers over the years. But the properties of nodules, especially under large strain deformation, has been neglected.

A scoping review shows that the study of the mechanical behavior of nodules has been mainly limited to elastic deformation (Speich, Schwoeble, and Kapadia, 1980; Collini and Nicoletto, 2005; Bonora and Ruggiero, 2005; Pereira et al., 2018). Furthermore, the proposed elastic constants are placed in a wide range (Andriollo, Thorborg, and Hattel, 2016). Although (Andriollo et al., 2018) adopted an elasto-plastic model with six constants, the assumed inelastic strains are negligible and only suffice to describe the local residual stresses during manufacturing of DCI. Recently, Anderiollo et al. (Andriollo et al., 2019) in addition to common elastic model, assumed an elastic-perfect plastic behavior for the nodule, but at least for tensile tests, their results show no advantage.

1.2.5 Scope and objectives

It was discussed in the previous section that reliable constitutive models to describe properties of nodule and matrix of DCIs are a challenge. This thesis will focuses on multiscale study of DCIs, both at the macro and micro scales, to present constitutive models for DCI and its components: the matrix and the nodule. To overcome the limitations that were mentioned in the previous section, the physical and mechanical properties of the materials of interest were estimated by integrating literature data with predictions from a computational

code. Specifically, the commercial code JMatPro (Java-based MATerials PROperties) was adopted. This uses the CALPHAD methodology (CALculation of PHAse Diagram (Kaufman and Bernstein, 1970)) to model the thermodynamic properties of the expected phases in the multicomponent alloy and, from these, determine the thermodynamic of the alloy. Then, based on proprietary databases, the code correlates the calculated thermodynamic properties to the physical-mechanical properties of the alloy, (Saunders et al., 2003).
The objectives of the thesis and the strategies adopted are as follows:

1- Introduce the constitutive model of the DCI and extract local stresses and strains.
For the macroscale study, the considered loading conditions are a uniaxial tensile test and a cylinder compression test on the DCI material. To define the constitutive model, the Finite Element (FE) method is used. By inverse calibration and using multi-objective optimization, the constants of the material model are calibrated. Finally, the local gradient of deformation is recorded to be used in the next step.

2- Proposing constitutive model for nodule.
The main goal of the thesis is to define the properties of the nodule. To do so, micromechanical approach using the FE method is considered. First, RVE composed of a nodule and matrix is created to represent the DCI material. By integrating the data available in the literature and using inverse calibration, the RVE is calibrated to provide the best match with the local gradient of deformation in compression (calculated in the previous step) and the tensile test results. The inverse calibration is performed by multi-objective optimization and after considering different models, the appropriate model for nodule is selected and its constants are calculated.

3- Calculation of the local residual stress in DCI.
To obtain thermo-mechanical behavior of the matrix, JmatPro code is used. A creep model is proposed for the matrix material and the model is calibrated based on the experimental data. RVE is used to calculate the local residual stresses in the DCI by simulating the cooling process.

4- Investigation of the functionality of the proposed models.
The calculated local residual stresses and nodule morphology are compared with the experimental evidences for different DCI materials.

1.2.6 Summary of the thesis

In this thesis, the numerical analysis is performed using the finite element method. Below is a brief summary of the structure of the thesis:

- Chapter 1 – Introduction

The first chapter provides a brief introduction to the problem, a review of the literature, and the objectives and scope of the thesis.

- Chapter 2 – Macromechanical study

The second chapter, is devoted to the macro scale study of the DCI. Two different FE models are considered to simulate compression of cylinder and uniaxial tensile loading. A non-associated pressure dependent material model is selected for DCI to provide the best match with experiments. The material model is implemented in the FE package by considering multiplicative approach. Constants of the material model are optimized for the following

objectives: true stress-strain curve in the uniaxial tensile test, load-displacement curve in cylinder compression test, and deformed shape of the cylinder. For optimization, a genetic algorithm is used through Dakota code. A python script is prepared to record gradient of deformation and stress tensor at the desired integration points.

- Chapter 3 – Micromechanical study: RVE

The remaining part of the thesis includes micromechanical study of DCI. The characteristics of the RVE are discussed in the third chapter. RVE is modeled by a simple cube with a spherical nodule in the center. Two different meshes are considered, one with corresponding nodes on the interface between the nodule and the matrix and the other with a finer element size. The former to avoid difficulties due to separation in the tensile test and the latter to avoid exaggerated distortion of the elements in the cylinder compression. Periodic bouandary condition is defined by introducing three auxiliary nodes outside the mesh. The homogenization technique for the stress and strain measurements is performed by a python script.

- Chapter 4 – Micromechanical study: local residual stresses

The fourth chapter is allocated to the calculation of the local residual stresses. Another grade of DCI is selected based on the local residual stress measurements available in the literature. The solidification of DCI and its matrix is executed by JMatPro. During solidification, the mechanical and physical properties of the matrix such as the coefficient of thermal expansion (CTE), elastic constants and flow stress are calculated by the code. The starting temperature of the cooling is selected by analyzing phase changes of the DCI and matrix. An elastic model is considered for the nodule due to its trivial deformation during cooling. The elastic properties of the nodule are calculated by mean field theory, knowing elastic properties of the matrix (from the CALPHAD calculation) and of the DCI (for its grade). The evolution of the nodule's CTE with temperature is assumed to be similar to isotropic graphite. A general creep model is presented by considering primary and secondary creep. The constants of the creep model are calibrated based on creep tests on a matrix like material. Manufacturing of the DCI is simulated by cooling the RVE from the assumed starting temperature to room temperature. Finally, the numerical results are compared to the experiments.

- Chapter 5 – Micromechanical study: nodule characteristics

In the fifth chapter, inverse calibration of nodule properties and the study of the RVE response under different loading conditions are dedicated. Here, DCI is the material that was used in the second chapter. For matrix of DCI, solidification is simulated by JMatPro. Therefore, the matrix properties and starting temperature for cooling are calculated by CALPHAD method. The nodule properties have been presented previously, but in this chapter, the nodule deformation exceeds the elastic limit. Therefore, a pressure dependent material model is presented for nodule strength. In the numerical analysis, RVE undergoes thermomechanical loading during cooling and then continues with pure mechanical loading at room temperature. During mechanical loading, RVE strains are adjusted to match the desired local strains at the macro scale. The RVE is calibrated to have the best match with the objectives. Here, the objectives are the uniaxial tensile test and the local stress state that formerly was calculated for specific integration points in the second chapter. Therefore, the unknown material constants are obtained by inverse calibration of the micro-model. Finally, the morphology of the nodule in various level of deformation is investigated.

- Chapter 6 – Conclusion

A conclusion of the thesis as well as highlighted findings of the research are explained in the sixth chapter. Also, some topics for future works are proposed.

Chapter 2

Macromechanical study

2.1 Material

The material considered for investigations is a ferritic (silicon, molybdenum) SiMo DCI that was analyzed by Hervas et al. (Hervas et al., 2013) and will be called DCI Hervas in this thesis. Its chemical composition is shown in Table 2.1. The average size of ferritic grains is 10.0 µm while 10% in volume of perlite is observed close to rich molybdenum carbides.

TABLE 2.1: Chemical composition of the DCI (in wt.%), Fe: balance.

Si	C	S	Mg	Mn	Cr	Mo	Sn	Cu	P
4.240	3.000	0.005	0.028	0.220	0.070	0.610	0.009	0.020	0.020

The commercial code JMatPro was use to extract additional information about the DCI microstructure. A pealitic-ferrite mixture was selected as DCI alloy, then, the graphite content was iteratively changed in order to obtain phases fractions reported in Table 2.2. Solid fractions variation of DCI during cooling is shown in Fig. 2.1. For the temperatures lower than 805°C the mass fraction of graphite remains unchanged and it can be assumed that micro-structure does not vary. Since, pearlite is a two-phased, lamellar (or layered) structure composed of alternating layers of ferrite (87.5 wt%) and cementite (12.5 wt%), obtained fractions correspond to a perlite volumetric fraction of 10.99%, that is consistent with experimental measurement.

TABLE 2.2: Volume and weight fractions of DCI phases.

	vol%	wt%
Graphite	8.87	2.85
Ferrite	89.0	95.0
Cementite	1.35	1.47
M6C	0.978	0.998
MGS	0.0235	0.0089

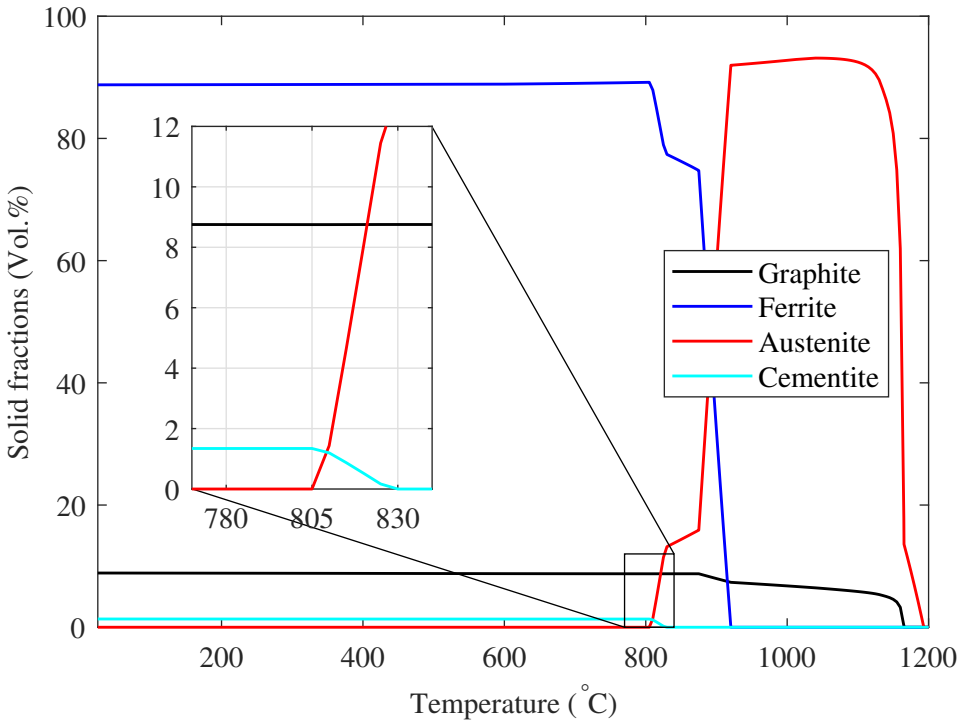

FIGURE 2.1: Variation of DCI Hervas phases in Vol% with temperature

2.2 Numerical study

2.2.1 Loading conditions

For the macromechanical study of DCI behavior at room temperature, two different loading conditions are considered:

- Compression of a cylinder of 5 mm diameter and 10 mm height
- Uniform uniaxial tension

For compression, the specimen geometry and experimental results are adopted from the work of Hervas et al. (Hervas et al., 2013). In their test, the punch compresses the cylinder and the load is stopped while the height of the sample reduces to 5 mm.
For tension, in order to compare numerical results with experiments, the tensile test performed by Hervas et al. (Hervas, Bettaieb, and Hug, 2013) is considered.
Both conditions are assumed to evaluate the mechanical behavior of the material not only in negative triaxiality but also in positive hydrostatic stress.

2.2.2 Constitutive model

DCI in macro medium is assumed to be heterogeneous composite of nodules and matrix. Since the graphite nodules are distributed randomly throughout the matrix and ferrite matrix properties do not vary with direction, on macroscale, the DCI can be simply modeled as homogeneous material. Also, isotropic behavior can be presumed for its mechanical properties.

For the Young's modulus of DCI, due to the continuous nonlinear variation of stress with strain, even at elastic deformation, a range of 162 GPa to 176 GPa is found in the literature. Also, they suggest a narrow variation of Poisson's ratio between 0.275∼0.28 (Ductile Iron Society, 1990; American Foundrymen's Society, 1993; Andriollo, Thorborg, and Hattel, 2016; Andriollo et al., 2016; Kohout, 2001; H.T. Angus, 1976; Speich, Schwoeble, and Kapadia, 1980). Therefore, the Young's modulus of 170 GPa can be selected for the under study material in agreement with experimental findings (Hervas, 2013). In addition, due to the similarities between the microstructure and composition of this material and DCI Zhang, that will be studied in the sections 4.3, the Poisson's ratio of 0.28 is presumed. More details about this decision will be dedicated in the mentioned section.

It is important to obtain reasonable yield function for the DCI. Although the use of the von Mises criterion simplifies the problem, at the same time it leads to errors in the predicting of the material behavior . For instance, researchers like Ruggiero el al. have proposed a pressure dependent model for austempered ductile irons under different stress triaxialities in tensile loading, based on experimental findings (Ruggiero et al., 2018). Moreover, due to the fact that von Mises model does not take the stress triaxiality into account, if experimental tensile stress-strain curve is considered for obtaining material constants, the predicted response of the material in compression may be unreliable. To overcome this problem, the following pressure dependent yield function is selected (Drucker and Prager, 1952):

$$\Phi = \sqrt{J_2} + \eta\sigma_h - \frac{\bar{\sigma}}{\sqrt{3}} \tag{2.1}$$

where σ_h is hydrostatic stress, J_2 is second invariant of deviatoric stress tensor and $\bar{\sigma}$ denotes yield strength. η represents the dependency of J_2 to the pressure and for von Mises model is zero. As a consequence of Eq. 2.1 plastic strains are accompanied by increase in volume if $\eta \neq 0$. In some cases this volume increase is not desirable and non-associated flow rule is adopted in return mapping stage:

$$\Psi = \sqrt{J_2} + \bar{\eta}\sigma_h - \frac{\bar{\sigma}}{\sqrt{3}} \tag{2.2}$$

In the macroscale, increase in volume was not seen in the experiments. Therefore, it is assumed that $\bar{\eta} = 0$ in the numerical analysis and volume constancy due to plastic deformation is respected. Regarding to the shape of stress-stress curve, the evolution of DCI yield strength with equivalent plastic strain ($\bar{\varepsilon}_p$) is introduced by Voce-type formulation with two terms:

$$\bar{\sigma} = \sigma_0 + B_1(1 + e^{-C_1\bar{\varepsilon}_p}) + B_2(1 + e^{-C_2\bar{\varepsilon}_p}) \tag{2.3}$$

where σ_0 is initial yield strength and B_1, C_1, B_2 and C_2 are material constants.

2.2.3 Finite element method

The finite element package MSC.MARC is used for numerical studies. Two different models are used for tensile and compressive loads.

For the uniaxial tension, because post-necking data was not presented in the experiment, single 4-node quadrilateral element with 4 integration point under axisymmetric conditions is used to obtain numerical true stress-strain curve.

The cylinder compression test is simulated with a three dimensional deformable cylinder that is compressed by a rigid punch. Eight-node eight-integration point isoparametric hexahedral elements are used to mesh the cylinder and a rigid surface geometry is selected for the punch. Due to the symmetry of the geometry and isotropy of the properties, one-eighth of the cylinder is studied to reduce the cost of the simulations. So, boundary conditions are defined to ensure the symmetry of the geometry and material flow. The geometry and mesh of the 1/8 of the cylinder compression simulation is shown in Fig. 2.2. The mesh is composed of 11020 elements. The height of the first eight upper layers is half that of the other layers because of the greater deformation of these regions. The contact between the punch and the cylinder is defined as a deformable-geometry touch condition while the friction for the sliding motion between the surfaces follows Coulomb's law. The coefficient of friction is another parameter that must be evaluated during the optimization phase. The compression is simulated by imposing the displacement to the punch in -z direction and its final value is selected 2.5 mm. This value leads to a nominal strain $\varepsilon_z = -0.5$ which is experimentally the limit of compression due to the failure of the sample.

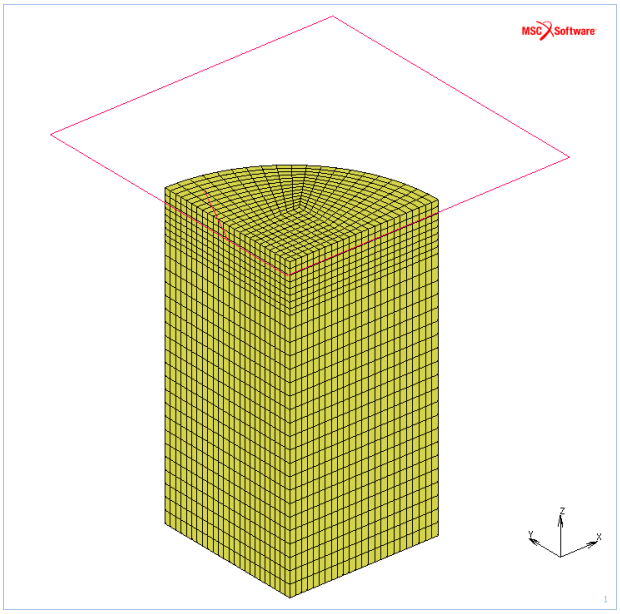

FIGURE 2.2: Designed geometry and mesh for macroscale study of DCI

The problem is solved incrementally under large strain hypothesis with updated Lagrange formulation using *multiplicative* formulation. Hypothesis of multiplicative decomposition of the deformation gradient, $\boldsymbol{F}$, assumes that:

$$\boldsymbol{F} = \boldsymbol{F}^e \boldsymbol{F}^p \tag{2.4}$$

where $\boldsymbol{F}^e$ and $\boldsymbol{F}^p$ are elastic and plastic part of deformation gradient respectively. A user material subroutine is prepared to update the stress and calculate tangent stiffness matrix at each integration point. The logarithmic strain measure is adopted for describing the deformation which is defined by:

$$\varepsilon = \ln \sqrt{\boldsymbol{F}\boldsymbol{F}^T} \tag{2.5}$$

The user material subroutine is implemented into the finite element package via *HYPELA2* routine and return mapping algorithm follows the procedure proposed by De Suoza Neto et al. (De Souza Neto, Perić, and Owen, 2008). In addition, the components of deformation gradient at each integration point are recorded as state variables for further microscale studies.

2.2.4 Optimization

The procedure for calibrating the macro-model to describe material behavior under different loading conditions is described in this section.

During the compression test, friction between the punch and cylinder surfaces creates trivially deformed areas called *dead zones*. As the punch moves downward, a slight deformation of the dead zones causes the specimen to barrel shape. For a predefined level of compression, the greater the friction between the surfaces, the greater the barreling phenomenon. Therefore, the coefficient of friction between the punch and the billet affects the final barrel shape of the sample and is one of the parameters that must be optimized. The other optimization parameters are the constitutive material constants of Eqs. 2.1 and 2.3 which define the mechanical behavior of the DCI material.
The optimization objectives are adopted from the cylinder compression test carried out by Hervas et al. (Hervas et al., 2013) with H/D (height/diameter) ratio equal to 2 and the results of tensile test of DCI (Hervas, Bettaieb, and Hug, 2013). In the tensile test, the objective is to obtain true stress-stain curve of the DCI. In the compression test, in addition to the load-displacement curve, the final shape of the sample is regarded an objective to capture the effect of the friction.
Therefore, it can be concluded that three optimization parameters and three objectives are assumed for calibrating the macro-model. Table 2.3 illustrates the features of the optimization.

TABLE 2.3: Optimization chractristics

Optimization	
Objectives	Parameters
Final shape of the sample at the end of compression	Coefficient of friction
Load-displacement curve during compression	Pressure coefficient, η, (Eq. 2.1)
True stress-strain curve in tensile test	True stress-strain constants (Eq. 2.3)

It should be emphasized that optimization parameters have coupled effects on the objectives. Therefore, they must be obtained simultaneously. Obviously, if the optimization parameters are calculated properly, the numerical results will be in agreement with the objectives.
The optimization is carried out by using DAKOTA package. A genetic algorithm method with a population size number of 20 is adopted for multi-objective optimizations. For each set of optimization parameters (selected by DAKOTA), difference between the objectives and the numerical results is defined as *error*. Then, the sum of squared errors is obtained

and fed into the code for further calculations. The optimization process continues until an acceptable error is achieved.

A suitable framework is prepared to run the optimization process automatically. Flow chart of the optimization stage is shown in the Fig. 2.3.

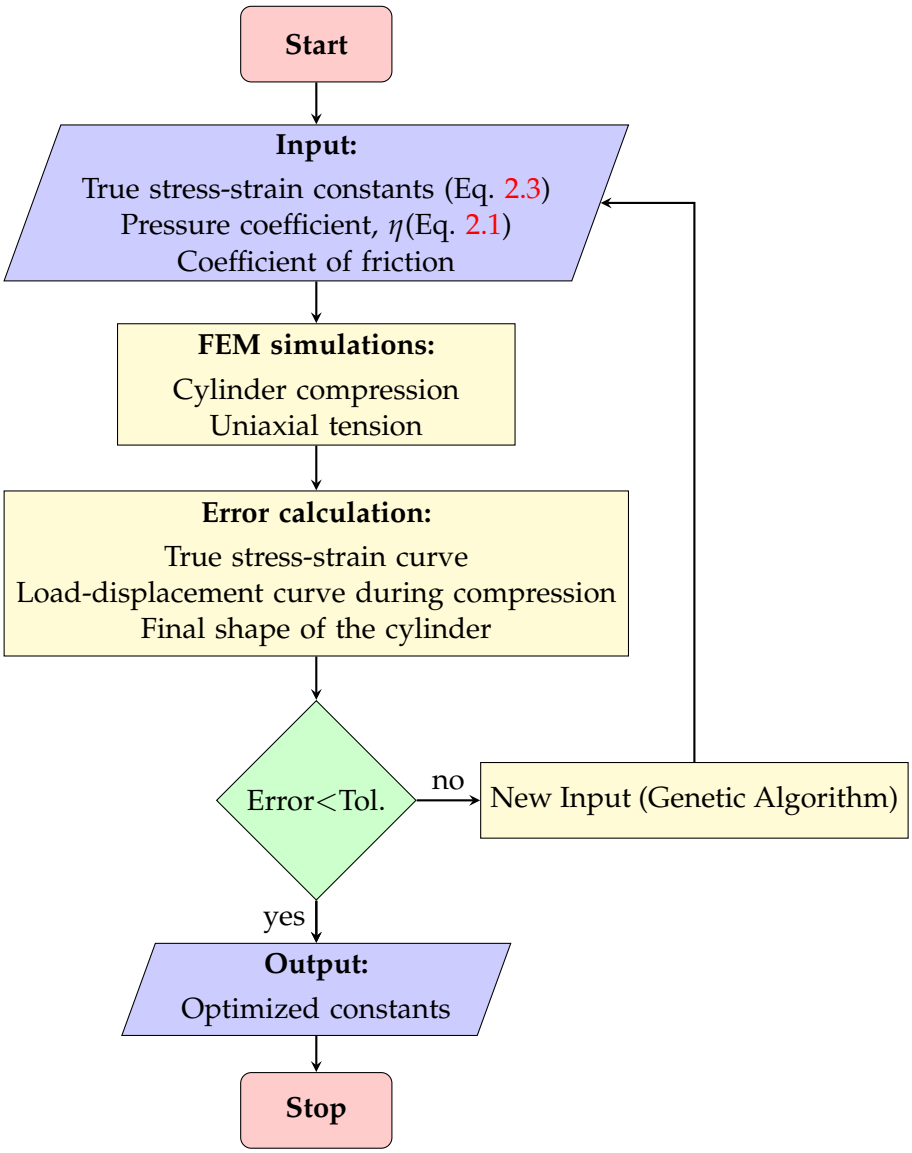

FIGURE 2.3: Flowchart of optimization procedure used for identification of DCI materials constants

First, DAKOTA determines a new set of optimization parameters from predefined ranges. The pre-processing step is performed by inputting this new set of parameters into the user subroutine HYPELA2 to define the material model in MSC. MARC. Then, the numerical solution is obtained by the FE code for the cylinder compression and simple tensile test.

For the post-processing step of compression simulation, a python script is written to calculate the error using the punch load and punch displacement at each increment as well asthe shape of the specimen at the end of compression. For tensile loading, another script is

used for calculating error between the FE results and the experimental tensile stress-strain data. At the end, these errors are reported to DAKOTA for new solutions. This procedure is repeated until the error is below the desired tolerance. All the mentioned steps are performed automatically.

In the optimization, a good initial guess can reduce the solution time and increase the possibility of obtaining reliable results. Due to the dry friction conditions in the test between the alumina punch and the cast iron billet, the initial value for the coefficient of the friction is selected 0.2 (J. Blau, 1992). Starting value for pressure coefficient, η, in Eq. 2.1 is chosen 0.058 (Ruggiero et al., 2018). Initial guesses for the constants in Eq. 2.3 are introduced by curve fitting to the experimental stress-strain tensile curve reported by Hervas et al. (Hervas, Bettaieb, and Hug, 2013) and are presented in Table 2.4.

TABLE 2.4: Initial guess for DCI stress-strain curve

σ_0 (MPa)	B_1 (MPa)	C_1	B_2 (MPa)	C_2
454.6	130.6	382.6	456.1	5.8

2.3 Results and discussions

The optimization results indicate that the coefficient of friction between the punch and the cylinder is 0.25. Calibrated parameters of the constitutive model are reported in Table 2.5

TABLE 2.5: Calibrated mechanical properties of DCI

Elastic constants		Yield criterion $\Phi = \sqrt{J_2} + \eta\sigma_h - \frac{\bar{\sigma}}{\sqrt{3}}$, $\Psi = \sqrt{J_2} + \bar{\eta}\sigma_h - \frac{\bar{\sigma}}{\sqrt{3}}$, $\bar{\sigma} = \sigma_0 + B_1(1 + e^{-C_1\bar{\varepsilon}_p}) + B_2(1 + e^{-C_2\bar{\varepsilon}_p})$						
E (GPa)	ν	η	$\bar{\eta}$	σ_0 (MPa)	B_1 (MPa)	C_1	B_2 (MPa)	C_2
170	0.28	0.058	0	474	130	390.5	396.4	6.93

The evolution of conventional stress (F/A_0) with conventional relative reduction ($\Delta L/L_0$) for the calibrated model during cylinder compression is compared with the experimental measurements in Fig. 2.4 where L_0, A_0, ΔL and F denote initial height, initial cross-sectional area, punch displacement and punch force, respectively. As shown in the graph, the calibrated model gives acceptable results from low to high compression level. Therefore, proposed pressure dependent constitutive model can reasonably predict material behavior. The study of the microstructure can reveal the cause of this pressure dependent behavior in the macro medium and will be discussed in the next chapter.

The final shape of the sample after compression is plotted in Fig. 2.5. Once again, the conformity between the numerical results and the experimental geometry of the sample confirms that the calibrated model can describe the deformation of the material. Moreover, the optimization of the friction coefficient allows to obtain a satisfactory correlation with the experimental observations. It should be noted that if ($\bar{\eta} \neq 0$) is selected, the volume

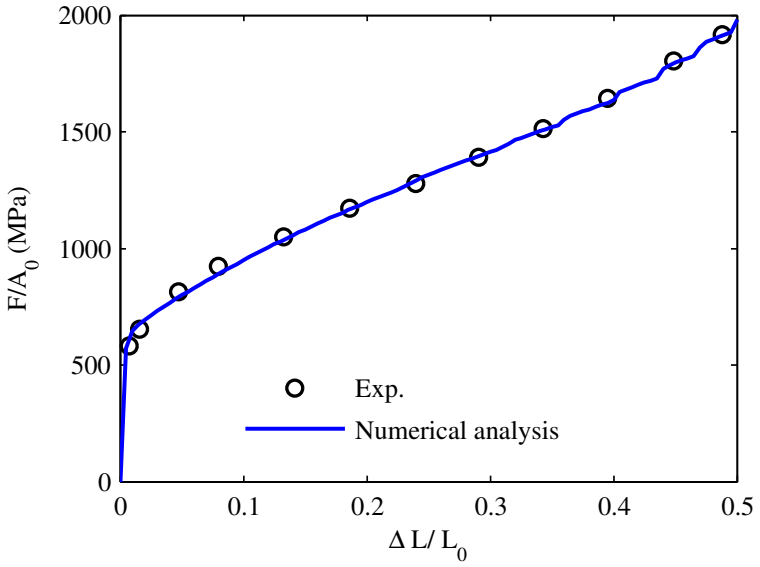

FIGURE 2.4: Conventional stress-relative reduction during compression

increases with the increase of plastic strains and consequently the final geometry will lose its agreement with the objective. Therefore, the assumption of a non-associative constitutive model without volume increase ($\bar{\eta} = 0$) is validated.

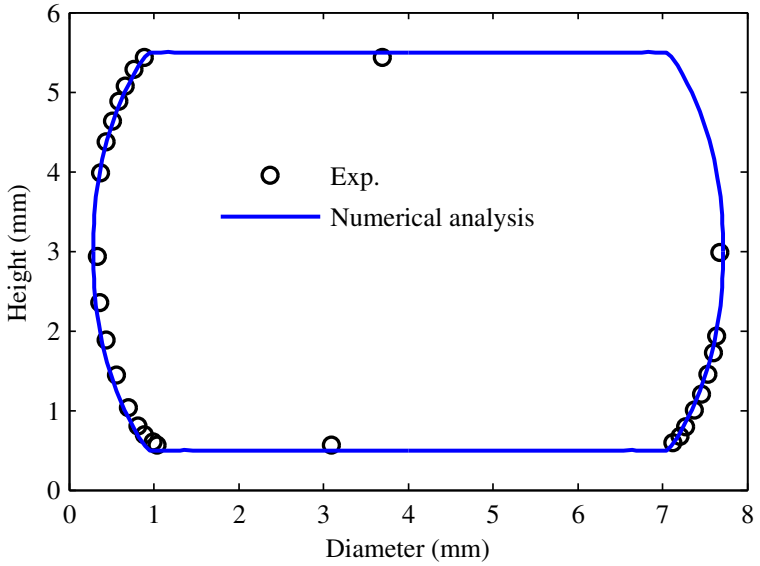

FIGURE 2.5: Sample geometry at the end of compression

True stress-stain curve of the calibrated macro-model under uniaxial loading is shown in Fig. 2.6. Once again, desirable compliance between the numerical solution and the experiment confirms that the proposed pressure dependent model is capable to describe DCI behavior not only under negative triaxialities but also under positive pressures. Furthermore, the model can be used for a wide range of deformation levels.

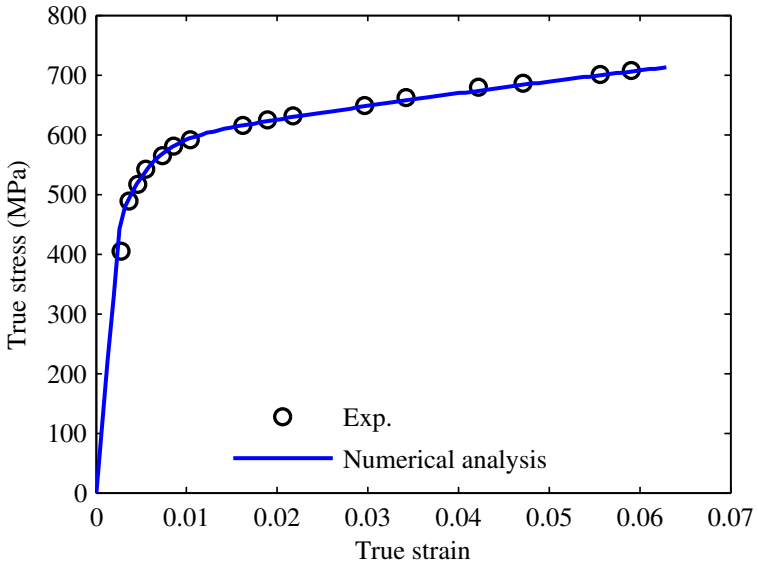

FIGURE 2.6: Uniaxial tensile stress-strain curve of DCI

The Sample shape and evolution of equivalent plastic strain (EQPLAS) during cylinder compression are shown in Fig. 2.7. As described in the section 2.2.4, friction between the punch surface and the sample creates dead zones with an insignificant amount of plastic strain that remains almost unchanged during compression. At the middle area of sample, plastic strain accumulates gradually and reaches to its maximum values at the end of compression. At the corner area EQPLAS localizes at the edge of the sample from the beginning and propagates toward the center as the compression proceeds.

Fig. 2.8 shows deformed sample at the $\Delta L/L_0 = 0.5$ where the upper half plots the contour of the equivalent plastic strain of the calibrated FE model and the lower half represents the experimentally measured nodule deformation (Hervas et al., 2013). It should be explained that they measured the nodule deformation by its aspect ratio, which is the ratio between major and minor diameters of the nodule. As figure illustrates, in the dead zone where the macro strains are negligible, deformation of nodules is not noticeable. In the middle and corners of the sample, where the material undergoes significant plastic strain, nodule deformation is also significant. It can be concluded that, at least in compression, the amount of nodule deformation is related to the amount of local strains in the macro medium. This will be considered when selecting specific locations in the macro medium for microscale studies.

2.4 Local study in compression test

It was described in section 2.3 that results of the numerical study are consistent with the experimental data and macro-model is calibrated acceptably. Therefore, a set of of useful data such as total strain, plastic and elastic strain, stress and gradient of deformation are available in each desired location in the macro-model. This local information can be used for studying mechanical properties of sub materials at the microscale.

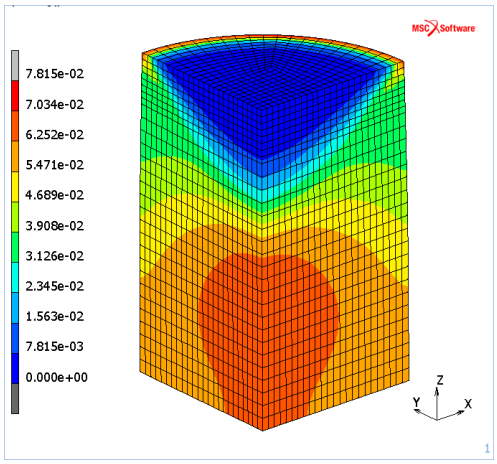

(a) $\Delta L/L_0 = 0.05$

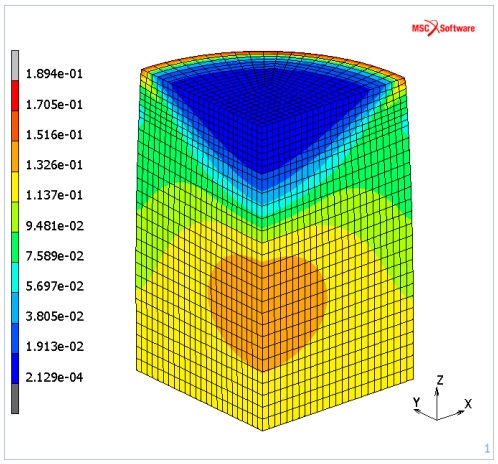

(b) $\Delta L/L_0 = 0.1$

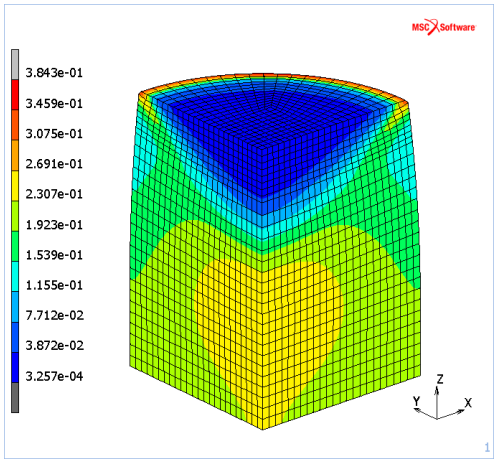

(c) $\Delta L/L_0 = 0.17$

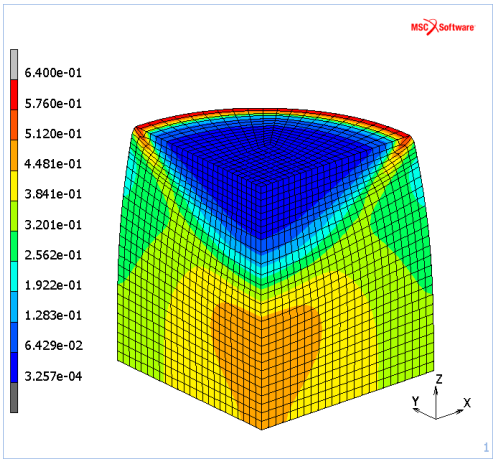

(d) $\Delta L/L_0 = 0.28$

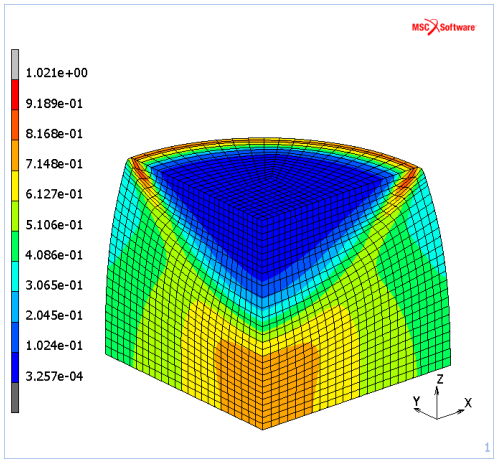

(e) $\Delta L/L_0 = 0.38$

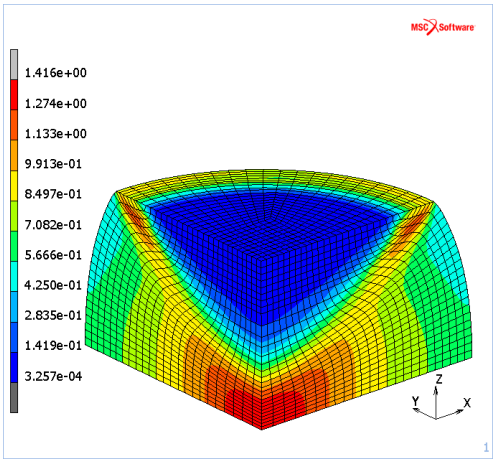

(f) $\Delta L/L_0 = 0.5$

FIGURE 2.7: Sample shape and evolution of equivalent plastic strain during cylinder compression

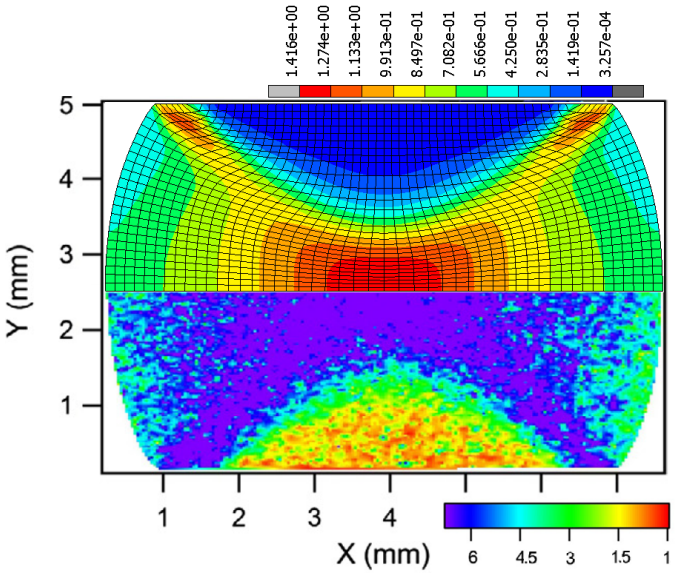

FIGURE 2.8: Deformed compression sample at $\Delta L/L_0 = 0.5$. Top: contour of EQPLAS in FE model and bottom cartography of nodule aspect ratio (Hervas et al., 2013)

For the macro-model under compression, due to the different local deformation and stress state in the sample, three areas are selected:

- Dead zone
- Middle area
- Corner area

In the FE model, first integration point of elements 2, 10681 and 18 are picked for dead zone, corner area and middle area respectively. Fig. 2.9 shows the position of the selected locations.

The Change in triaxiality factor (T.F.) and EQPLAS of the selected point in the dead zone during compression is plotted in Fig. 2.10a while triaxiality factor is defined as (T.F. $= \sigma_h/\sqrt{3J2}$). This point is located in the dead zone and does not experience significant deformation during compression as discussed previously in section 2.3. Therefore, its equivalent plastic strain is very small. Its T.F. starts with a very low value of -0.69 (compared to uniaxial compression which is T.F.= -0.33) and evolves to -0.26 at EQPLAS of 0.00134. The very low deformation with non-constant T.F. creates a more complex loading condition than simple uniaxial compression. Therefore, this point may be ideal for calibrating the micro-model under elastic condition and, consequently studying the elastic properties of its contents.

Fig. 2.10b shows the evolution of the EQPLAS and T.F. for selected locations in the middle of the sample during compression. As the figure indicates, for the middle area, T.F. varies in the range of -0.35 to -0.33 for the EQPLAS less than 0.35. This is very close to the uniaxial compression condition and at least simplifies the loading condition in the initial attempts for finding micro-model properties in presence of plastic deformation. As the compression continues, the T.F. decreases sharply to less than -0.8, showing a complex stress state even at the center of the sample for a high compression level. This point experiences a very high

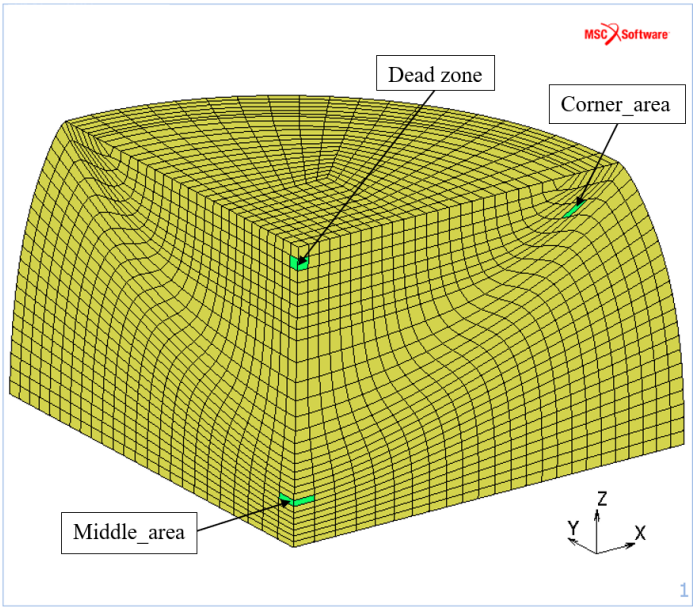

FIGURE 2.9: Location of selected points in the compression sample at $\Delta L/L_0 = 0.5$

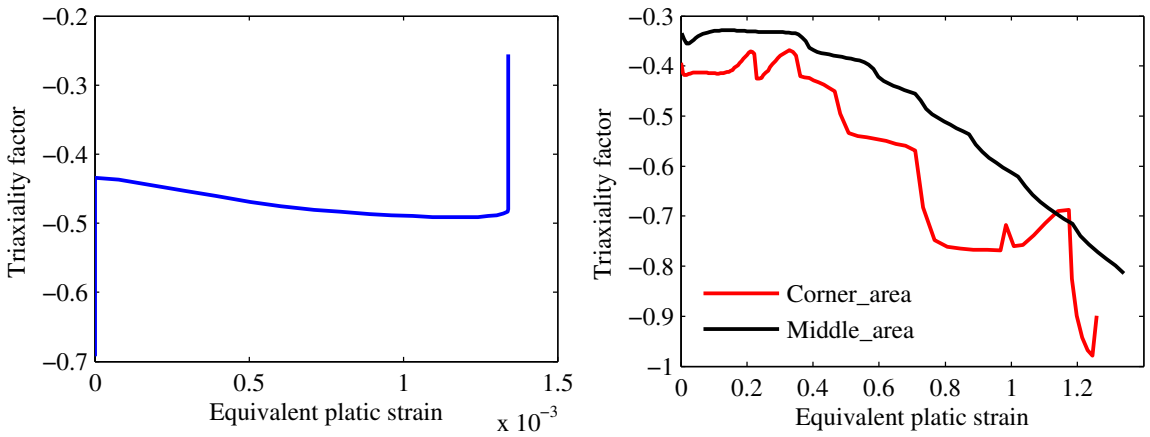

(a) Dead zone

(b) Corner and middle of the sample

FIGURE 2.10: Variation of triaxiality and equivalent plastic strain in compression

EQPLAS of 1.34 at $\Delta L/L_0 = 0.5$.
As can be seen in the Fig. 2.10b, for the selected point in the corner area of the sample, state of stress produces complex negative triaxiality that starts with -0.4 and varies to less than -0.9 at high compression levels. However, some local increase in the T.F. is calculated. The amount of plastic deformation for this point is greater than 1.26 at the end of compression. Based on the above discussion, for the selected points in the middle and corner of the compression sample, the immense equivalent plastic strain in presence of a complex state of stress creates an ideal condition for investigating the mechanical behavior of micro-model under large deformations and complex loads.

Chapter 3

Micromechanical study: RVE

3.1 Representative volume element

Ductile iron is known as a metal matrix composite which contains inclusions (spherical graphite nodules) that are held together in a ferrous matrix (Grimvall, 1997). A schematic of micro structure of DCI is shown in Fig. 3.1a (Zhang et al., 2019). Random distribution of the graphite nodules with different shapes and sizes throughout the DCI can be seen in the figure.

Representative volume element (RVE) is defined as the minimum volume that its behavior is representative of the material (Hill, 1963). In the micro-mechanical approach constitutive behavior of a composite in macro-scale can be studied by considering its well defined RVE. One direct method to make a RVE, is exactly considering one part of macro volume. Following this method, RVE should contain noticeable number of nodules with real shapes, sizes and distances. This consideration obviously increase the RVE dimensions and solution time (Pereira et al., 2018).

In the present work, it is assumed that ductile cast iron is made by spatial arrangement of a cubic RVE that has only one spherical graphite nodule at the center as is depicted in Fig. 3.1b where L_0 denotes the repeating RVE length. This assumption in one hand simplifies the problem and reduces the numerical costs and on the other hand can lead to acceptable macro-scale results (Drago and Pindera, 2007; Sun and Vaidya, 1996).

In this case the sphere diameter is average diameter of graphite nodules distributed throughout the DCI. In a composite, if V_n and V_{RVE} be the volume of inclusions and volume of the RVE respectively, volume fraction is defined as: $\mathrm{VF} = V_n / V_{RVE}$. Once graphite volume fraction of a DCI is given, the periodic length of the RVE can be simply calculated.

Discretized RVE model will be used to investigate the micro-mechanical behavior of the DCI under different loading conditions. Finite element code, MCS.MARC, is used for modeling the micro model; RVE is meshed with eight-node eight-integration point isoparametric hexahedral elements. It should be emphasized that to overcome possible numerical errors due to using different element class, the same element type is regarded in both micro-scale and macro-scale study.

In this thesis, the DCI response under different loading conditions such as uniaxial tension, uniaxial compression, simple shear and cylinder compression conditions will be studied. Numerical investigations show that in some cases such as uniaxial loading, which separation between nodule and matrix is a part of RVE behavior, initial unrealistic penetration of nodes into curvature interface cause numerical problems during separation; the penetrated nodes stick to the other surface and remain inside during separation. To overcome

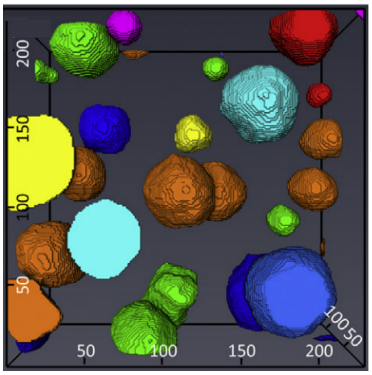

(a) Distribution of nodules in DCI (Zhang et al., 2019)

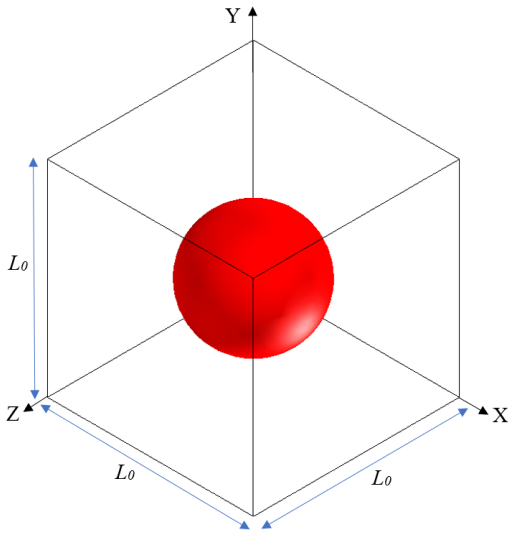

(b) Assumed repeating RVE

FIGURE 3.1: Micro structure of DCI

this problem, one practical solution is to set correspondingly nodes of nodule to the nodes of matrix on the interface. Fig. 3.2 shows the geometry and mesh of the designed RVE when separation may occur where corresponding nodes in the interface can be seen better in the one-eight of the model. This mesh pattern is adopted by using 13312 and 2048 elements for matrix and nodule respectively and the micro model is called *Corsp_RVE*.
Also, experimental observations show that separation between nodule and matrix dose not occur under compression of the cylinder. But, nodule deformation and RVE distortion are huge and using Corsp_RVE model prevents to reach extreme configurations. So, finer mesh is selected here for nodule and matrix to reduce extreme distortion of the elements as much as possible. It should be emphasized that although increasing number of elements provides better mesh shape at large deformations but due to complexity of the problem some numerical errors arises that lead to precocious non-convergence of the solution. Therefore, 25168 and 13608 elements are considers to mesh the matrix and nodule respectively. Elements of matrix are designed to have more height along compression direction (z axis) to avoid excessive squeezed length in high compression levels. Designed RVE for micro-scale study of DCI under compression is called *Comp_RVE* and depicted in Fig. 3.3 where one eight of the model has been magnified For better presentation.

3.2 Periodic Condition

As stated in the previous section, it is assumed that RVE is representative of the microstructure and has regular pattern. Therefore, periodic boundary concoctions (PBCs) can be considered to take properly deformation field around it into account (Hill, 1963). Many researchers such as Hori and Nemat-Nasser concluded that considering periodic boundary condition leads to better results for investigating RVE of the composites respect to simple

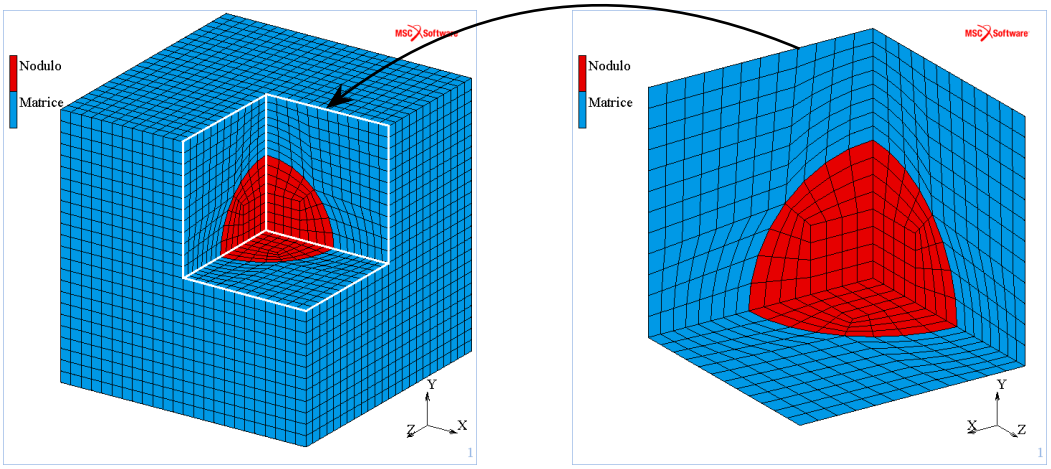

FIGURE 3.2: Geometry and mesh of designed RVE for tension (Corsp_RVE)

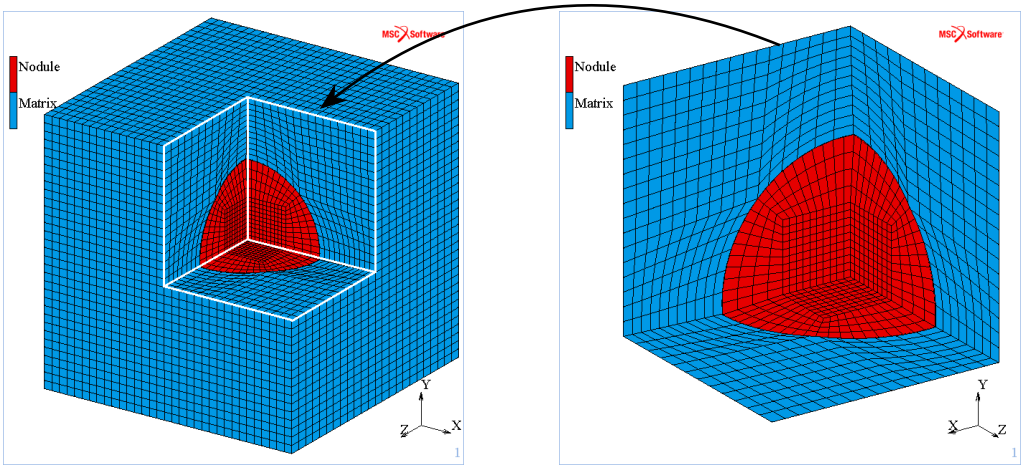

FIGURE 3.3: Geometry and mesh of designed RVE for compression (Comp_RVE)

boundary condition (Hori and Nemat-Nasser, 1999). Periodic boundary condition guarantees the periodicity of the outer surface of the RVE in which all the representative volume elements deform similarly and no separation or penetration occurs.

In the present study, periodic boundary condition with homogeneous displacement is adopted. Due to this assumption the displacement of the RVE boundary $\mathbf{U}^b$ is defined by:

$$\mathbf{U}^b = \mathbf{U} + \mathbf{U}^* \tag{3.1}$$

where $\mathbf{U}$ is the local displacement field and $\mathbf{U}^*$ denotes periodic displacement field on the RVE surfaces. Usually, revealing RVE boundary displacement from Eq. 3.1 can not be performed directly because of the unrecognized periodic displacement $\mathbf{U}^*$. RVE boundaries are consisted of six surfaces that two by two are parallel and each parallel pair is assumed to be normal to one principal axis. Regarding to the Eq. 3.1 displacement field of each pair of parallel surfaces is:

$$\mathbf{U}^{b1} = \mathbf{U}^1 + \mathbf{U}^* \tag{3.2a}$$

$$\mathbf{U}^{b2} = \mathbf{U}^2 + \mathbf{U}^* \tag{3.2b}$$

where superscripts 1 and 2 denote two opposite parallel boundary surfaces of the RVE. Periodic boundary condition ensures that for the opposite planes 1 and 2 the periodic displacement, $\mathbf{U}^*$, is equal due to periodicity. Hence, relative displacement between opposite planes is obtained by subtracting Eq. 3.2a from Eq. 3.2b:

$$\mathbf{U}^{b2} - \mathbf{U}^{b1} = \mathbf{U}^2 - \mathbf{U}^1 = \mathbf{\Delta U} \tag{3.3}$$

Employment of Eq. 3.3 will ensure that displacement field of RVE boundaries are continuous.Continuity of the RVE surface tractions gives:

$$\mathbf{T}^{b1} + \mathbf{T}^{b2} = 0 \quad which \quad \mathbf{T} = \boldsymbol{\sigma}^m \mathbf{n} \tag{3.4}$$

because normal vectors to the opposite parallel boundaries fulfill: $\mathbf{n} = -\mathbf{n}$.

In genera case, $\mathbf{\Delta U}$ in Eq. 3.3 can be expressed by considering displacement gradient ($\boldsymbol{\nabla}\mathbf{U}$) (Li and Sitnikova, 2019) :

$$\mathbf{\Delta U} = \begin{Bmatrix} \Delta U_x \\ \Delta U_y \\ \Delta U_z \end{Bmatrix} = \begin{Bmatrix} U_x \\ U_y \\ U_z \end{Bmatrix}_{(x^2,y^2,z^2)} - \begin{Bmatrix} U_x \\ U_y \\ U_z \end{Bmatrix}_{(x^1,y^1,z^1)} = \boldsymbol{\nabla}\mathbf{U}\mathbf{\Delta x} \tag{3.5}$$

where U_x, U_y and U_z are displacement along x, y and z axes for a boundary. Due to presuming simple cubic packing for the RVE, transnational vector $\mathbf{\Delta x}$ from one RVE to another is introduced by:

$$\mathbf{\Delta x} = \begin{Bmatrix} \Delta x \\ \Delta y \\ \Delta z \end{Bmatrix} = \begin{Bmatrix} L_0 i \\ L_0 j \\ L_0 k \end{Bmatrix} \tag{3.6}$$

For a multi-scale study and base on the Eq. 3.5, for investigating material behavior in micro-scale, relative displacement between boundaries can be obtained base on the local displacement gradient in macro-scale. In general case, when a particle of the macro structure experiences general state of deformation involving combination of distortion and volumetric strains, calculating gradient of displacement is burdensome.
In small strain problems, displacement gradient can be simplified by considering only its symmetric part which is the strain tensor. Therefore, $\mathbf{\Delta U}$ is simply calculated by replacing displacement gradient with local macro strain field in the Eq. 3.5 as it has been adopted by some researchers (Pierre M. Suquet, 1987; Andriollo, Thorborg, and Hattel, 2016; Tian et al., 2019).
In the finite deformation problems, gradient of displacement in Eq. 3.5 is directly obtained from local gradient of deformation in macro-scale by:

$$\mathbf{\nabla U} = \boldsymbol{F} - \boldsymbol{I} \tag{3.7}$$

where $\boldsymbol{F}$ denotes deformation gradient and $\boldsymbol{I}$ is unit tensor.
In the present work displacement gradient is obtained from Eq. 3.7 which is definitely valid not only for small strains but also for large deformations; where relation between strain field and displacement is not more linear.

Periodic boundary condition constrains in Eq. 3.3 are usually performed with defining linear linkage between nodes on the RVE surfaces in the finite element software. For example MSC.MARC uses *Servo Link* to input linear constraint (tying) with the following form (MSC MARC Vol. A, 2019):

$$\mathbf{U_t} = a_1\mathbf{U_{r1}} + a_2\mathbf{U_{r2}} + ... \tag{3.8}$$

where $\mathbf{U_t}$ is the displacement of a node on the surface of the RVE to be constrained (tied), $\mathbf{U_{r1}}$ is retained displacement of specified nodes and a is a constant that describe relative displacement between selected nodes. In deed, Eq. 3.8 consists of three independent relations for three degree of freedom each along one coordinate axis.
Generally, homogeneous periodic boundary condition implemented into the RVE by defining *Reference Point* (RP). Reference points are needed to satisfy the relative displacement between boundaries in Eq. 3.3 through servo links. For a general three dimensional RVE, every relative displacement of the pair parallel boundaries is defined by a reference point and so three reference points are introduced. Therefore, relative displacement between opposite boundaries is represented by displacement of the reference points:

$$\mathbf{U}^{b2} - \mathbf{U}^{b1} = \mathbf{U}^{RP} \tag{3.9}$$

comparing Eq. 3.3 and Eq. 3.9 leads to:

$$\mathbf{U}^{RP} = \mathbf{\Delta U} \tag{3.10}$$

Base on Eq. 3.10 for studying the deformation of the RVE with PBC the local displacement field $\mathbf{\Delta U}$ is applied to the reference points as nodal constrains.

In finite element analysis, defining manually servo links between nodes is cumbersome especially when RVE surfaces contain large number of nodes. Hence, Digimat package is used to define the servo links between parallel surface boundaries to model the periodic

condition. An example of the servo links created by Digimat for simulating periodic boundary condition of the RVE is shown in Fig. 3.4a where RP.X, RP.Y and RP.Z are reference points for introducing relative displacements field between parallel boundary surfaces normal to x, y and z directions respectively.

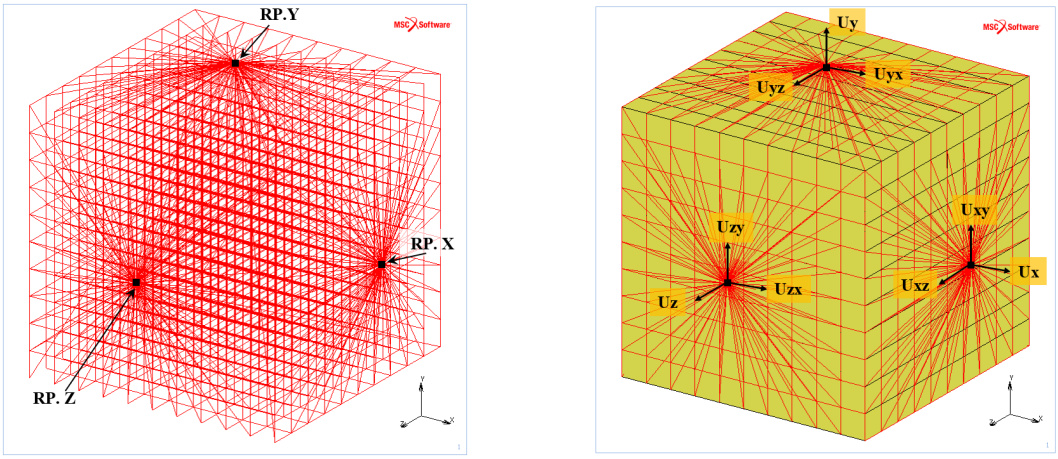

(a) Designed servo links for the RVE

(b) Servo links added to the RVE mesh

FIGURE 3.4: An example of the RVE with servo links

By merging previously created mesh and servo links into MSC. MARC modeling phase of the RVE is completed. A state-of-the-art technique is adopted to couple the servo links with the imported mesh. It has worth to say that number and location of the surface nodes for introducing PBC have to be identical with surface nodes of the mesh to guarantee the correct periodic condition. An example of the RVE with servo links and periodic boundary condition is represented in Fig. 3.4b.
As it was described, in periodic boundary problems with homogeneous displacement condition the desired deformation of the RVE can be achieved by inserting appropriate relative displacement to the reference points. In general case each control node have 3 possible displacements. For instance, RP.X may have displacement U_x, U_y and U_z respectively in x, y and z directions and the same condition for RP.Y and RP. Z exists as it is plotted in the Fig. 3.4b. These nine possible displacements are imposed to the reference points to inspect micro-model behavior under different deformation loading conditions.

in the following, for instance, boundary conditions of the RVE in some simple cases like uniaxial loading and simple shear are presented. Obviously for complicated cases, the above mentioned method for calculating displacement field of the reference points from deformation gradient, can be used.

3.2.1 Uniaxial loading

For studying uniaxial deformation of the RVE with PBC along x axis, a fix origin with the following conditions may be adopted:

$$U_x = \Delta L_u \tag{3.11a}$$
$$U_{xy} = U_{yz} = U_{zx} = 0 \tag{3.11b}$$

where ΔL_u in Eq. 3.11a is the displacement of the RVE along x and is inserted to the RP. X. which obviously implies uniaxial tension if this displacement is positive. Conditions in Eq. 3.11b are used for avoiding unfavorable rotation of the RVE during deformation without compromising its periodic boundary condition.

3.2.2 Simple shear

In simple shear case, if for example shear occurs in xy plane, the pure shear condition in the RVE can be achieved by using the following conditions:

$$U_{xy} = U_{yx} = \Delta L_s/2 \tag{3.12a}$$

$$U_{yz} = U_{zx} = 0 \tag{3.12b}$$

where in Eq. 3.12a ΔL_s denotes total shear displacement that is needed for specific shear deformation. For RVE with PBC, half of this displacement is applied to the RP.X and RP.Y to provide relative shear displacement along y and x axis respectively. Again, Eq. 3.12b is implied to avoid numerical difficulties due to the free rotation of the RVE.

3.3 Stress and strain measure

In this thesis, simulations are performed by MSC. MARC using Updated Lagrangian formulation to ensure the functionality of the code in large deformations. Therefore, logarithmic strain and Cauchy stress measure is acquired (MSC MARC Vol. A, 2019). If deformation gradient in one increment is known, logarithmic strain, $\boldsymbol{\varepsilon}$, and Cauchy stress, $\boldsymbol{\sigma}$, tensors can be calculated by (De Souza Neto, Perić, and Owen, 2008):

$$\boldsymbol{\varepsilon} = \ln \sqrt{\boldsymbol{F}\boldsymbol{F}^T} \tag{3.13}$$

$$\boldsymbol{\sigma} = J^{-1}\mathbf{P}\boldsymbol{F}^T \tag{3.14}$$

where $\mathbf{P}$ denotes first Piola-Kirchhoff tensor and J is the Jacobian of $\boldsymbol{F}$ and is obtained by: $J = \det \boldsymbol{F}$.

Due to different geometry and properties of the nodule and matrix, when RVE undergoes a thermo-mechanical loading the distribution of the local quantities like stress or strain tensor are not uniform. In the following, two methods to obtain overall strain and stress field of the RVE are described. By the way, calculation of the RVE stress and strain components at each increment is a part of FE post-processing phase and executed by using a python script.

3.3.1 Using reference points results

By inserting $\boldsymbol{\Delta U}$ as boundary conditions to the RVE, gradient of displacement and reaction forces (R_{ij}) at each reference point are available after finite element analysis.

For obtaining overall strain field of the RVE, $\bar{\boldsymbol{\varepsilon}}$, first $\boldsymbol{\nabla U}$ is calculated from Eq. 3.5 regarding to the displacements of reference points. Then, deformation gradient of the RVE is obtained from Eq. 3.7 and finally $\bar{\boldsymbol{\varepsilon}}$ is calculate from Eq. 3.13.

Once reaction forces in reference points are obtained, overall first Piola-Kirchhoff stresses ($\bar{P}_{ij}$) of the RVE are defined by dividing them to the original area of the RVE:

$$\bar{P}_{ij} = \frac{R_{ij}}{L_0 L_0} \tag{3.15}$$

Then, by inserting this overall first Piola-Kirchhoff tensor ($\bar{\mathbf{P}}$) and formerly calculated deformation gradient into Eq. 3.14, overall Cauchy stress tensor ($\bar{\sigma}$) of the RVE is calculated.

3.3.2 Finite element homogenization

Generally, for any micro-field parameter of the RVE the homogenized quantity can be obtained by:

$$\bar{\mathbf{q}} = \frac{1}{V_c} \int_{V_c} \bar{\mathbf{q}} \, dV \tag{3.16}$$

where $\bar{\mathbf{q}}$ is the micro-field quantity and V_c denotes the gage volume of the contents and can be volume of the entire RVE, matrix or inclusions. In this technique, stress and strain components of the homogeneous microscopic medium are obtained by calculating homogenized stress and strain tensors through the RVE volume with respectively substituting $\bar{\sigma}$ and $\bar{\varepsilon}$ in Eq. 3.16:

$$\bar{\sigma}_{ij} = \frac{1}{V_{RVE}} \int_{V_{RVE}} \sigma_{ij}(\mathbf{X}) \, dV \tag{3.17}$$

$$\bar{\varepsilon}_{ij} = \frac{1}{V_{RVE}} \int_{V_{RVE}} \varepsilon_{ij}(\mathbf{X}) \, dV \tag{3.18}$$

Eqs. 3.17 and 3.18 illustrate that for a RVE with total volume V_{RVE} the homogenized stress component $\bar{\sigma}_{ij}$ and homogenized strain component $\bar{\varepsilon}_{ij}$ are calculated respectively by integration of local stress $\sigma_{ij}(\mathbf{X})$ and local strain $\varepsilon_{ij}(\mathbf{X})$ over the RVE volume where $(\mathbf{X})$ demonstrates the location of the local quantities in the RVE ($\mathbf{X} \in V_{RVE}$).
In finite element method, integration in the Eq. 3.17 and Eq. 3.18 can be rewritten as:

$$\bar{\sigma}_{ij} = \frac{1}{V_{RVE}} \sum_{n=1}^{nel} \sum_{g=1}^{nip} \sigma_{ij} V_g \tag{3.19}$$

$$\bar{\varepsilon}_{ij} = \frac{1}{V_{RVE}} \sum_{n=1}^{nel} \sum_{g=1}^{nip} \varepsilon_{ij} V_g \tag{3.20}$$

where nel denotes the total number of RVE elements and for the n^{th} element: nip is the number of integration points, σ_{ij}, ε_{ij} and V_g represent the stress, strain and current volume at the g^{th} integration point respectively.

A comparative study on the overall Cauchy stress and overall logarithmic strain obtained by different methods of sections 3.3.1 and 3.3.2 shows that the results are almost the same with the difference of defined tolerance for the finite element solution convergence. In this work RVE stress and strain components are defined by finite element homogenization

method. RVE hydrostatic stress ($\bar{\sigma}_h$) and effective deviatoric stress ($\bar{\sigma}_{eds}$) are defined as:

$$\bar{\sigma}_h = \frac{1}{3} tr(\bar{\boldsymbol{\sigma}}) \tag{3.21}$$

$$\bar{\sigma}_{eds} = \sqrt{3J_2(\bar{\mathbf{S}})} = \sqrt{\frac{3}{2}\,\bar{\mathbf{S}} : \bar{\mathbf{S}}}, \quad \bar{\mathbf{S}} = \bar{\boldsymbol{\sigma}} - \bar{\sigma}_h \mathbf{I} \tag{3.22}$$

3.3.3 Multi scale study

For multi scale study applications, such as inverse calibration of RVE, it is tried to obtain similar mechanical responses in both macro and micro scales. Although the mechanical properties of the RVE are not dependent on the geometry or boundary conditions and they are inherent material properties, strain energy equilibrium should be satisfied on the boundaries (Hill, 1963):

$$\overline{\boldsymbol{\sigma}:\boldsymbol{\varepsilon}} = \bar{\boldsymbol{\sigma}}:\bar{\boldsymbol{\varepsilon}} \tag{3.23}$$

Based on the Hill's energy law, the total strain energy of the RVE is equal to the effective strain energy for the homogeneous macroscopic medium (Hill, 1963). As it was discussed in the section 3.2, calculating displacement of the reference points in micro scale base on the local gradient of displacement in macro scale will guarantee to have same deformation gradient in both scales. Subsequently, the overall strain field of the RVE is identical to that of macro scales. Necessarily, same stress field in both scales are needed to satisfy the Hill's energy law. This condition is used to find unknown mechanical properties of RVE.

It has worth to note that in a multi scale numerical study, number of increments that is needed to reach a specified level of deformation ought to be equal in both macro and micro scales. In this case, at each increment, same strain is imposed in both scales and deformation history dose not affects the consequent stress field.

Chapter 4

Micromechanical study: local residual stresses

4.1 Introduction

It was discussed in section 1.2.3 that during the solidification of the DCI, residual stresses are formed due to the discord within thermal expansion coefficient of matrix and nodules. Zhang et al. (Zhang et al., 2016) experimentally measured the elastic residual stresses of a metal mold DCI. In this chapter, the micromechanical model proposed in the chapter 3 is adopted to predict the residual stresses and mechanical behavior of this DCI. The physical-mechanical properties of the constituents at different temperatures are evaluated by integrating the data available in the literature in conjunction with the results of JMatPro code.

4.2 Materials and constitutive modeling

4.2.1 DCI

The material is the metal mold DCI analyzed in Zhang et al. (Zhang et al., 2016) whose chemical composition is reported in the Table 4.1. The matrix of this DCI is ferritic with 5% volume fraction of pearlite and average grain size of ∼30 µm; the volume fraction and mean size diameter of graphite nodules are 11.5% and ∼30 µm respectively.

TABLE 4.1: Chemical composition of the DCI (in wt.%), Fe: balance.

C	Si	Mn	P	S	Cr	Ni	Co	Cu	Ti	V	Mg	Ce	Se
3.68	2.30	0.22	0.015	0.011	0.027	0.048	0.024	0.016	0.017	0.014	0.11	0.042	0.043

Solid fractions variation of DCI during cooling, which is calculated by JMatPro Base on its composition, is shown in Fig. 4.1. Acceptable graphite volume fraction, 11.2%, is obtained at room temperature and the presence of cementite confirms the pearlite-ferrite structure of the matrix with 7.7% of pearlite volume fraction. At 790°C the accumulation of carbon in nodules ends and lower than this temperature the mass fraction of graphite is the same as room temperature.

4.2.2 Matrix

Chemical composition of the matrix, reported in Table 5.1, can be calculated base on the carbon remaining at room temperature in the DCI and scaling the amplitude of all elements

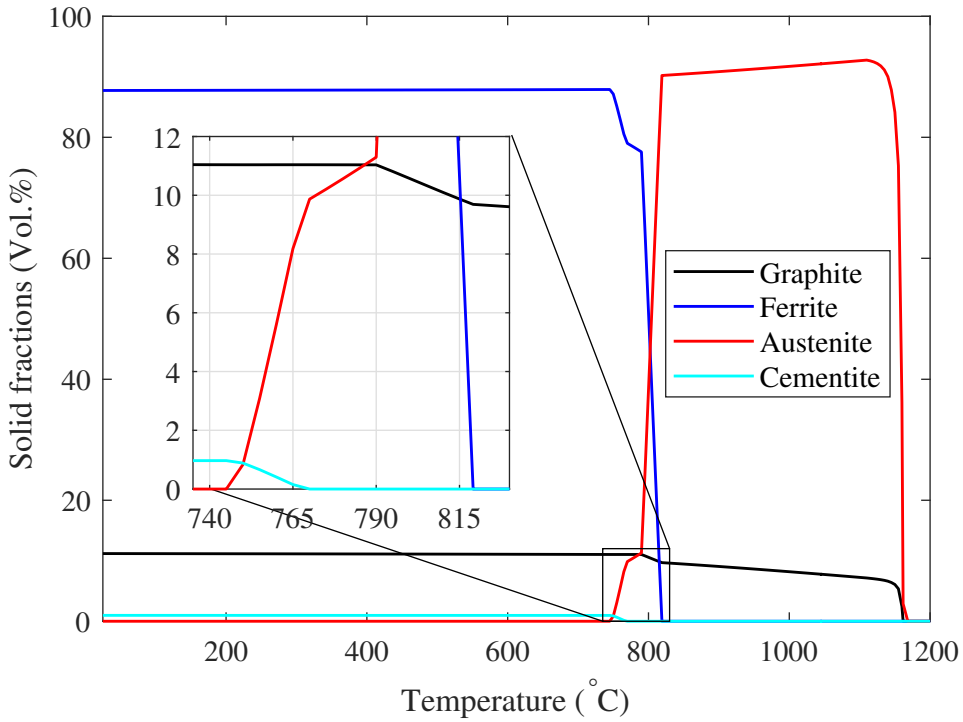

FIGURE 4.1: Variation of DCI solid fractions in Vol.% with temperature

referring only to the matrix. It should be noted here that JMatPro calculations show that a slight decrease in amount of carbon leads to more satisfactory portion of pearlite in the alloy. The variation of matrix solid fractions with temperature is shown in Fig. 4.2.

TABLE 4.2: Chemical composition of matrix (in wt.%), Fe: balance.

C	Si	Mn	P	S	Cr	Ni	Co	Cu	Ti	V	Mg	Ce	Se
0.0581	2.386	0.228	0.0156	0.0114	0.028	0.0498	0.0249	0.0166	0.0176	0.0145	0.1142	0.0436	0.0446

The amount of cementite available at room temperature, provides 5.7% of pearlite volume fraction in the matrix which can be assumed a satisfactory value regarding to the under study DCI. As the figure suggests, at 769°C the remaining amount of austenite decomposes to ferrite and cementite under a eutectoid reaction. Therefore, the mentioned temperature can be regarded as lower eutectoid temperature, T_L, of the cooling process. Due to the difference in microstructure of austenite (FCC) and ferrite (BCC), a sudden volume expansion takes place at this temperature, resulting in discontinuity in physical and mechanical properties of the material. This challenge, along with the fact that accounting for the phase transformation in the micro-model will complicate the numerical analysis, makes it reasonable to assume that the cooling simulation can be run from 769°C. Although this temperature is lower than 790°C, where nodule growth ends as discussed in the previous section, the low strength of the matrix indicates that the error in residual stress calculations will not be significant. This simplification can also be found in the literature; for instance Andriollo et al. to numerically measure the residual stresses around a nodule of the same DCI, it was assumed that cooling process starts from T_L (Andriollo et al., 2019).

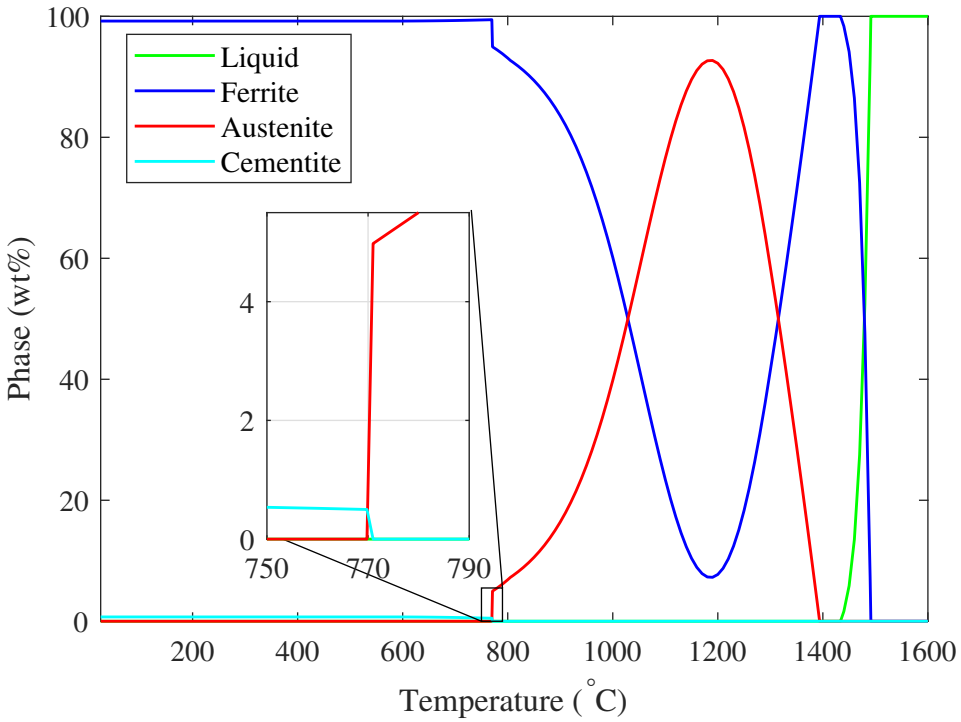

FIGURE 4.2: Variation of matrix phases in wt% with temperature

The variation of matrix proof stress with temperature for the given grain size is calculated by JMatPro and shown in Fig. 4.3 where the break in the curve at 769°C is noted by red dashed line. From these values the true tress-strain curves at different temperatures can be acquired.

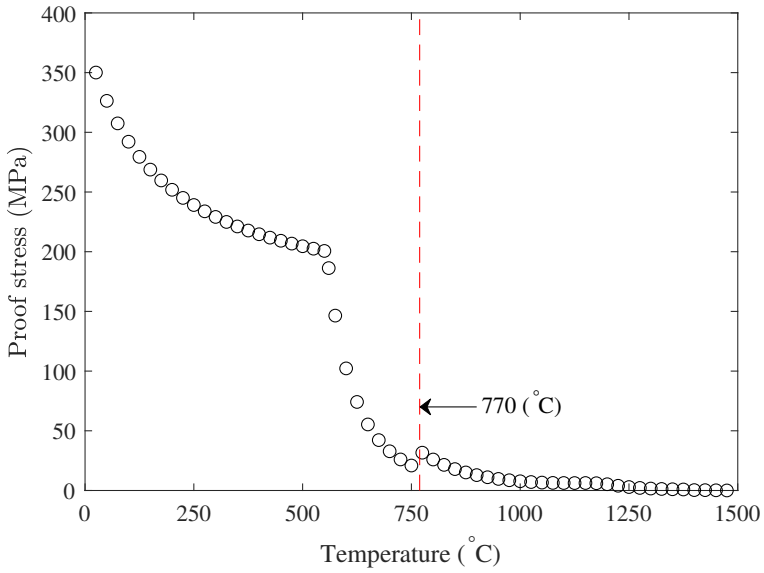

FIGURE 4.3: Variation of matrix proof stress with temperature

Fig. 4.4 plots matrix flow curves for some temperatures. At room temperature, good

agreement between JMatPro data and experimental tensile curve, for the matrix of the same grade of DCI (Kuna and Sun, 1996), can be seen for true strains lower than 0.2. Evolution of some elastic and physical properties of the matrix with temperature is shown in Fig. 4.5 and Fig. 4.6 respectively.

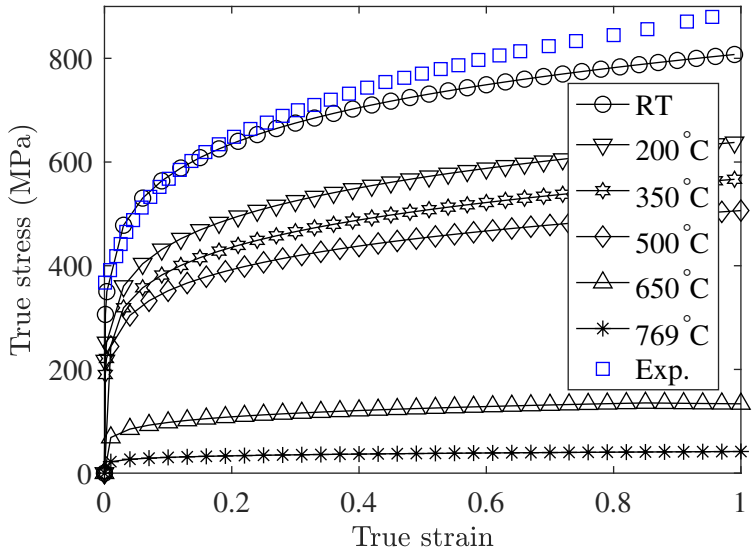

FIGURE 4.4: Stress-strain curve of the matrix at different temperatures

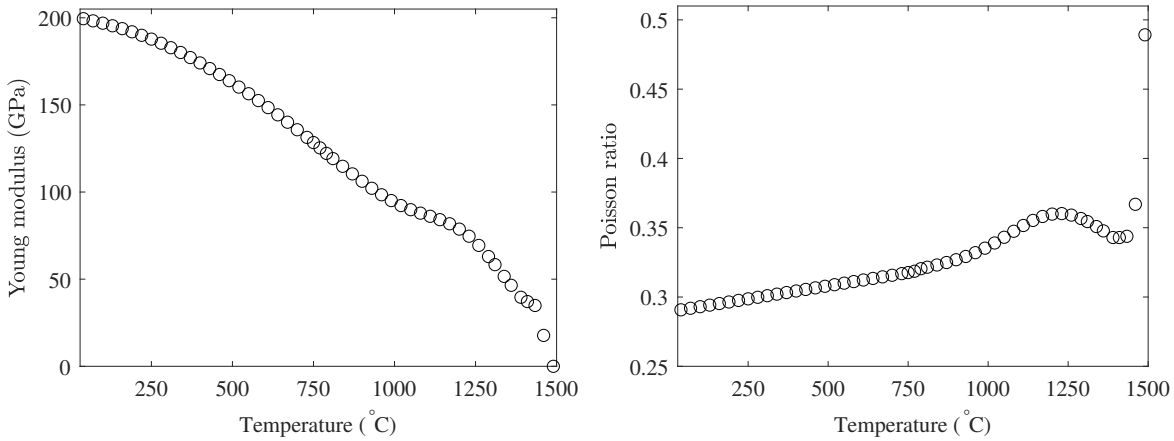

(a) Young's modulus (b) Poisson's ratio

FIGURE 4.5: Variation of some matrix elastic properties with temperature

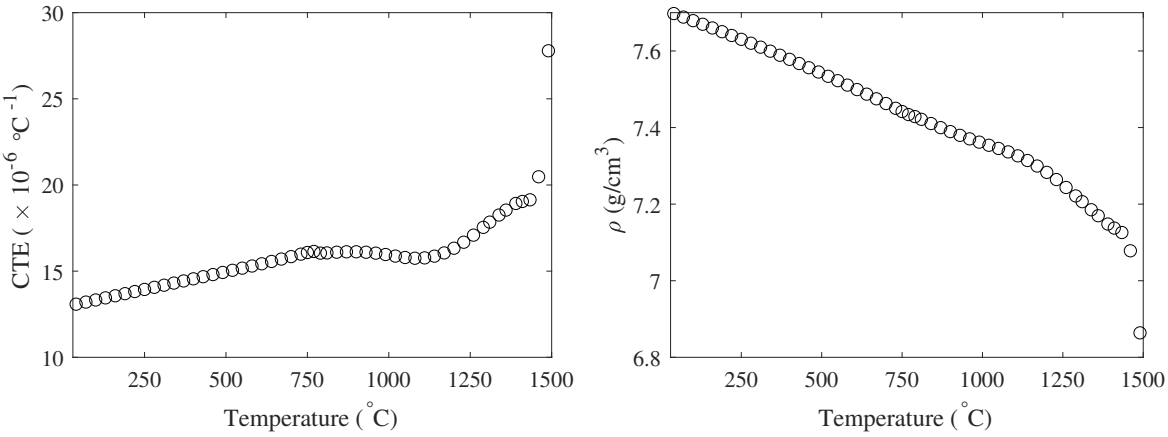

(a) CTE (b) Density

FIGURE 4.6: Variation of some matrix physical properties with tempratute

Experimental studies on the creep behavior of ferritic steel alloys with similar percentage of silicon and nickel in the matrix are available in the literature. For instance, the steady-state creep of Fe-Si steels has been investigated at different temperatures and at different percentages of silicon in the alloy composition: below 600°C (Davies, 1963), at 643°C (Barrett and Nix, 1965) and above 1100°C (Stang, Nix, and Barrett, 1973). Andriollo et al. performed some uniaxial tensile tests on equivalent matrix material to study its time-dependent behavior (Andriollo et al., 2018), but the experimental data are not sufficient to fully characterize the matrix creep behavior.

Literature review reveals that admirable experimental investigations of the creep behavior of a ferritic steel similar to under study matrix have been executed by Kaibyshev and Kazakulov (Kaibyshev and Kazakulov, 2004). They studied the deformation behavior of Fe-3Si steel in the temperature range of 400-900°C with load and displacement control tests. Table 4.3 shows the chemical composition of the Fe-3Si alloy where a satisfactory similarity with the matrix elements can be assumed. They reported that the average grain size is ∼6 mm while that of the matrix is much smaller. This can be interfere as an obstacle in adopting creep data of this alloy for predicting creep deformation of the matrix, if the creep behavior of ferritic steel depends on the grain diameter.

TABLE 4.3: Chemical composition of the Fe-3Si (in wt.%), Fe: balance. (Kaibyshev and Kazakulov, 2004)

Si	C	S	Mn	Cr	Ni	Cu	P	Al	As
3.1	0.025	0.025	0.06	0.03	0.06	0.06	0.01	0.003	0.008

Experimental studies on the effect of grain size on creep deformation of Fe-3Si steel alloy reveal that for this type of material, grain size does not affect steady state creep, even though some effects on transient creep cannot be neglected (Barrett, 1964; Stang, Nix, and Barrett, 1973; Stang, Nix, and Barrett, 1975). Therefore, using the creep data of Fe-3Si ferritic steel alloy with a larger grain size for characterizing creep behavior of matrix with smaller grain size, can be supposed to be practical for predicting steady-state creep, but may introduce an

error in the primary creep calculation. Due to the fact that major part of the creep deformation is formed in the steady state stage, this error is neglected for simplification. Therefore, it is assumed that the creep behavior of the matrix follows that of the Fe-3Si ferritic steel alloy.

The following semi-empirical equation has been proposed for the secondary creep rate (Mukherjee, Bird, and Dorn, 1968; Bird, Mukherjee, and Dorn, 1969):

$$\dot{\varepsilon}_{ss} = A\frac{DGb}{kT}\left(\frac{\sigma}{G}\right)^n \tag{4.1}$$

where A is dimensionless constant, D is the self diffusivity, G is the shear modulus, b is the Burgers vector, K is the Boltzmann constant, T is the absolute temperature, σ is the applied stress and n is the stress exponent.

Later, understanding of the creep behavior was improved by introducing the conception of effective stress, $\sigma - \sigma_p$, so that steady-state creep rate is a function of the effective stress: $\dot{\varepsilon}_{ss} \propto \left(\sigma - \sigma_p\right)^n$ (Lagneborg and Bergman, 1976; Evans and Harrison, 1976). σ_p is called *back stress* or *friction stress* and may be due to the dependence of creep on subgrain size, subcells or particle dispersion presence in pure or alloy metals (Davies et al., 1973; Parker and Wilshire, 1975). This hypothesis assumes that creep occurs only when effective stress is positive and that for the applied stress levels below σ_p creep is negligible (Lund and Nix, 1976).

Therefore, considering that the secondary creep deformation in Eq. 4.1 is driven by effective stress, the following rate-controlling relationship can be proposed:

$$\dot{\varepsilon}_{ss} = A\frac{DGb}{kT}\left(\frac{\sigma - \sigma_p}{G}\right)^n \tag{4.2}$$

In the following, the creep model proposed in Eq. 4.2 is calibrated on the basis of experimental creep measurements of Fe-3Si (Kaibyshev and Kazakulov, 2004). It should be described that in the present work, the RVE cooling begins from the temperature below 800°C and deformation behavior of the matrix at higher temperatures is of no interest. Also, experimental data reveal that at temperatures below 550°C the required stresses for inelastic deformation due to creep is exaggeratedly higher than those created within the RVE. Therefore, the study of the creep behavior of the alloy is limited to the above range.

Attempts for calibrating the creep model, with the definition of back stresses. Fig. 4.7 indicates that for the presumed temperature range, at the low stress regime (left side of the red dashed line), the relationship between $\dot{\varepsilon}_{ss}^{(1/n)}$ and applied stress is linear with $n = 4.75$. Then, for a given temperature, the back stresses are calculated by extrapolating the linear fit to zero strain rate.

Mohamed et al. proposed that back stresses are function of temperature with this empirical relationship (Mohamed, Park, and Lavernia, 1992) :

$$\frac{\sigma_p}{G} = B\exp\frac{Q_p}{RT} \tag{4.3}$$

where B is a dimensionless constant, R is the universal gas constant and Q_p is energy term. With respect to this equation, the data vary linearly if $\ln\left(\sigma_p/G\right)$ is plotted as a function of $1/T$. Fig. 4.8 confirms this linear variation, so Eq. 4.3 can be calibrated to predict the back stresses in the considered temperature range. Consequently, the constants Q_p and B are obtained by linear fitting and reported in Table 4.4.

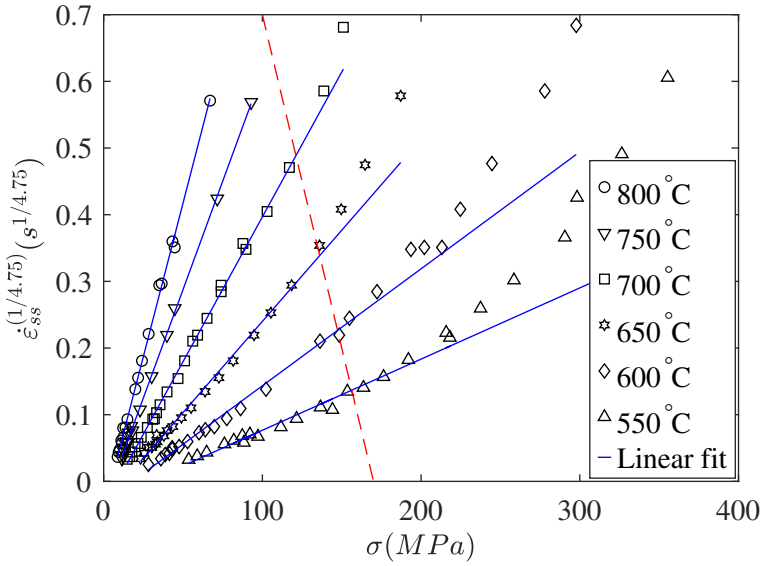

FIGURE 4.7: Relationship between $\dot{\varepsilon}_{ss}^{\frac{1}{n}}$ and σ for n=4.75

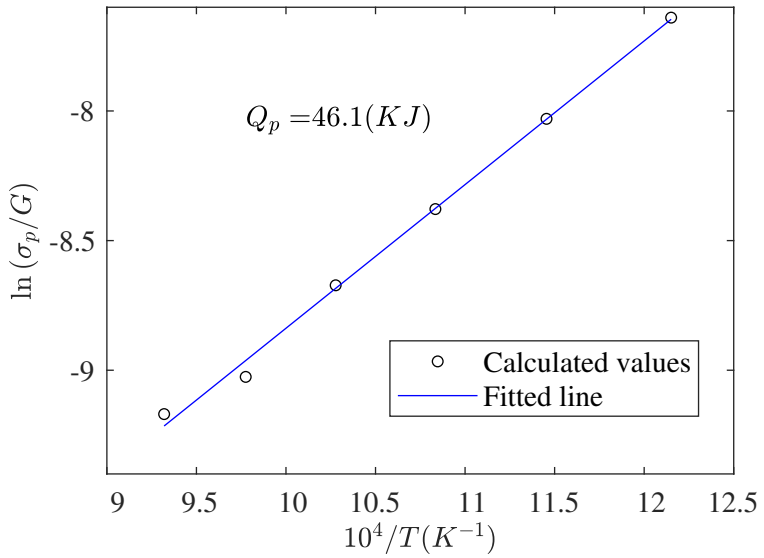

FIGURE 4.8: Variation of normalized back stress with temperature

After defining back stresses, the next step is to introduce the self diffusivity parameter, D. In solids, this parameter is usually given by an Arrhenius equation (Madelung, 1990):

$$D = D_0 \exp \frac{-Q}{RT} \tag{4.4}$$

where D_0 is the material constant and Q is the activation energy for inelastic deformation. If D of Eq. 4.4 is inserted into Eq. 4.2 then the slope of $\ln[(\sigma - \sigma_p)/G] - (1/n)\ln(T/G)$ against $1/T$ is $Q/(nR)$. Fig. 4.9 is plotted with assuming n=4.75 where at each strain rate activation energy can be calculated by the derivative of the fitted quadratic polynomial.

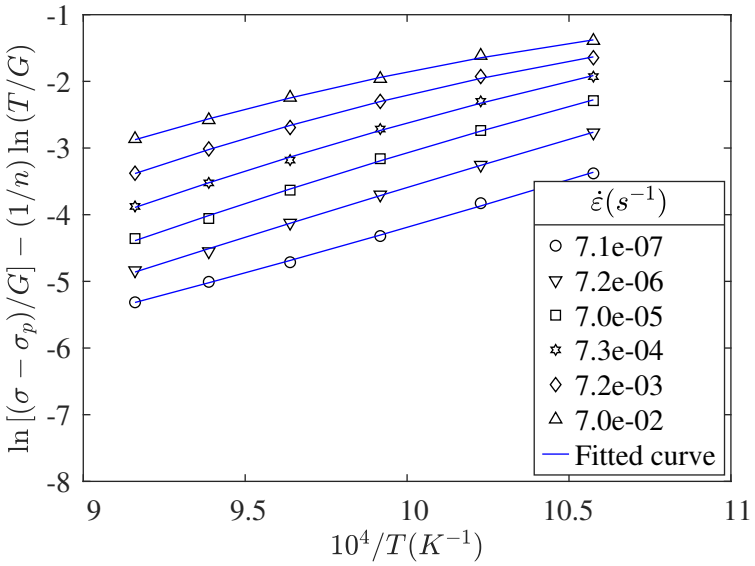

FIGURE 4.9: Typical plot for determining activation energy

Fig. 4.10 shows the range and average of the obtained values for the Q. Despite a wide range at some temperatures, activation energy increases to reach its maximum of 280 (KJ/mol) at 800°C. This value is in agreement with the activation energy for self-diffusion in α iron: 280 (KJ/mol)(Cottrell, 1995) or 281.5 (KJ/mol) (Madelung, 1990). Therefore, it can be concluded that the proposed back stress model gives a realistic activation energy for the power law creep model. Assuming the constant $D_0 = 2 \times 10^{-4}$, adopted from self-diffusion relation for α-iron (Evans and Harrison, 1976), D in the creep model is fully defined.

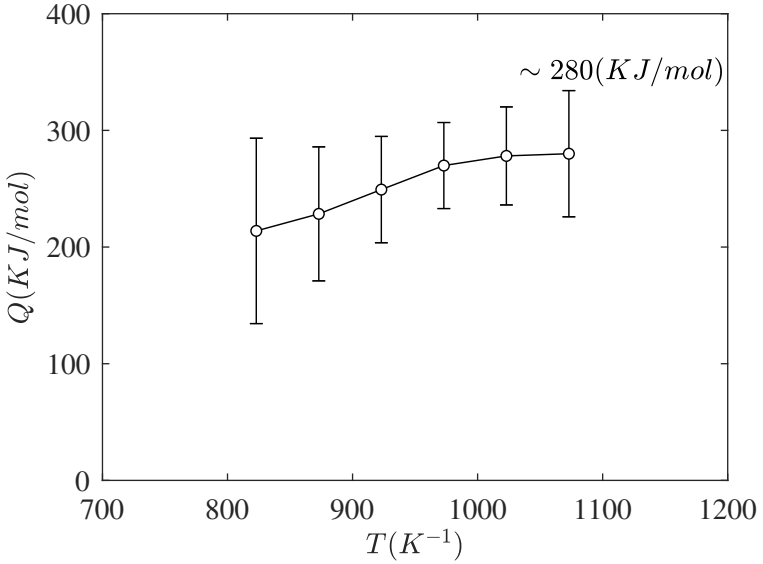

FIGURE 4.10: Dependency of activation energy to the temperature

Finally, remaining constants n and A in Eq. 4.2 must be calculated to calibrate the presented creep model. This goal is achieved by linearly fitting the double logarithmic plot

of normalized steady-state strain rate $\dot{\varepsilon}_{ss}kT/(DGb)$ versus normalized effective stress $(\sigma - \sigma_p)/G$ as shown in Fig. 4.11. Here $b = 0.248$ nm for α-Fe (Frost and Ashby, 1982) is assumed. The results show that for normalized effective stress less than 0.003, Eq. 4.2 gives acceptable results with $n = 4.75$ whereas stress exponent is greater than 8 for higher values of $(\sigma - \sigma_p)/G$. It can be argued that this behavior is due to the change in the creep mechanism from high temperature climb when $(\sigma - \sigma_p)/G < 0.003$, to low temperature climb when $(\sigma - \sigma_p)/G > 0.003$ (Cadek, 1988; Kaibyshev and Kazakulov, 2004).

At this stage the secondary creep model is calibrated and all constants are summarized in Table 4.4; subscript "2" denotes the values for steady-state creep with normalized effective stress greater than 0.003.

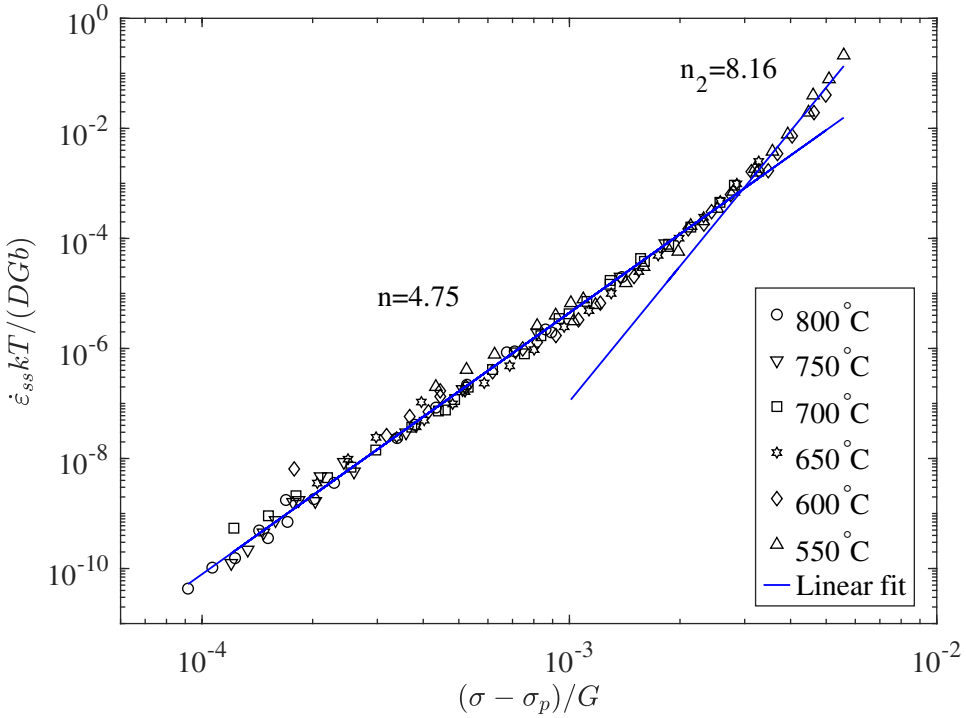

FIGURE 4.11: Plot of normalized strain rate against normalized effective stress

TABLE 4.4: Stady-state creep constants

B	Q_p	D_0	Q	n	A	n_2	A_2
	(KJ/mol)	(m^2/s)	(KJ/mol)				
5.69×10^{-7}	46.1	2×10^{-4}	280	4.75	7.9090×10^{8}	8.16	3.3390×10^{17}

Fig. 4.12 shows a comparison between results of calibrated creep model and experiment; fairly good concordance approve functionality of the proposed power law creep model and material constant identification procedure.

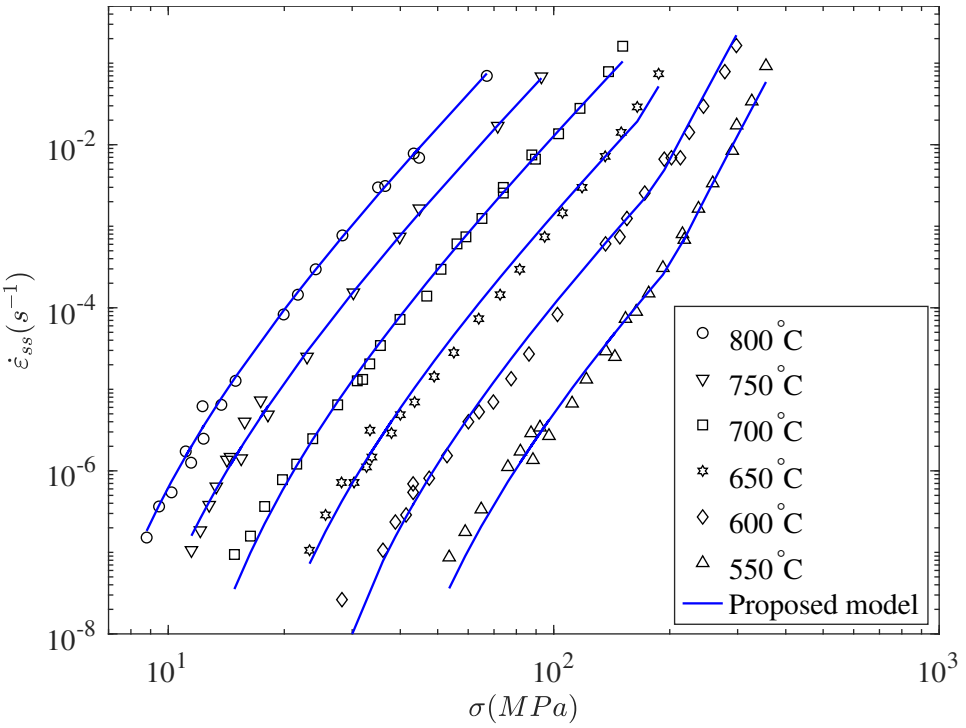

FIGURE 4.12: Variation of steady-state creep strain rate with stress at different temperatures: comparison between experimental data of (Kaibyshev and Kazakulov, 2004) and proposed model

The DCI cooling process is transient in nature because mechanical properties of the matrix and and the stress level of the RVE vary with temperature. In transient processes at high temperature and when the stresses are low (such as the RVE condition during cooling), in addition to secondary creep, primary creep must be considered to model the accumulation of creep strain (Sherby and Burke, 1968).

In this regard, Esposito and Bonora proposed a mechanism-based model to model primary creep (Esposito and Bonora, 2011). They suggested that transient creep strain rate is a function of the steady-state creep rate:

$$\frac{\dot{\varepsilon}}{\dot{\varepsilon}_{ss}} = \exp\left[\frac{\bar{\Omega}}{RT}\sigma \exp\left(-\frac{\varepsilon}{\varepsilon_0}\right)\right] \tag{4.5}$$

where $\bar{\Omega}$ and ε_0 are material parameters and denote the scaled activation volume and decay constant respectively, ε is creep strain and $\dot{\varepsilon}$ denotes creep strain rate. Based on their proposed model, for specified reference stress and temperature, the lower limit of creep rate in transient region is the steady-state creep. In the present work, this creep model is adopted to predict the transient creep strain of Fe-3Si material.

The constants of Eq. 4.5, including the scaled activation volume and decay constant, are identified from $\dot{\varepsilon} - \varepsilon$ curves. If the equation is rewritten in the following form:

$$\ln\left[\ln\left(\frac{\dot{\varepsilon}}{\dot{\varepsilon}_{ss}}\right)\right] = \ln\left(\frac{\bar{\Omega}}{RT}\sigma\right) - \left(\frac{\varepsilon}{\varepsilon_0}\right) \tag{4.6}$$

then $\bar{\Omega}$ and ε_0 are obtained by linear fitting of the plots of $\ln\left[\ln\left(\frac{\dot{\varepsilon}}{\dot{\varepsilon}_{ss}}\right)\right]$ against ε. More details on the method of parameter identification can be found in their work.

For the studied material, $\dot{\varepsilon} - \varepsilon$ data at 500°C and 600°C with two stress levels are available. These creep data are considered to obtain the material parameters in Eq. 4.6. The calculated values for the decay constant and scaled activation volume are plotted in Fig. 4.13 and Fig. 4.14, respectively.

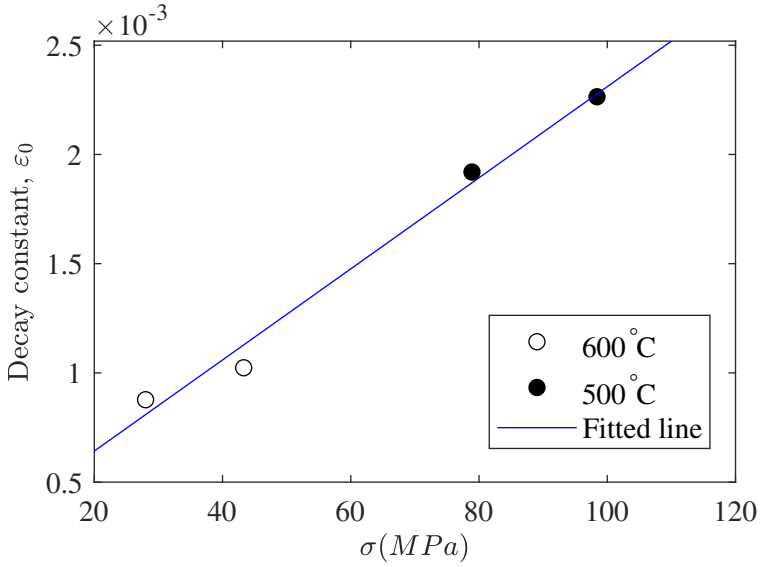

FIGURE 4.13: Variation of decay constant with applied stress at 500°C and 600°C

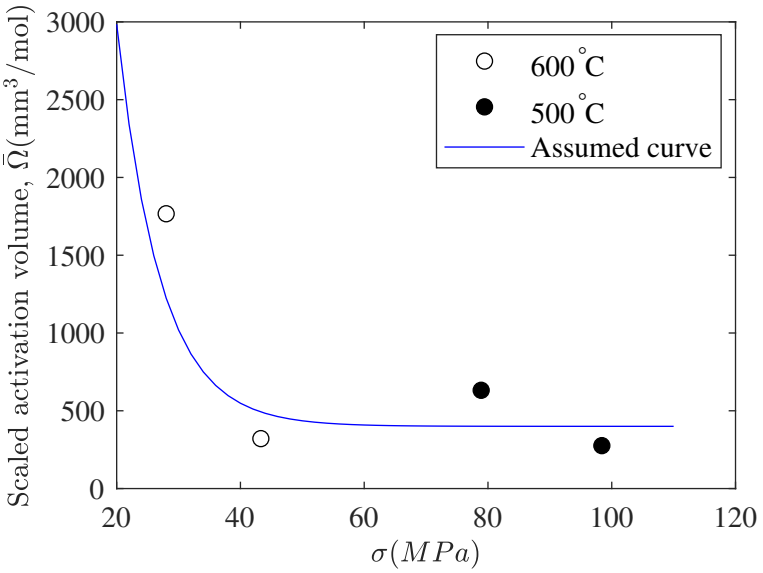

FIGURE 4.14: Variation of scaled activation volume with applied stress at 500°C and 600°C

Esposito and Bonora argued that $\bar{\Omega}$ and ε_0 are not dependent to temperature but are functions of applied stress (Esposito and Bonora, 2011). Fig. 4.13 indicates that the decay

constants obtained, vary linearly with the stress at least in the range considered. Therefore, a linear equation is used to model the evolution of ε_0 with stress:

$$\varepsilon_0 = \bar{\varepsilon}_0 + \frac{\sigma}{C_1} \tag{4.7}$$

where $\bar{\varepsilon}_0$ and C_1 are material constant and calculated by linear fit. Their values are reported in Table 4.5.

Evolution of calculated scaled activation volume with stress in Fig. 4.14 shows an exponentiation decay. Although data for lower stress levels are not available, the following equation may be assumed base on the trend of the data:

$$\bar{\Omega} = \Omega_0 + C_2 \exp\left(-\frac{\sigma}{C_3}\right) \tag{4.8}$$

where Ω_0, C_2 and C_3 are material constant. These constants are obtained by curve fitting and listed in Table 4.5.

TABLE 4.5: Transient creep parameters

$\bar{\varepsilon}_0$	C_1	Ω_0	C_2	C_3
(mm/mm)	(MPa)	m^3/mole	m^3/mole	(MPa)
2.2515×10^{-4}	4.7957×10^{4}	4.0×10^{-7}	4.5×10^{-5}	7

Here, the general creep strain rate model, in the form of Eq. 4.5, is calibrated. Fig. 4.15 shows that the presented creep model is able to acceptably describe the creep behavior of the material in both transient and steady-state stages.

4.2.3 Nodule

Nevertheless, the nodules, which are made of graphite and whose chemical composition and micro structure can be considered similar in all DCI grades, the behavior of the matrix depends entirely on the DCI material. Therefore, in this thesis, the matrix characteristics will be determined based on the selected DCI but identical parameters are presented for the nodules.

Experiments show a high melting temperature of graphite in the range of 3700-5000°C compared to its microstructure and measurement methods (Colonna et al., 2009). Despite its very high melting temperature, experimental research suggests that evolution of certain physical properties with temperature must be considered.

Among all the physical properties, one of the most important parameters for residual stress simulations is the coefficient of thermal expansion. Nelson and Riley experimentally measured the thermal expansion of graphite perpendicular,$\alpha_\perp$, and parallel,$\alpha_\parallel$, to the hexagonal crystal axis (Nelson and Riley, 1945). They proposed that the average value of linear thermal expansion ,$\bar{\alpha}$, can be calculated using Riley's relation (Riley, 1945):

$$\bar{\alpha} = \frac{2}{3}\alpha_\perp + \frac{1}{3}\alpha_\parallel \tag{4.9}$$

assuming that a graphite sample probably consists of small graphite crystals with random orientation. They suggested that graphite's mean CTE at room temperature is about

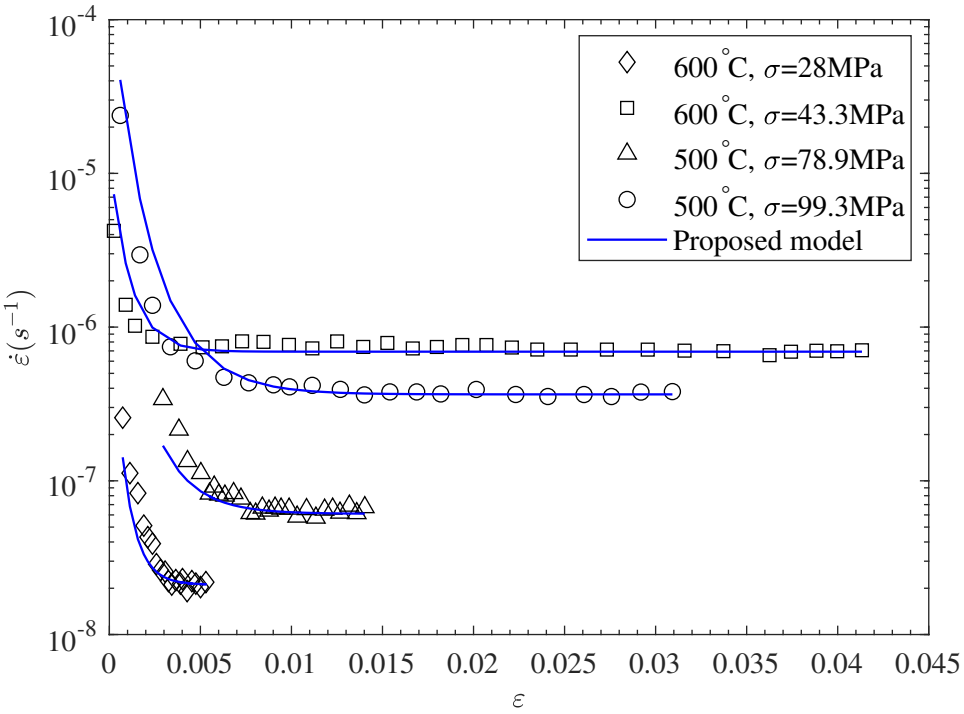

FIGURE 4.15: Creep strain rate versus creep strain: comparison between experimental data of (Kaibyshev and Kazakulov, 2004) and proposed model

$8 \times 10^{-6}\,°C^{-1}$. Adopting their $\alpha_{\perp}$ and $\alpha_{\parallel}$ data, the average CTE of graphite can be estimated at different temperatures by using Eq. 4.9. Fig. 4.16 presents the average CTE of graphite calculated by this method.

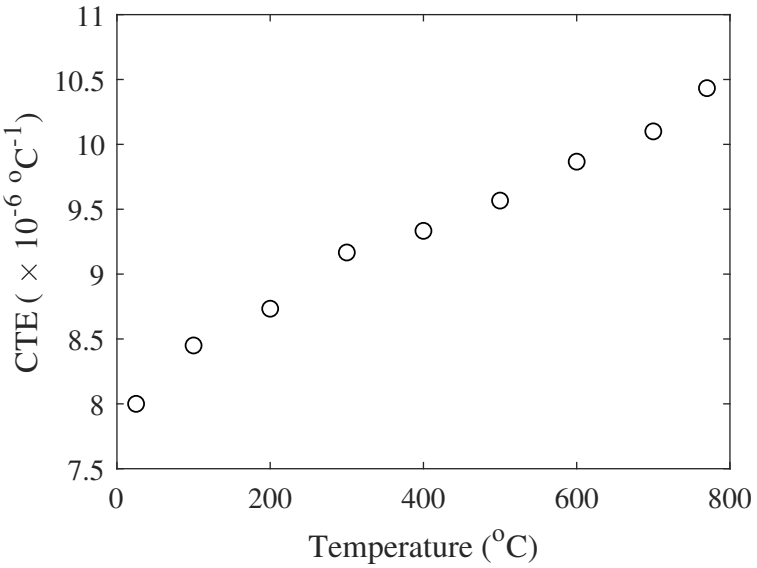

FIGURE 4.16: Variation of graphite mean CTE with tempratute

Based on the fact that the nodule is made of graphite, it is assumed that the CTE of

the nodule and its evolution with temperature is the same as that of the graphite material. Calculations show that at 769°C the CTE of graphite is 10.43×10^{-6} °C^{-1} that is much higher than its value at room temperature. Therefore, it is not recommended to assume that the CTE of the nodule is constant to calculate the residual stress around it.

One of the most difficult parts of this thesis is defining the mechanical properties of the nodules. In order to overcome this problem and find a reasonable solution, the following strategy has been applied:

1- Preliminary simulations reveal that the nodule deformation during cooling is trivial. Also, during mechanical loading such as uniaxial tension or simple shear, if the deformations are small, no significant difference in the RVE response is obtained by defining yield criterion for the nodule. Thus, in this chapter, behavior of the nodule is assumed to be elastic.

2- Due to the high melting temperature of graphite, it is assumed that its elastic constants are independent of temperature for the interested range of 25-800°C.

3- The elastic Young's modulus of the nodule is selected 27GPa, as measured experimentally from the hardness data of the nanoindentation test (Hervas et al., 2013; Pradhan et al., 2009).

4- The remaining nodule elastic property is its Poisson's ratio, PR. To find the nodule Poisson's ratio, the available data of DCI, matrix and nodule are taken into account. For this grade of DCI, PR equal to 0.28 is reported in the literature (Andriollo, Thorborg, and Hattel, 2016). Knowing the elastic properties of the matrix at room temperature (from JMatPro) and assuming the aforementioned value for Young modulus of nodule, an attempt is made to find the PR of the nodule that gives the correct PR for this DCI. To do this, DigiMat package with the mean-field approach is used. This gives a Poisson's ratio of the nodule equal to 0.22.

4.3 Micro model

Due to the small deformation of the RVE and the possibility of nodule-matrix separation in some loading cases, the micro model Corsp_RVE that was introduced in sections 3.1 is considered.

With respect to to the average nodule diameter and volume fraction, periodic length of the RVE is calculated L_0=49.7227 µm. This micro model can be used to predict the overall mechanical behavior of the DCI under different loading conditions. In addition to this model and to compare the numerically calculated local residual stresses with the experimental measurements of Zhang et al. (Zhang et al., 2016) another micro model with a nodule diameter of 50 µm is created. This diameter is equal to the diameter of "nodule A" in their work. In this case, L_0=82.8712 µm is assumed to keep the average volume fraction. But, comparison of the results of these two micro models confirms that the scaling of the RVE has no effect on the simulation of the residual stress. Therefore, the micro model respecting the average nodule diameter is also considered for residual stress simulations.

In the micro model, the periodic boundary condition introduced in sections 3.2 and the finite element homogenization presented in sections 3.3.2 are considered.

Knowing the elastic properties of the matrix and nodule, and using the DigiMat package with the Mean Field (MF) approach, the elastic constants of DCI at different temperatures can be calculated. At room temperature Young's modulus and Poisson's ratio of RVE are obtained 167.8GPa and 0.28 respectively. These values are consistent with the elastic constants of this grade of DCI (Andriollo, Thorborg, and Hattel, 2016; Andriollo et al., 2016) and the general properties of DCI (Ductile Iron Society, 1990; American Foundrymen's Society, 1993). For higher temperatures, the experimental data of Delprete and Sesana (Delprete and Sesana, 2014) are considered. They measured the Young's modulus of Si-Mo-Cr ductile cast iron in the range between room temperature and 800°C. According to their measurements, at room temperature, the material has a Young's modulus equal to 178GPa. To compare the results of the MF model with their measurements, the data are normalized to the Young's modulus at room temperature, E_0. Fig. 4.17 shows the variation of the normalized Young's modulus, E_T/E_0, with temperature where E_T denotes Young's modulus at selected temperatures. The satisfactory agreement between the MF model and the room temperature experiment at 800°C confirms that the Young's modulus assumed for the matrix and nodule provides acceptable results for the DCI.

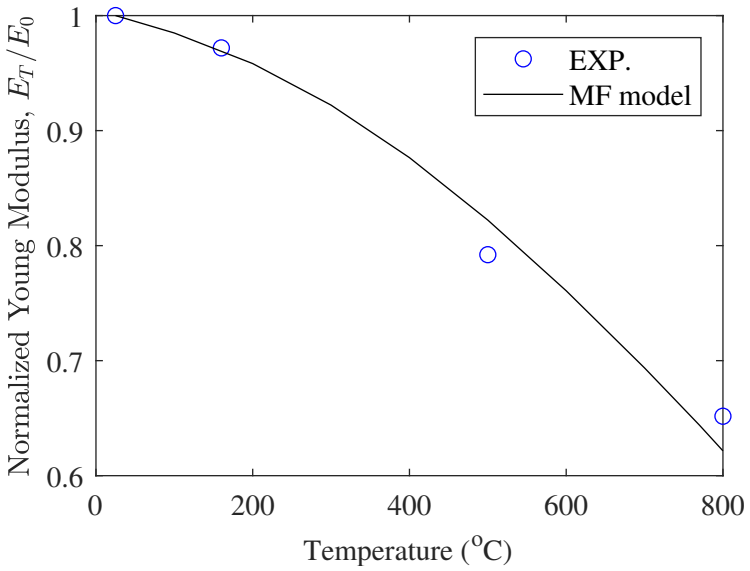

FIGURE 4.17: Variation of DCI Young's modulus with temperature

4.4 Finite element method

Numerical results are obtained from thermomechanical simulations using the MSC.MARC finite element software package. Although the deformations are trivial for the calculation of the residual stresses of the RVE, an updated Lagrangian approach is adopted to update quantities such as the current volume at the integration points, which is necessary to obtain homogenized stresses and strains of the RVE. This approach not only provides the required variables in the current configuration but also gives an accurate solution for small deformations.

The interface between the nodule and the matrix is modeled by a contact surface. It is assumed that there is no chemical bond between the nodule and the matrix. The friction between the contact surfaces follows the bi-linear shear's law with a coefficient of 0.2. The contact properties involve node-to-segment contact with the deformable-deformable method and double side check with optimized contact constrains is used. The microscale numerical study includes two steps: *Cooling* and *Mechanical loading*.

4.4.1 Cooling

The simulations start from this step where the local residual stresses in the RVE are formed. The cooling process starts at 769°C as discussed in sections 4.2.2. This temperature is introduced as the initial thermal condition at all nodes of the micro models. Then, the RVE temperature is uniformly reduced to room temperature.

During cooling, the mismatch of the CTE of the nodule and the matrix causes thermo-mechanical interactions between them and leads to the formation of local residual stresses; a larger CTE of the matrix causes a larger volumetric contraction with respect to the nodule but the boundary condition of the interface acts as a barrier to this volumetric contraction and concludes local strains in the matrix. These local strains introduce local residual stresses in the RVE.
Since the cooling rate is of importance in creep strain calculations, the temperature variation of the RVE with time is adopted to be the same as the cooling curve presented by Andriollo et al. (Andriollo et al., 2018) and is shown in Fig. 4.18.

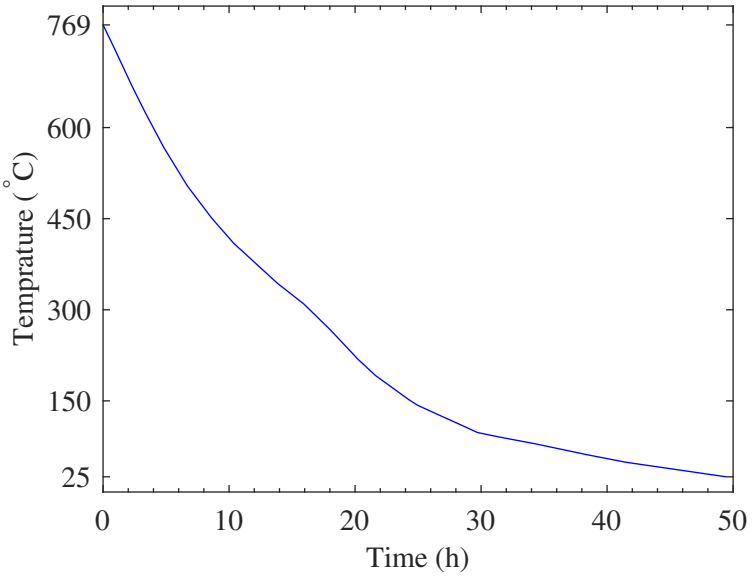

FIGURE 4.18: Cooling curve of the DCI

The viscosity with implicit solution method is adopted to calculate the inelastic deformation of the matrix where the creep strain rate is introduced by the subroutine Ucrplw. The boundary conditions include: 1- fixed origin of the RVE 2- $U_{xy} = U_{yz} = U_{zx} = 0$, in order to avoid the unintentional motion of the rigid body and rotation respectively. It should be explained that, although during cooling the sliding motion between the die and nodule

surfaces is not remarkable, the definition of friction may be necessary to avoid probable undesired rotation of the nodule. Therefore, the value of the friction coefficient can be chosen arbitrarily at this step.

It should be emphasized here that the dimensions of the VRE should be scaled to obtain, at the end of cooling, the actual diameter and volume fraction of the nodule. The post-processing of the results includes the calculation of the CTE, the residual inelastic strain on a predefined trajectory and the current volume of the nodule and the RVE is performed by a python script at each increment.

4.4.2 Mechanical loading

In this step, the mechanical behavior of the micro model under different loading conditions is studied. This step is carried out at room temperature and starts after finishing the cooling step. Therefore, at the beginning of this step, the RVE contains residual stresses. The boundary conditions for desired cases, uniaxial loading and simple shear, are presented in Eqs. 3.11b and 3.12b, respectively. For post-processing, a python script is written to compute the homogenized stress and strain fields of the nodule, matrix and RVE.

4.5 Results and discussion

Stress contours at mid range and ambient temperatures are plotted in Fig. 4.19 where 1/8 of model is removed for better presentation of the RVE interior. Numerical results indicate that as cooling continues, residual stresses evolve to reach maximum values at the end of cooling while excessive local stresses cause visco-plastic behavior of the matrix. It should be noted that the lower Young's modulus of the nodule relative to the matrix reduces the local residual stresses in some way.

The distribution of the stress component along the z axis, σ_z, shows that the maximum residual stress is created near the interface and in the matrix (Figs. 4.19a and 4.19b). The residual stress reduces to its minimum value on the RVE surface which is not a free surface due to the periodic condition.

The contours of the hydrostatic stress, σ_h, at two different temperatures are shown in Figs. 4.19d and 4.19d. Again, the higher CTE of the matrix imposes pressure on the the nodule since the matrix contracts more than the nodule during cooling. The results show that this pressure is uniform across the nodule and increases with continued cooling to room temperature. For the matrix, the reaction forces at the interface create a negative mean stress adjacent to the nodule. But, the sign changes and the amount increases away from the interface.

As depicted in Figs. 4.19e and 4.19f, effective deviatoric stress, σ_{eds}, inside the matrix increases with decreasing RVE temperature, but its gradient is not uniform throughout the matrix. The maximum local stresses appear around the interface and they gradually reduce with moving toward the surface. Due to the fact that the RVE is a cube while nodule has spherical shape, not all surface nodes have the same distance to the interface and therefore the distribution of the equivalent stresses on the RVE surfaces is not uniform.

The study of the residual stresses inside the nodule shows that the equivalent stress inside the nodule is trivial and it sustains mainly a uniform hydrostatic pressure because of its spherical shape (Fig. 4.19). Fig. 4.20 shows the equivalent stress on the surface and

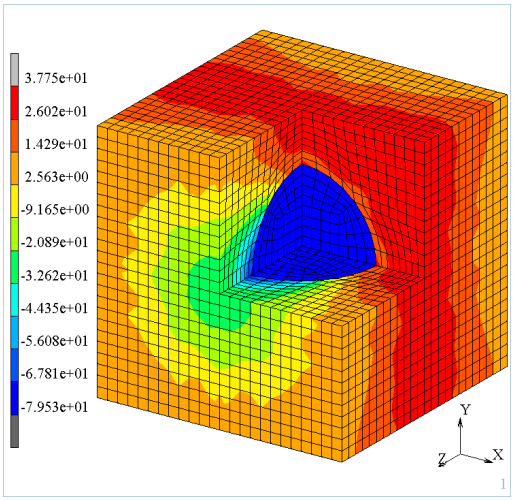

(a) σ_z @ 378°C

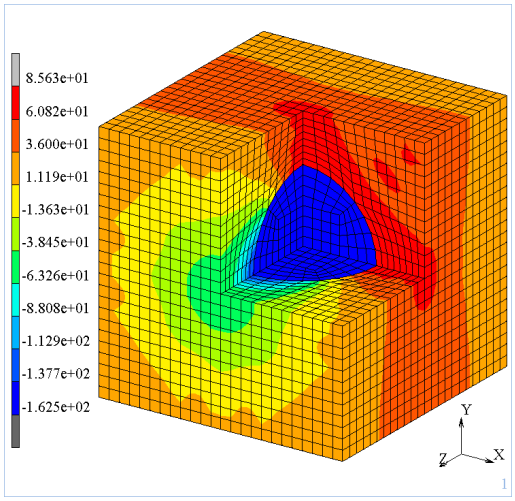

(b) σ_z @ RT

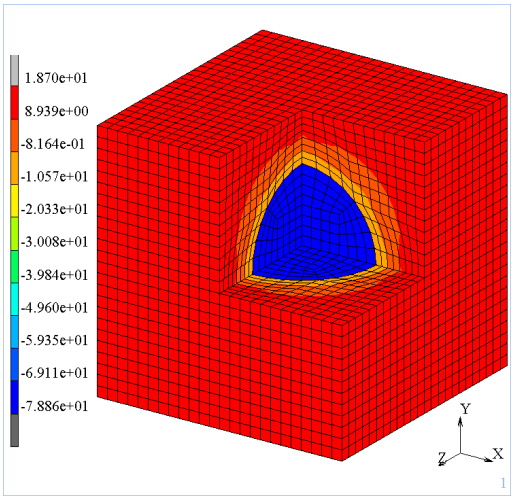

(c) σ_h @ 378°C

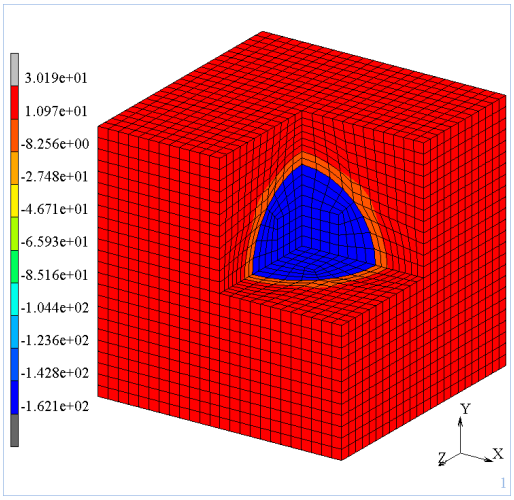

(d) σ_h @ RT

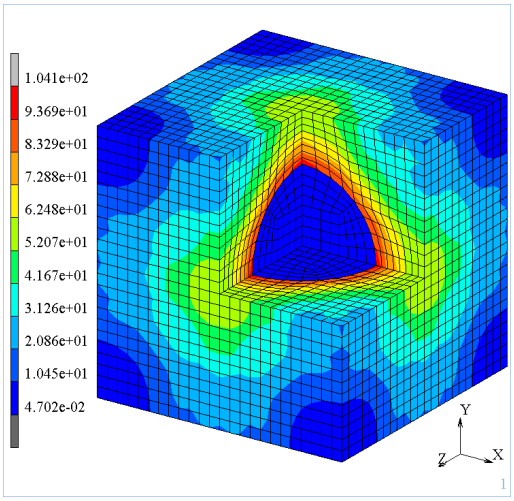

(e) σ_{eds} @ 378°C

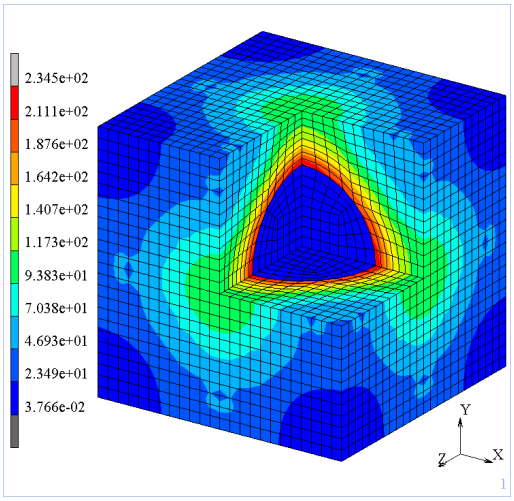

(f) σ_{eds} @ RT

FIGURE 4.19: RVE stress during cooling

inside the nodule at the end of cooling where 1/8 of the nodule is removed for convenience. The figure reveals that the maximum local equivalent stress does not exceed 6 MPa at some locations on the surface, which is mainly due to map of the mesh and the use of touch contact for the interface. However, the equivalent stress is negligible inside the nodule. Therefore, it can be concluded that the nodule deformation during the cooling can be considered elastic and it sustains only hydrostatic pressure.

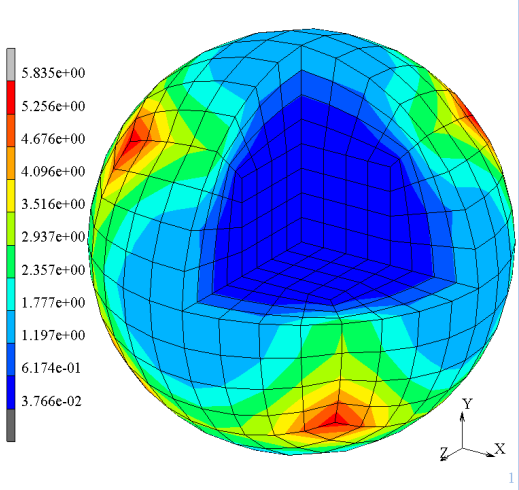

FIGURE 4.20: Equivalent von Mises stress of nodule at the end of cooling

Using the updated Lagrangian method in FE solutions, the total volume of the RVE can be calculated simply by summing all the integration point weights. Therefore, the volume change of the RVE can be incrementally obtained to calculate the volumetric coefficient of thermal expansion, γ, by the following relationship:

$$\gamma = \frac{1}{V_{RVE}} \frac{\Delta V_{RVE}}{\Delta T} \tag{4.10}$$

where ΔV_{RVE} represents the change in volume of the RVE due to increment of temperature (ΔT).

The coefficient of linear expansion can be obtained simply by one-third of γ. Therefore, the change in the CTE of the RVE can be calculated incrementally during cooling. Fig. 4.21 shows the CTE evolutions of the matrix, the nodule and the RVE. Due to the fact that nearly 90% of the volume of the unit cell is matrix, the CTE of the RVE remains close to that of the matrix. However, some numerical errors in the calculation of the RVE volume, when the creep card is active through the subroutine, may affect the results in the range of 550-769°C. It should be mentioned that since the elastic properties of the nodule and matrix are not similar, the CTE of the RVE cannot be calculated directly using the rule of mixture.

Differential-Aperture X-ray Microscopy (DAXM) technique is used by Zhang et al. (Zhang et al., 2016) to measure residual elastic strain field in the matrix. They experimentally calculated the elastic strain,ϵ^{el}_{FF} , along the F-axis in the neighborhood of three nodules they named "A", "B" and "C". More details about coordinate system, x-ray direction and measuring specifics were presented by Andriollo et al. (Andriollo et al., 2018); Fig. 4.22 show plan and direction of measurements, as reported in their work.

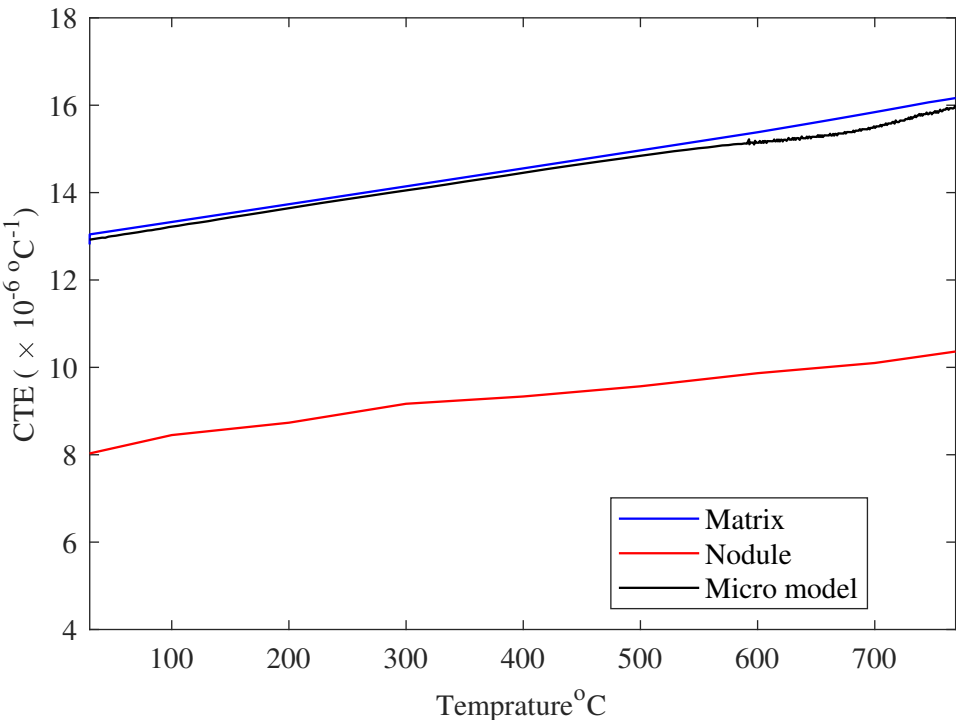

FIGURE 4.21: CTE variation during cooling

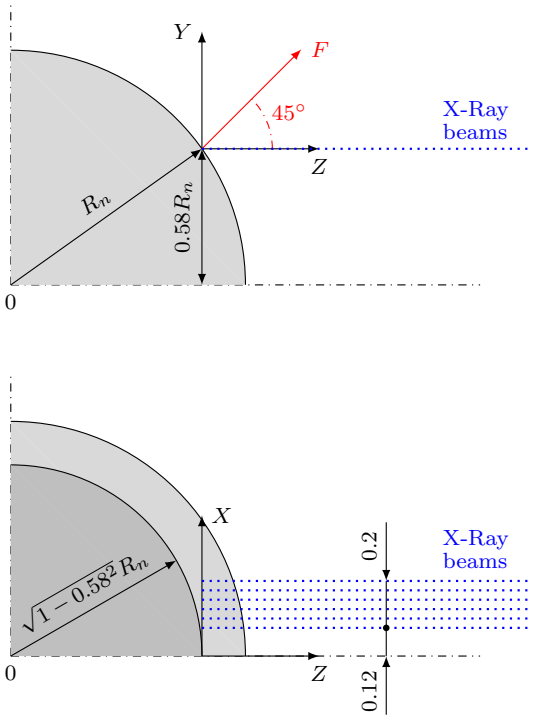

FIGURE 4.22: Reference system for X-ray measurements of elastic residual strain

At the end of cooling stage, residual elastic strain in the matrix is obtained and compared with the experimental measurements in Fig. 4.23.Experimental data are digitized from the work of Andriollo et al. (Andriollo et al., 2018) where they represented the residual elastic strain in the adjacent of nodule A. Although in the work of Zhang et. al (Zhang et al., 2016), measurements are also available for two other nodules, "B" and "C", these were not considered because the nodules are very close to each other, a circumstance that distances the local morphology from the modeled periodic structure.

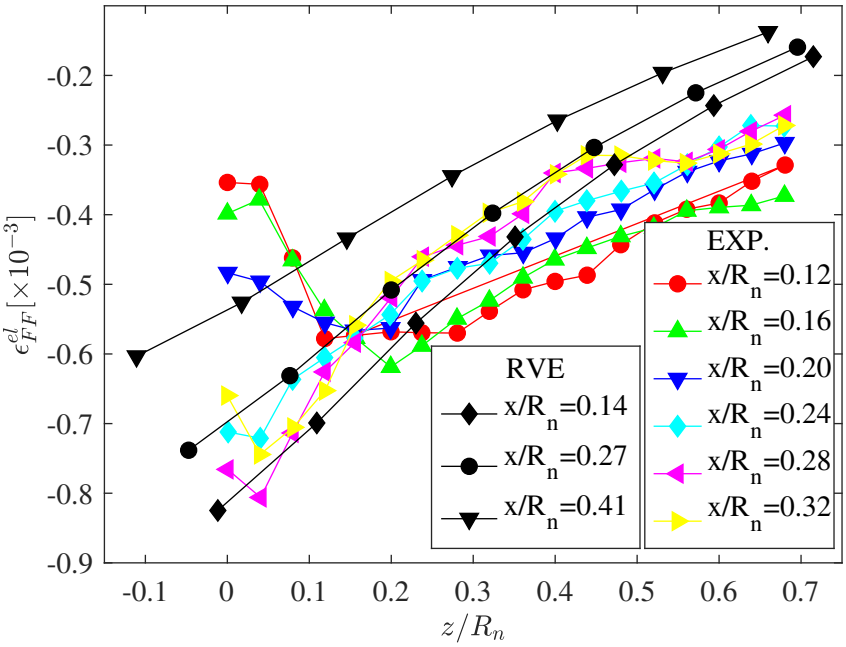

FIGURE 4.23: Local residual stress measurement: comparison between experimental data and micro model

The numerical results are taken at the nodes of the mesh, from the nodule-matrix interface, approximately on the same plane (due to the round shape of the nodule, they are not exactly on the same plane) and on lines parallel to those of the X-Ray beams. The figure suggests that the minimum and trend of residual elastic strain of the RVE are considerably close to the test data; the simulated residual elastic strain has its minimum at the interface and gradually increases with distance from the nodule. In addition, the more the distance along the x axis, the less the residual elastic strains. However, the experimental results show a reversal for values of z/R_n ranging from 0.3 to 0.04, depending on the position x/R_n. In accordance with the definition of the reference system and the effective size of the nodule under consideration (50 mum in diameter), the region affected by the inversion can be identified with a shell surrounding the nodule with a thickness of about 2 to 5 mum. The reason for such a trend is unclear, Andriollo et al. (Andriollo, Fæster, and Winther, 2018) argued that the figure may be fictitious because the measurement could be affected by the sharp gradients in chemical composition. Indeed, the latter, as reported by Levine et al. (Levine,

Okoro, and Xu, 2015), affects the value of the unstrained lattice spacing used as reference to calculate the experimental strain. Finally, it is worth mentioning that, experimentally, such a trend was not observed around the "B" and "C" nodules. These results confirm that although a very simple model was selected for RVE, it can reasonably calculate the residual stresses in the DCI.

The effect of creep on the final residual elastic strains is discussed in Fig. 4.24. In this figure, "No Creep" refers to the micro model without creep and "Pr+Sc Creep" presents the results of RVE with primary and secondary creep (integrated model). As expected, creep leads to stress relaxation phenomenon and the predicted residual elastic strains considering creep are lower than "No Creep" model and closer to the experiments. The minimum creep strain without creep is calculated -0.984×10^{-3} while this value is -0.855×10^{-3} for the integrated model; the relative error is 15%. Therefore, it is concluded that in order to study the local residual elastic strains in the DCI, visco-plastic model with an appropriate creep model should be used.

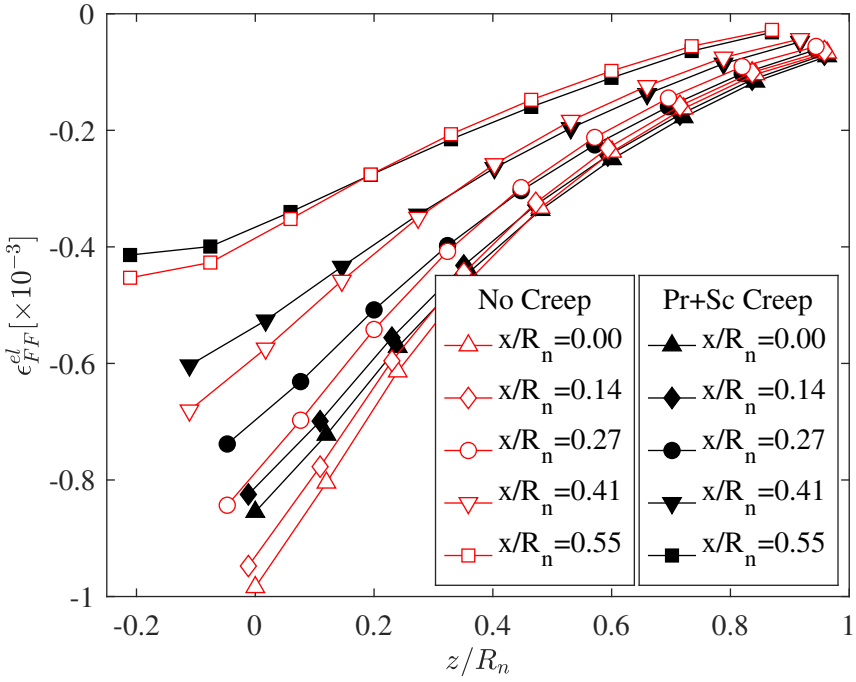

FIGURE 4.24: Effect of creep strain on the final residual stresses

To investigate the effect of primary creep on the final residual elastic strains, the results of the integrated RVE (with primary and secondary creep) are compared to the RVE with only secondary creep. This comparison is performed in the Fig. 4.25 where "Sc Creep" refers to the micro model in which only secondary creep is considered for creep strain calculations. The figure indicates that the effect of primary creep is trivial; in this case, the minimum creep strain of the "Sc Creep" model is obtained -0.888×10^{-3} which introduces the relative error of about 3.9% compared to the integrated model. This shows that for the studied micro model, the stress relaxation in the transient region of the creep model is negligible.

Fig. 4.26 shows gradual formation of residual elastic strain during cooling for a point on the interface with $z/R_n = -0.0116$ and $x/R_n = 0.14$.

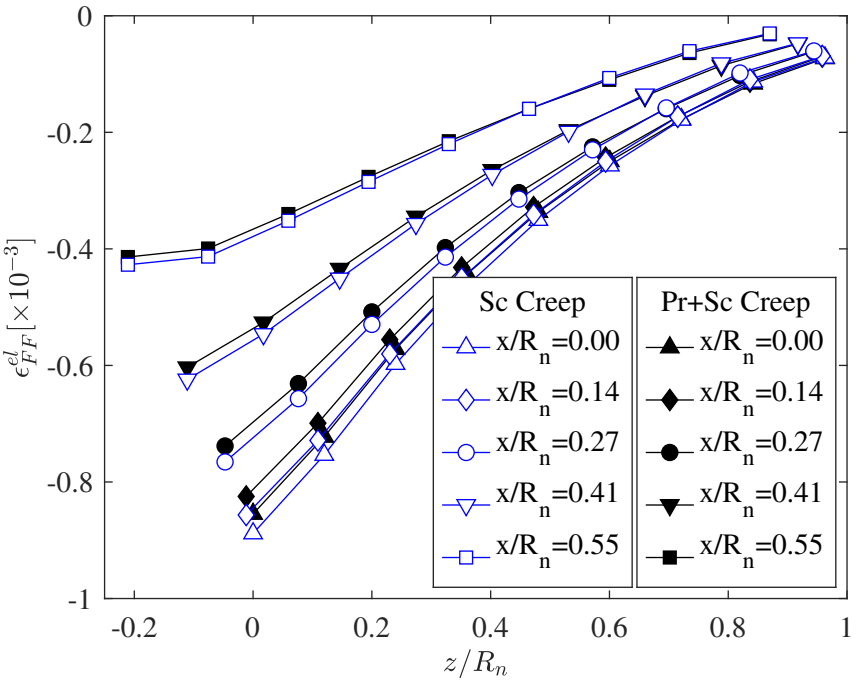

FIGURE 4.25: Effect of primary creep strain on the final residual stresses

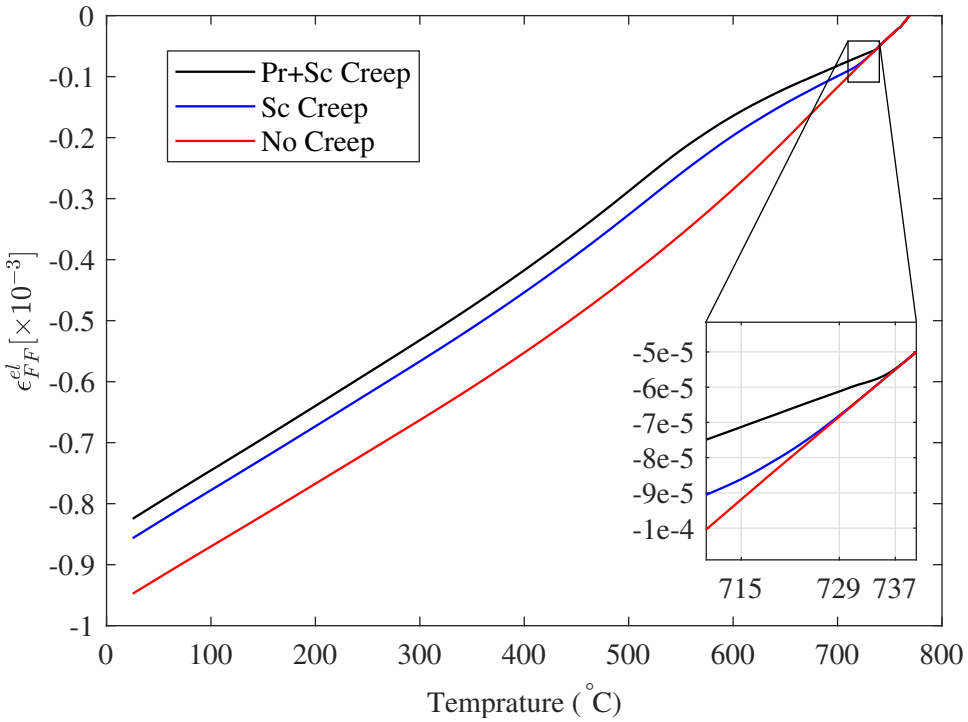

FIGURE 4.26: Formation of residual elastic strain during cooling

If creep is ignored in the simulation,the rate of residual elastic strain formation decreases continuously but gradually over the temperature range, as can be seen in the "No Creep" model. Indeed, the rate of residual elastic strain formation decreases from $1.719 \times 10^{-6}(1/°C)$ for for a temperature above 737°C to $1.044 \times 10^{-6}(1/°C)$ for a temperature below 50°C. At 550 °C elastic strain is calculated to be -0.359×10^{-3}.

For the integrated model with primary and secondary creep ("Pr+Sc Creep" model), stress relaxation with time can be seen for the temperature above 550°C. Therefore, the formation of elastic strain due to CTE mismatch of nodule and matrix, is partially eliminated with stress relaxation effect. It should be noted here that for the temperatures above 737 °C, the stress level is below the threshold stress and creep is inactive, so the results are identical to those of the "No Creep" model. The rate of elastic strain formation is reduced to $0.738 \times 10^{-6}(1/°C)$ for a temperature between 700-737 °C due to relaxation effect of the creep. As the temperature of the RVE decreases, the creep effect gradually slows down and this rate increases until it reaches $1.171 \times 10^{-6}(1/°C)$ for a temperature between 550-580 °C. At 550 °C the elastic strain is obtained -0.221×10^{-3}. For the temperatures lower than 550°C the creep is negligible and the trend and strain formation rate are similar to "No Creep" model. For instance, the rate of elastic strain formation is $1.067 \times 10^{-6}(1/°C)$ fora temperature below 50°C that is close to the "No Creep" model. Obviously, because it has higher residual elastic strain at 550°C due to the creep, arrives at a higher value at room temperature.

If only the secondary creep is considered, "Sc Creep" model, the creep is active for the temperatures below 737 °C like the integrated model. But the amount of creep strain is significant for temperatures below 729 °C. Hence, ignoring transient creep causes less stress relaxation in this temperature range. At 729 °C elastic strain is -0.068×10^{-3} as for the "No Creep" model while for the integrated model it is 0.061×10^{-3}. The effect of primary creep disappears by decreasing the temperature and creep effect. Therefore, the lower the temperature, the smaller the difference between the results of the "Sc Creep" model and the integrated model. For temperatures below 550°C the difference remains unchanged. This shows the importance of considering primary creep in the simulation of the cooling process.

The formation of irreversible deformations in the matrix is limited to the high temperatures, when the yield strength of the material is low enough to be overcome by the nodule reaction forces at the interface, as shown in the graph Fig. 4.27.

Obviously, with the presence of creep, the relaxation effect reduces level of stress required to exceed the yield strength and, consequently formation of plastic strains is stopped earlier. In the case of the full creep model, it stops at 730°C with the value of 3.6×10^{-5} while without primary creep occurs at 708°C with 5.4×10^{-5}. If creep is neglected, the formation of plastic strain continues for lower temperatures while in this case it stops at 670°C with the maximum value of 8.3×10^{-5}.

In the Fig. 4.28, the irreversible strain, calculated at the end of the cooling, is plotted as a function of the distance from the nodule normalized to its radius. Clearly, the maximum plastic strain occurs at the interface where the nodule less contraction respect to the matrix acts as an obstacle and therefore zones that are closer to this obstacle undergo more deformations. In the same graph, the dislocation density measured by Zhang et al. (Zhang et al., 2016) for the same locations is given. Probably, the strain level is too low to speculate on a comparative analysis between these two quantities. However, the qualitative finding is consistent.

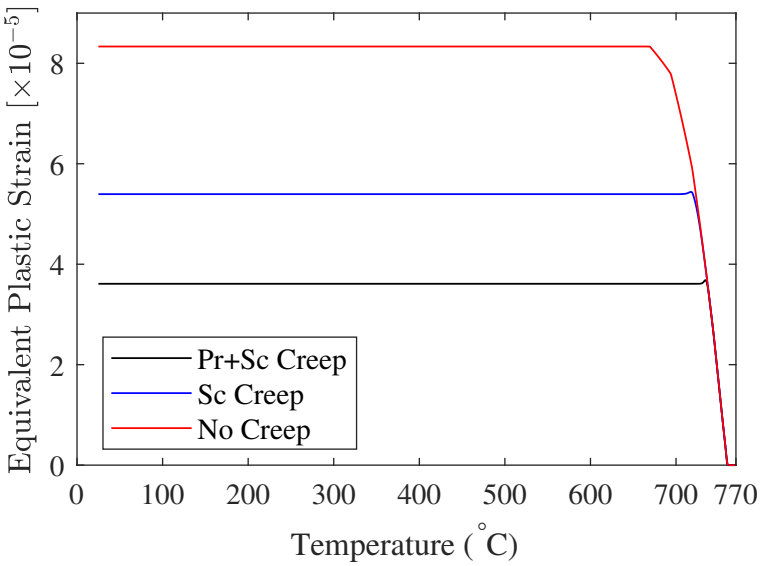

FIGURE 4.27: Formation of equivalent plastic strain during cooling

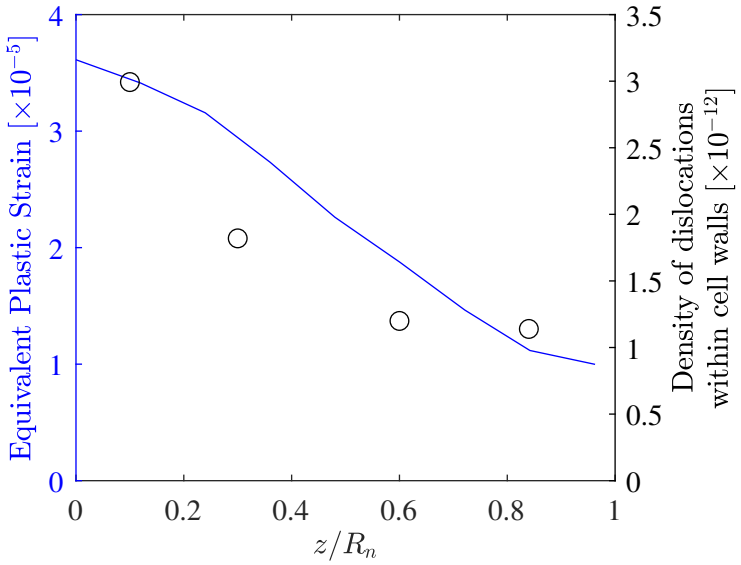

FIGURE 4.28: Change in dislocation density and equivalent plastic strain with the normalized distance from nodule interface

Fig. 4.29 shows the contours of the plastic deformation in the micro model at two different temperatures. At 750°C, only 19°C less than starting temperatures, uniform plastic deformation can be observed around the nodule in the Fig. 4.29a. The maximum value is found at the interface and gradually disappears with increasing distance from interface and there is no irreversible deformation on the surface of the RVE. Fig. 4.29b shows the contours of the plastic deformation at room temperature. The maximum value at the interface is higher than the value at 750°C, but it decreases again with distance from the interface. Therefore, some zones of plastic deformation can be observed on the RVE surface.

In the following, the response of the RVE under different loading conditions is studied.

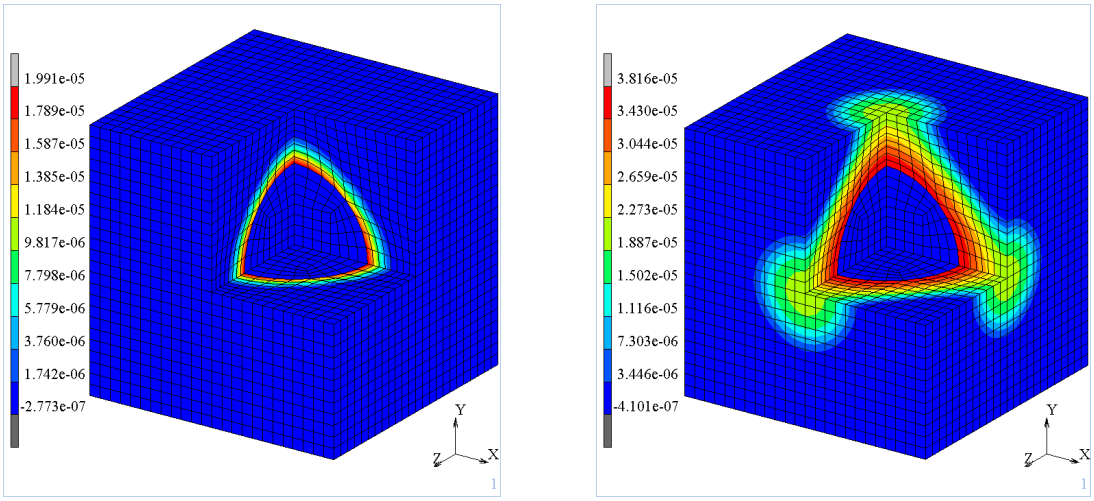

(a) σ_z @ 750°C (b) σ_z @ RT

FIGURE 4.29: Distribution of equivalent plastic strain during cooling

For each case, three different models are regarded to study the effect of the residual stresses on the RVE response: 1- "Integrated model" shows the RVE that undergoes cooling including creep followed by mechanical loading 2- "No creep" model shows the RVE that is similar to the integrated model but the creep is ignored in the cooling phase and 3- "No RS model" shows the RVE that directly undergoes mechanical loading without initial residual stresses. Fig. 4.30 shows true stress versus true strain curve of the RVE when the mechanical loading is uniaxial tension. As can be seen, residual elastic strains at the end of cooling affect the knee part of the curve. In the absence of negative residual stresses, the post yield zone of No RS model is higher than that of the other models. However, as loading continues, the difference vanishes due to elimination of compressive residual stresses. The initial part of the true stress-strain curves at least for stress levels below 200MPa is linear. The slope of this line is calculated to be 170.9GPa for the integrated model, which is close to the assumed value of 167.2GPa. But if residual stresses are ignored, this slope increases to 196.8GPa for the No RS model, which is far from the actual Young's modulus of the DCI. This shows the value of considering residual stresses in the response of the RVE.

It can be figure out that role of creep strains in the mechanical behavior of RVE is not significant. Similarly, the comparison of the results with the experimental data measured by Andriollo et al. (Andriollo et al., 2019) does not provide good results. This can be explained by the use of a miniaturized sample in the test.

True stress-strain curve of the RVE under uniaxial compression is depicted in Fig. 4.31. It can be seen that compared to the No RS model, compressive residual stresses shift the knee part of the curve downward. This effect is not significant and is only observed in the post yield region and disappears when the compressive load causes more compressive stresses in the RVE. Again, here the effect of creep strain on the compressive behavior of the micro model is insignificant.

The shear stress versus shear strain curve of the micro model is plotted in Fig. 4.32. Unlike the uniaxial loading cases, the residual stresses affect a larger portion of the curve. In the initial part of the post-yield curve, the No RS model shows more hardening but for the shear strain higher than 0.005 its curve is lower than other models. However, the difference

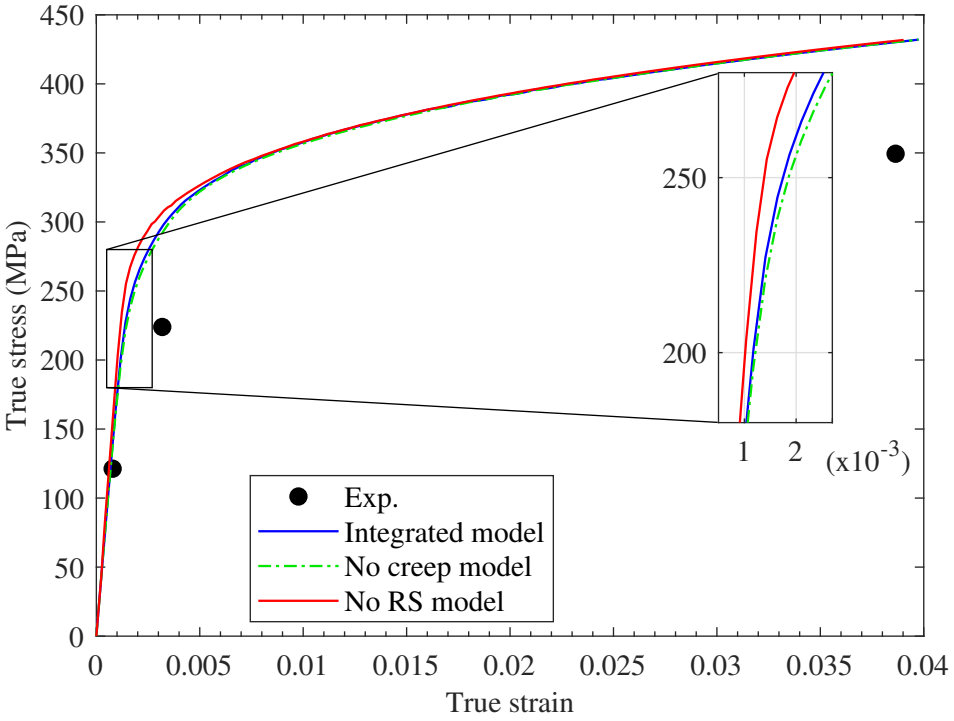

FIGURE 4.30: True stress against true strain curve of DCI under uniaxial tension

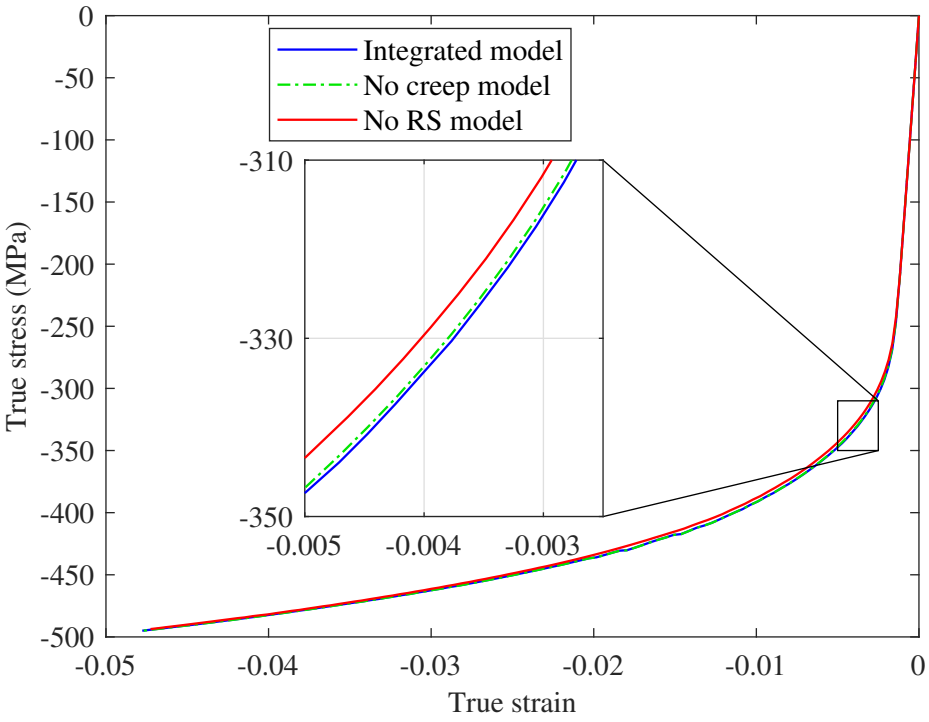

FIGURE 4.31: True stress against true strain curve of DCI under uniaxial compression

reduces as the shear loading continues. The results show that for shear stress levels below 120MPa, the relationship between shear stress and shear strain is linear. The slope of this linear part is 65.78GPa and 70.23GPa for integrated model and No RS model respectively. The shear modulus for the DCI is obtained 65.78GPa based on its Young'smodulus and Poisson's ratio. Clearly, if residual stresses are considered, shear modulus of micro model is very close to that of the DCI, which again confirms the importance of RS in the RVE simulations. This figure shows the negligible effect of creep strain on the RVE response.

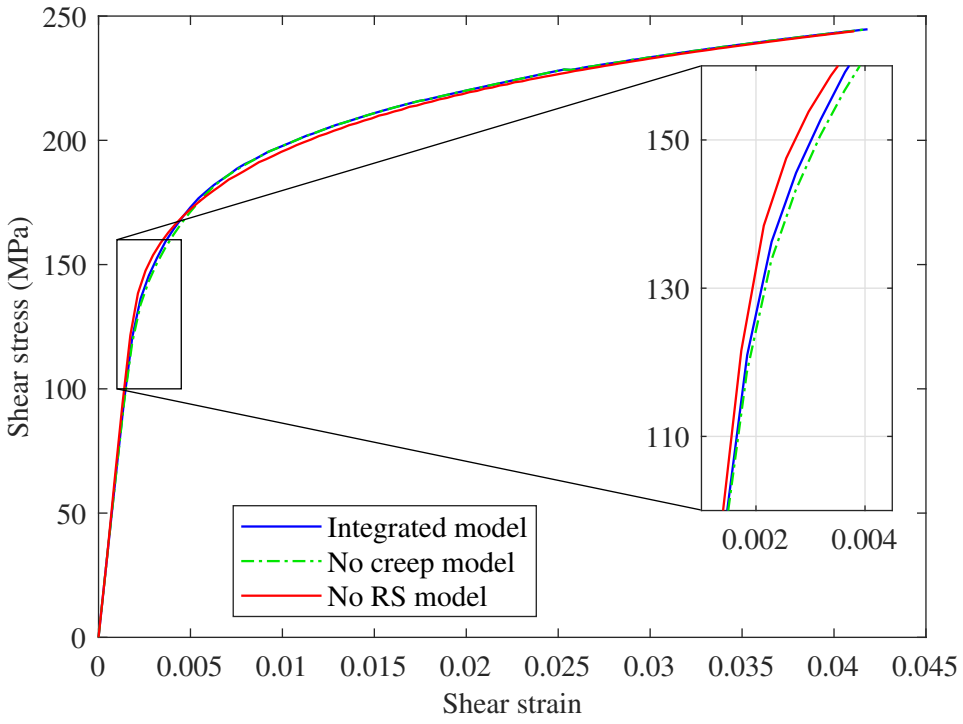

FIGURE 4.32: True stress against true strain curve of DCI under simple shear

Chapter 5

Micromechanical study: nodule characteristics

5.1 Micro model

In this chapter, the micro mechanical response of DCI Hervas under different mechanical loading conditions is investigated to calibrate mechanical properties of the nodules. The mechanical loads consist of: uniaxial tension and local compression conditions which were introduced in sections 2.4. In the tensile loading, due to the separation between the nodule and the matrix, the micro model called Corsp_RVE is considered. Micro model Comp_RVE is selected for the compressive loading cases where the RVE undergoes huge deformations. These models have been presented previously in sections 3.1.

For the DCI under study, experimental measurements revealed that the graphite nodules are distributed throughout the DCI with an average diameter of 16.8 µm and a standard deviation of 6.4 µm (Hervas et al., 2013). The Aspect Ratio (AR) of nodule follows a normal distribution with a mean value of 1.23 and a standard deviation of 0.35. Therefore, the nodule is modeled by a sphere using this reference diameter. The JMatPro results reveal that DCI at room temperature consists of 8.87% graphite volume fraction. Given this graphite volume fraction and the calculated diameter of the nodule, the periodic length of the RVE is calculated L_0=30.36 µm.

5.2 Constitutive thermo-mechanical models

At the microscopic scale, the thermomechanical properties of the RVE are governed by its components. So, appropriate constitutive models must be introduced to present an acceptable RVE model. To also account for the residual stresses that form in the cooling phase of the DCI manufacturing process, the effect of temperature on the behavior of the micromodel is considered. In the following, two different models are proposed for the RVE constituents.

5.2.1 Matrix

As mentioned in section 5.1, RVE contains 8.87% volume fraction of graphite. Therefore, the matrix composition can be calculated by deducing the graphite nodule from the composition of the DCI. Furthermore, the experiments show that for the studied DCI, the average grain size of ferrous matrix is 10 µm (Hervas et al., 2013). With knowing these information, JMatPro is used to simulate the solidification process and calculate the microstructure of the

matrix. The chemical composition of the matrix at room temperature is reported in Table 5.1 where Sn and Mg are not take into account in the calculation with JMatPro.

TABLE 5.1: Chemical composition (in wt.%).

Si	C	S	Mg	Mn	Cr	Mo	Sn	Cu	P
4.3642	0.1594	0.0051	0.0288	0.2264	0.0720	0.6279	0.0093	0.0206	0.0206

Table 5.2 shows the matrix phases at room temperature. The distribution of the phases implies that in matrix, volume percentage of the pearlite is equal to 13.09%. Change of matrix solid fractions with temperature is presented in Fig. 5.1 that shows lower eutectoid temperature, T_L of 824°C. Here, as in the discussion in section 4.2.2, this temperature is considered as starting point of the cooling process in the simulations.

TABLE 5.2: Phases in matrix(in wt.%); Fe: balance.

	wt.%	Vol.%
Ferrite	97.05	96.97
Cementite	1.64	1.62
M6C	1.29	1.38
MNS	0.0138	0.0258

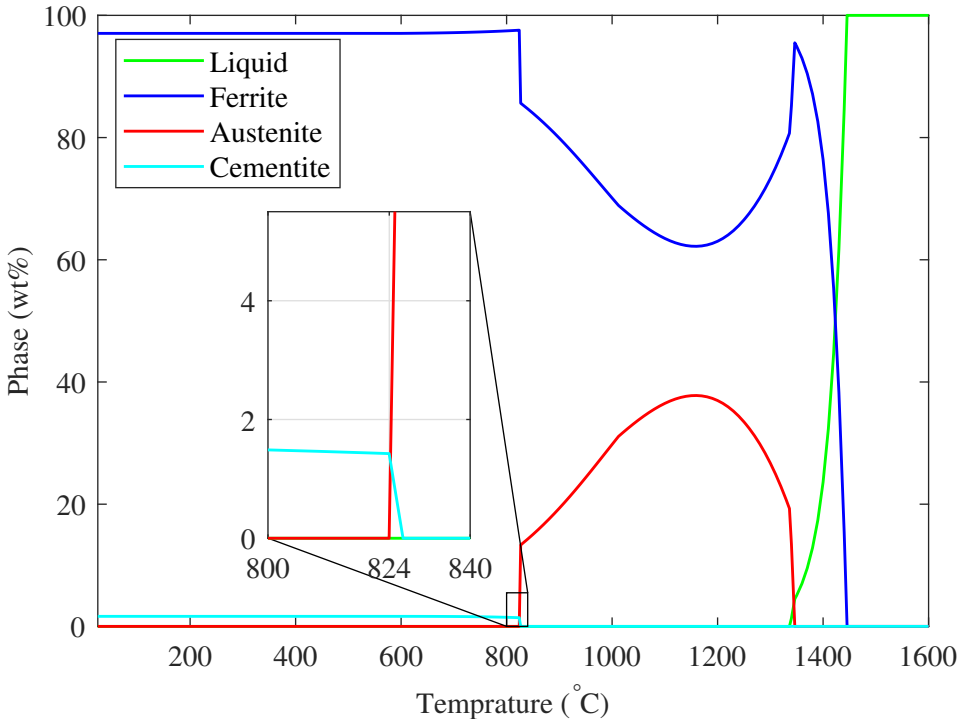

FIGURE 5.1: Variation of matrix phases in wt% with temperature

Once the microstructure of the cast iron has been settled, JmatPro can provide reliable estimations of physical and mechanical parameters at different temperatures such as: elastic

constants and physical properties that will be discussed in the following.

Regarding to the Table 5.1 matrix can be classified under ferritic steel alloys. It is well measured experimentally that the Coefficient of thermal expansion (CTE) dependens on the ambient temperature for the steel alloys (Hull et al., 1987). JMatPro results suggest that the CTE of the matrix is $13.6 \times 10^{-6}\,°C^{-1}$ at room temperature which is in agreement with a steel alloy of similar composition (ASTM, 1994). As the temperature increases, the matrix CTE increases linearly to reach the value of $17.15 \times 10^{-6}\,°C^{-1}$ at 824°C. This evolution with lattice thermal expansion is similar to that considered by Andriollo et al. for DCI Zhang (Andriollo et al., 2016). The variation of CTE and density as a function of temperature is shown in Fig. 5.2a and Fig. 5.2b, respectively.

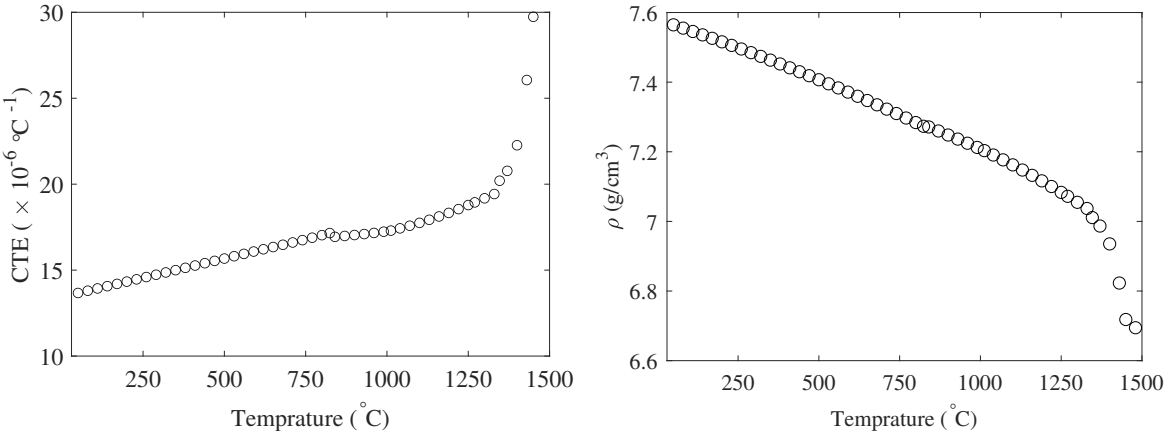

(a) CTE (b) Density

FIGURE 5.2: Variation of some matrix physical properties with tempratute

The matrix is expected to have improved mechanical properties compared to DCI due to the omission of the softest phase (graphite nodule). The JMatPro results show that at room temperature, the Young's modulus and Poisson's ratio of the matrix are 191.5 GPa and 0.29, respectively. Also, variation of elastic properties of the matrix with temperature follows a similar behavior for low carbon steels (Fukuhara and Sanpei, 1993). The variation of matrix elastic properties with temperature is illustrated in Fig. 5.3. The Young's modulus of the matrix decreases significantly at elevated temperature, as can be seen in Fig. 5.3a. As Fig. 5.3b indicates, Poisson's ratio of the matrix exhibits a slight linear increase as the temperature of the alloy increases.

To investigate the thermomechanical response of the matrix, a temperature dependent constitutive model is presented based on its chemical composition, microstructure and experimental observations. Usually von Mises criterion is used to define the yield surface of steel alloys. The strain hardening effect at room temperature can be characterized by a two-term Voce-type formulation. It is assumed that the matrix yield strength decreases linearly with increasing temperature and for above T_L (lower eutectoid temperature for DCI) loses its load carrying capability. So, the following relationship for the plastic flow curve of the matrix can be proposed:

$$\bar{\sigma} = [\sigma_0 + B_1(1 + e^{-C_1\bar{\varepsilon}_p}) + B_2(1 + e^{-C_2\bar{\varepsilon}_p})](1 - \frac{T - T_r}{T_L - T_r}) \tag{5.1}$$

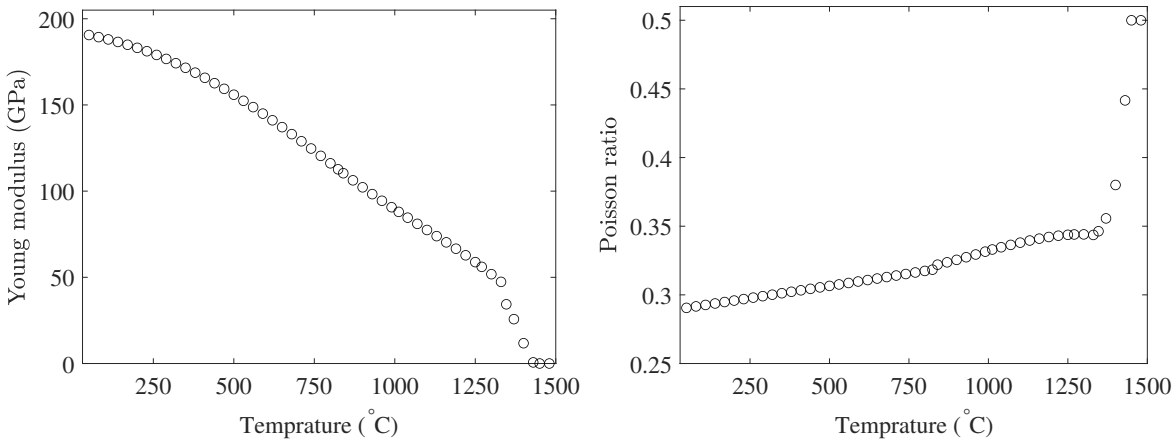

(a) Young's modulus (b) Poisson's ratio

FIGURE 5.3: Variation of some matrix elastic properties with temperature

where σ_0 is initial yield strength and B_1, C_1, B_2 and C_2 are material constants. In addition, T_r represents the ambient temperature which is assumed to be 25°C.

The plastic flow curve of the matrix at different temperatures using Eq. 5.1 is plotted in Fig. 5.4a. A conventional yield strength, $\sigma_{p0.2}$ can be measured at very low plastic strain of $\varepsilon_p = 0.2\%$. Hug et al. experimentally measured the $\sigma_{p0.2}$ for nodular cast iron whose chemical composition is close to the under study DCI (Hug et al., 2009). Fig. 5.4b shows the comparison between their experimental results and conventional yield strength of the matrix. Due to the fact that strength of DCI is governed by the matrix, the assumed evolution of the strength with temperature is applicable.

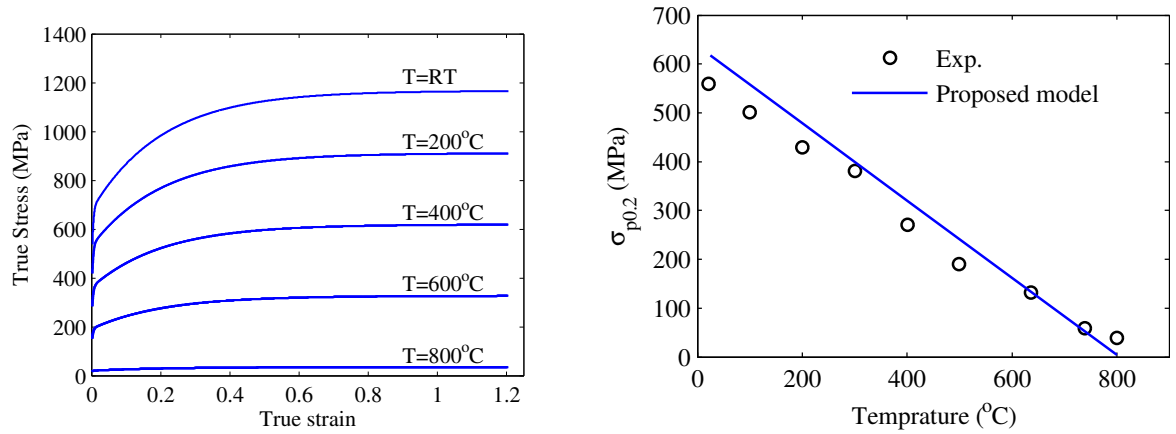

(a) True stress-strain curve for the matrix (b) Conventional yield strength

FIGURE 5.4: Variation of matrix strength with temperature

5.2.2 Nodule

It was discussed in sections 4.3 that the nodules are made of graphite and their material and microstructures do not vary noticeably in the different DCI materials. Therefore, the Young's modulus, Poisson's ratio and CTE of nodules are assumed to be identical to the values presented previously in the sections 4.3.

When the elastic properties of matrix and nodules are available, DigiMat package with the mean field approach can be used to calculate the elastic constants of the DCI. The results propose 167.5GPa and 0.28 for Young's modulus and Poisson's ratio of DCI respectively. These values are very close to the selected elastic properties of the DCI Hervas in sections 2.2.2. Therefore, as for the Zhang DCI, consideration of the assumed elastic properties of the nodule as well as the values calculated by JMatPro for the matrix, present acceptable results also for the DCI Hervas.

Preliminary simulations reveal that the nodule response indicates a slight dependence of the yield evolution with hydrostatic stress. Therefore, a non-associated Drucker-Prager pressure dependent material model in the form of Eqs. 2.1 and 2.2 is adopted for describing its yield. The functionality of this material model to predict the nodule behavior will be validated later.

5.3 Finite element analysis

The numerical results are obtained by the finite element software package MSC.MAR using the updated Lagrangian approach. This approach not only provides the required variables in the current configuration, but also gives an acceptable solution even under large deformations. The material models for the nodule and matrix are implemented using the user material subroutine *HYPELA2* while the mapping algorithm and stress updating procedure are adopted from the procedure proposed by De Suoza Neto et al. (De Souza Neto, Perić, and Owen, 2008). The interface between the nodule and the matrix is modeled by a contact surface and the contact parameters are assumed to be the same as those in section 4.4.1. For the post-processing, a python script is written to compute the homogenized stress field of the nodule, matrix and RVE as well as aspect ratio of the nodule at each increment. The numerical study consists of two steps: *cooling* and *Mechanical loading*.

5.3.1 Cooling

In this step, the DCI manufacturing process is simulated to introduce residual stress inside the RVE. The cooling process starts at 824°C as discussed in section 5.2.1. This temperature is introduced as the initial thermal condition to all nodes of the RVE mesh. At this temperature, the diameter and volume fraction of the nodules must be 17 µm and 8.84% respectively to achieve the desired dimensions at room temperature. Residual stress formation is simulated by uniformly reducing the temperature of the nodes from the initial condition to the room temperature. All the simulation characteristics of this step are considered to be the same as those of section 4.4.1, but the creep effect is neglected. Here, the goal is to investigate RVE response under noticeable deformation. Therefore, as concluded in section 4.5, this simplification has negligible impact on the RVE response while saving a lot of optimization time.

5.3.2 Mechanical loading

In this step, mechanical behavior of the RVE and the nodule under different loading conditions is studied. This step is carried out at room temperature and starts after completing the cooling step. Therefore, at the beginning of this step, the RVE contains residual stresses. Two sets of boundary conditions are involved: a fixed origin of the RVE and displacements of the reference points. The former is considered to avoid unwanted movement of the rigid body and the latter to impose a mechanical load on the RVE. The selected loading conditions include:

- Uniaxial tension
- Different compression conditions

A uniaxial tensile condition is imposed on the RVE according to the descriptions in section 3.2. For the compressive condition, the RP displacements are calculated based on the local deformation gradient in macroscale (which was obtained previously in section 2.4). How to calculate the RP displacement from the deformation gradient was explained in detail in section 3.2.

5.3.3 Material constants identification

An optimization procedure is adopted to identify the material constants of the matrix and nodule. The flow chart of the optimization procedure is depicted in the Fig. 5.5. In the error calculation step, the response of the RVE is compared to the following objectives:

- Uniaxial tensile test data of DCI Hervas (Hervas, Bettaieb, and Hug, 2013)
- Stress state at selected locations of the cylinder under compression (section 2.4)

The behavior of the RVE should be representative of homogenized macro medium. It was explained in section 3.2 the application of a periodic boundary condition for the RVE leads to the same strain field at the microscale. Consequently, RVE stresses should be in agreement with the local stress state of the macroscopic material. Apparently, for a given strain, the RVE stress is determined by the mechanical properties and the interaction between the matrix and the nodule. Therefore, for the above-mentioned objectives, the focus is on calibrating the mechanical properties of the RVE constituents to achieve a close agreement between the RVE stress field and the objectives. In the following, the process of constant identification of RVE constituents is presented:

- Matrix

It was mentioned earlier in section 5.2.1 that the matrix is a type of ferritic steel alloy, while mechanical behavior of steel alloys has been well investigated by the researchers. The strategy chosen to calculate the material constants of Eq. 5.1 is: first, theses constants should not be far from the DCI constants, keeping in mind that the matrix has more strength; and second, under the uniaxial tensile conditions, flow curve of the RVE is mainly governed by the matrix due to the trivial deformation of the nodule. The latter assumption will be discussed in section 5.4 based on the simulation results. Therefore, as a first step, material

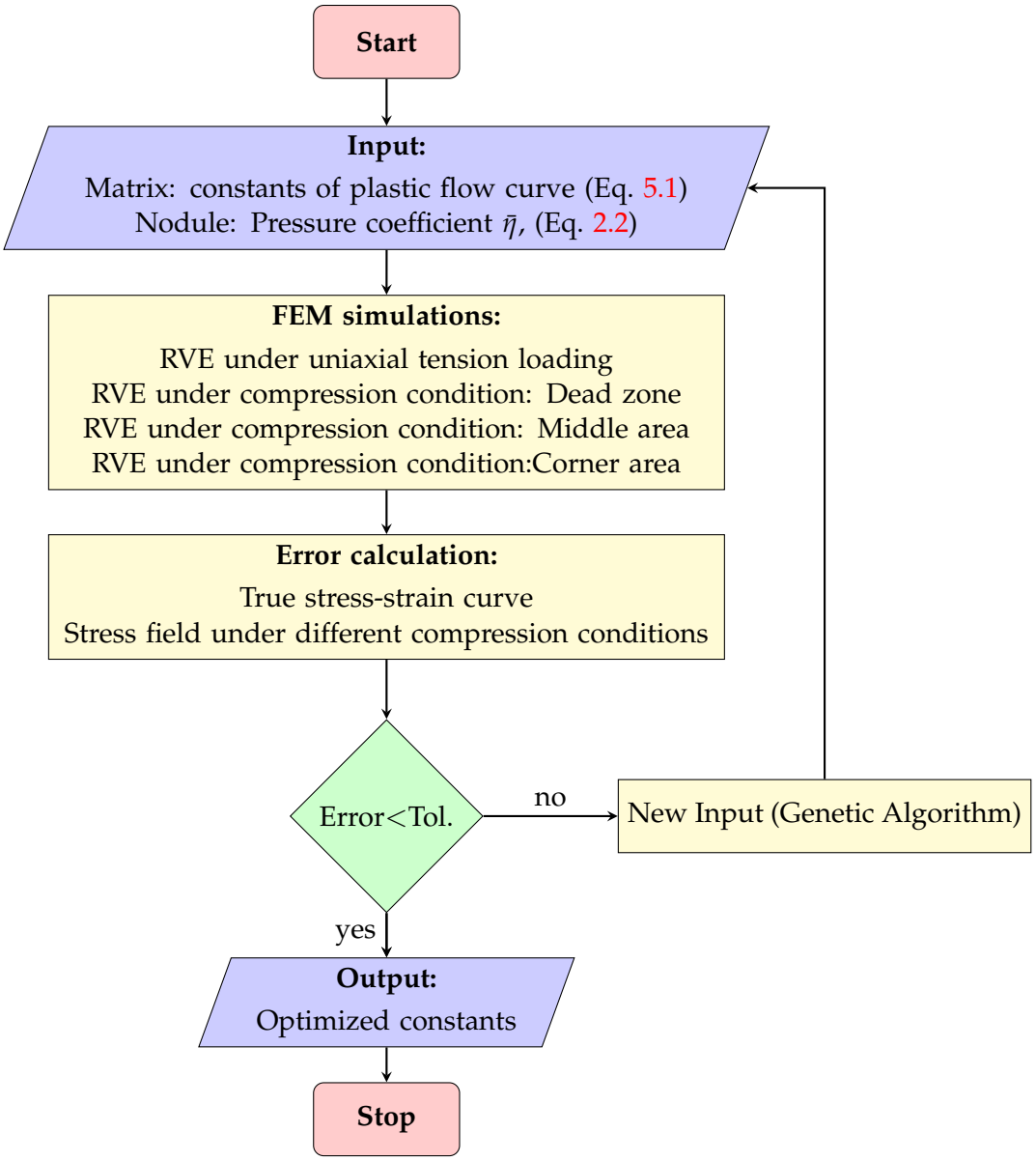

FIGURE 5.5: Flowchart of optimization procedure used for identification of RVE materials constants

constants of the matrix are calculated by comparing the stress-strain curves of DCI and RVE under uniaxial tensile conditions assuming that the nodule is elastic. The obtained constants of the matrix will be considered as an initial guess in the optimization process.

- Nodule

In section 1.2.4, it was stated that the behavior of the nodule under large strain deformations is still a challenge. Among all the unknowns of the nodule, its yield and stress-strain relationship are placed on the dark side. Here, inspired by previous research on the graphite, an attempt will be made to shed some light on the problem.

Compressive failure experiments have been performed under different confining pressure conditions for graphite material by Yi et al. (Yi et al., 2020). They studied different yield criteria as well as Mohr-Coulomb with the following relationship:

$$\sigma_1 = \frac{1+\sin\phi}{1-\sin\phi}\sigma_3 + \frac{2c.\cos\phi}{1-\sin(\phi)} \tag{5.2}$$

where σ_1 is axial stress, σ_3 is the confining pressure, c is the cohesion and ϕ is the frictional angle. The material constants c and ϕ are reported 29.6 MPa and 10.6° respectively.
One of the most common approximations for the Drucker-Prager criterion is that its yield surface coincides with the outer edges of the Mohr-Coulomb surface. This coincidence is obtained when η and $\bar{\sigma}$ in the Eq. 2.1 are:

$$\eta = \frac{6\sin\phi}{\sqrt{3}(3-\sin\phi)}, \quad \bar{\sigma} = \frac{6c.\cos\phi}{(3-\sin\phi)} \tag{5.3}$$

By inserting the reported values for cohesion and frictional angle into Eq. 5.3, η and $\bar{\sigma}$ are calculated 0.2263 and 61.9 MPa respectively. These values are considered as meaningful constants for describing nodule yield. Since no strain hardening is reported for the graphite material, $\bar{\sigma}$ of the nodule is assumed to be constant.

Graphite is a quasi-brittle material and its mechanical behavior under confining pressure can be assimilated to that of rock materials (Yi et al., 2020). The mechanical behavior of rock materials changes from brittle failure under low confining pressure to compressional-shear and plastic failure with noticeable volume expansion under high confining pressure (You, 2010; Tarasov and Potvin, 2013). These findings are consistent with experimental observations for the graphite nodule under confining pressure where formation of cracks into the nodule is reported (Hervas et al., 2013). Therefore, it can be concluded that the volume increase occurs after the nodule rupture under confining pressure and therefore, $\bar{\eta}$ in eqn 2.2 is not zero. However, if the associated flow rule is assumed ($\eta = \bar{\eta}$), the significant volume expansion may lead to an unrealistic pressure of the RVE. In this case, the evolution of the RVE pressure is influenced by the amount of nodule volume expansion. Therefore, $\bar{\eta}$ can be specified by optimizing the RVE pressure.

The code used for the optimization and its characteristics are the same as the procedure presented in section 2.2.4. The constants of RVE constituents are calculated to obtain acceptable results for both objectives. Finally, all the constitutive material constants of the matrix and nodule are summarized and reported in Table 5.3. The functionality of these proposed values will be discussed in detail later.

TABLE 5.3: RVE constitutive constants at room temperature

Elastic parameters			Yield criterion $\Phi = \sqrt{J_2} + \eta\sigma_h - \frac{\bar{\sigma}}{\sqrt{3}}$ $\Psi = \sqrt{J_2} + \bar{\eta}\sigma_h - \frac{\bar{\sigma}}{\sqrt{3}}$ $\bar{\sigma} = \sigma_0 + B_1(1 + e^{-C_1\bar{\varepsilon}_p}) + B_2(1 + e^{-C_2\bar{\varepsilon}_p})$						
	E (GPa)	ν	η	$\bar{\eta}$	σ_0 (MPa)	B_1 (MPa)	C_1	B_2 (MPa)	C_2
Nodule	37.5	0.163	0.2263	0.022	61.9	0	0	0	0
Matrix	191.53	0.29	0	0	537	150	350	480	4.9

5.4 Results and discussion

In this section, the results of the presented RVE model under different mechanical loadings are presented. During the deformation of the RVE, volumetric strains cause volume change due to hydrostatic stresses while deviatoric stresses are responsible for possible distortion. Therefore, it can be concluded that the hydrostatic and deviatoric stresses of the RVE can reveal its overall mechanical behavior. Therefore, $\bar{\sigma}_h$ and $\bar{\sigma}_{eds}$ are used as representative quantities to describe the stress of the RVE in complex stress states. In all the plots related to the RVE stress contour, some blocks of the RVE mesh are removed for better presentation.

5.4.1 Uniaxial tension

Numerical calculations confirm that under uniaxial tensile conditions, the RVE stress component along tension direction is equal to the RVE effective deviatoric stress. Fig. 5.6 shows RVE true stress-strain tensile response where admirable concordance with the experimental data reported by Hervas et al. (Hervas, Bettaieb, and Hug, 2013) has been achieved.

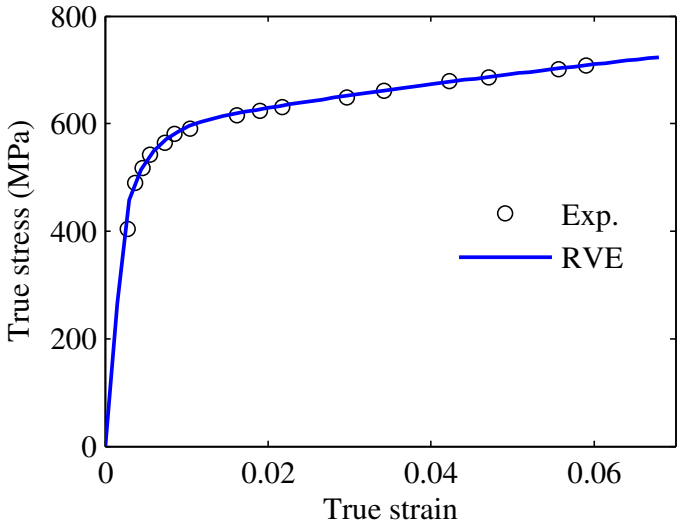

FIGURE 5.6: Uniaxial tensile stress-strain curve of RVE

The distribution of the RVE effective deviatoric stress at the end of the tension is plotted in Fig. 5.7a. The results show that the nodule stress values are trivial with respect to matrix. This may be due to the separation between the nodule and the matrix along tension direction that has been observed in tests (Hervas, Bettaieb, and Hug, 2013) which also can be seen in Fig. 5.7b where contact surface is shown by red color. Therefore, it is confirmed that the tensile stress response of the RVE is mainly driven by the matrix behavior and the assumptions that were considered in the matrix constant identification part of section 5.3.3 and also calculated values for the matrix material model are acceptable.

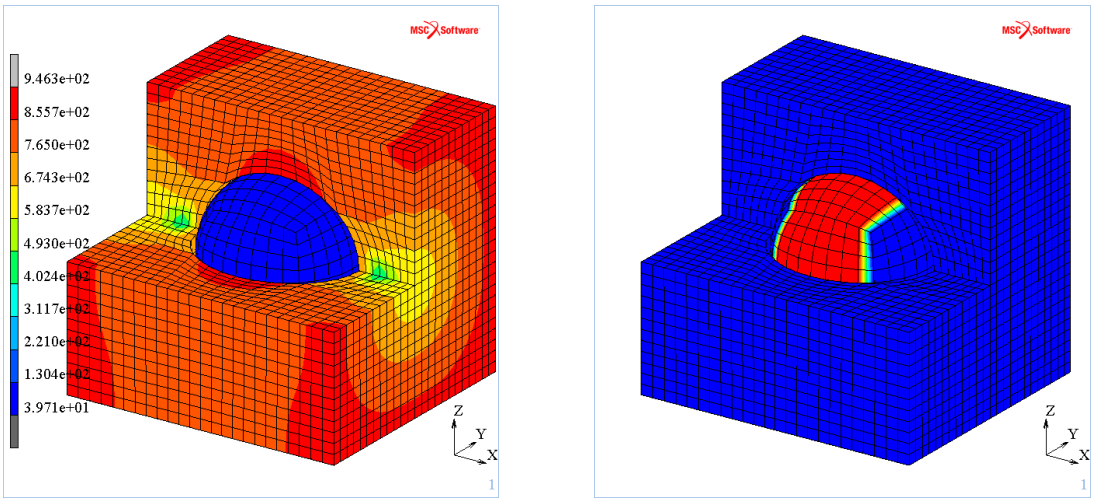

(a) Effective deviatoric stress (b) Contact status

FIGURE 5.7: RVE at the end of uniaxial tension

5.4.2 Compression condition: Dead zone

Trivial plastic strain makes this point an ideal location for studying elastic properties of the RVE and specially the nodule. Comparison between stress results in macro and micro scales is presented in Fig. 5.8. Distribution of pressure and effective deviatoric stress of the RVE at equivalent plastic strain equal to 0.00134 are shown in Fig. 5.9.

In the Fig. 5.8a a good agreement between the hydrostatic stresses at the macro and microscopic scales can be observed. As suggested by Fig. 5.9a, the nodule sustains pressure more than matrix. The minimum pressure of the RVE is found at top and bottom of the nodule in the direction of compression (z axis), while the center of the nodule experiences notable pressure. During the optimization process, it was found that the RVE pressure is governed by the elastic constants of the nodule; increasing the Young's modulus and Poisson's ratio of the nodule leads to an increase in the RVE pressure. Therefore, it can be concluded that the proposed Young's modulus and Poisson's ratio of the nodule are capable of describing the RVE pressure at low deformation under complex compression condition.

It can be seen in Fig. 5.8b that the effective deviatoric stress of the RVE gives acceptable conformity with the macro results. Fig. 5.9b shows that the matrix posses a high and almost uniform effective deviatoric stress, except for two narrow regions in the direction of compression and near the nodule. Thus, as under uniaxial tensile conditions, the effective deviatoric stress of the RVE is mainly governed by the matrix. Also, this figure indicates

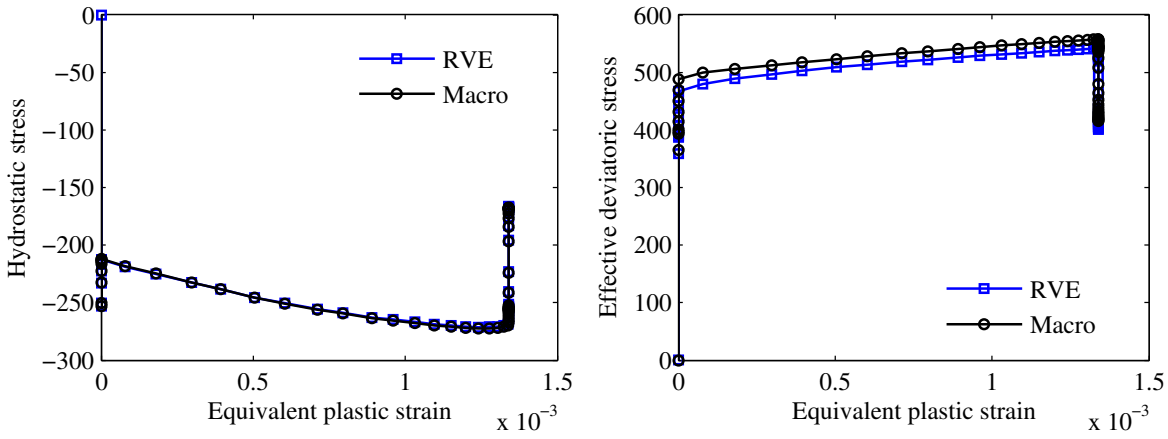

(a) Hydrostatic stress (mean stress) (b) Effective deviatoric stress

FIGURE 5.8: RVE stress results for Dead zone in the compression sample

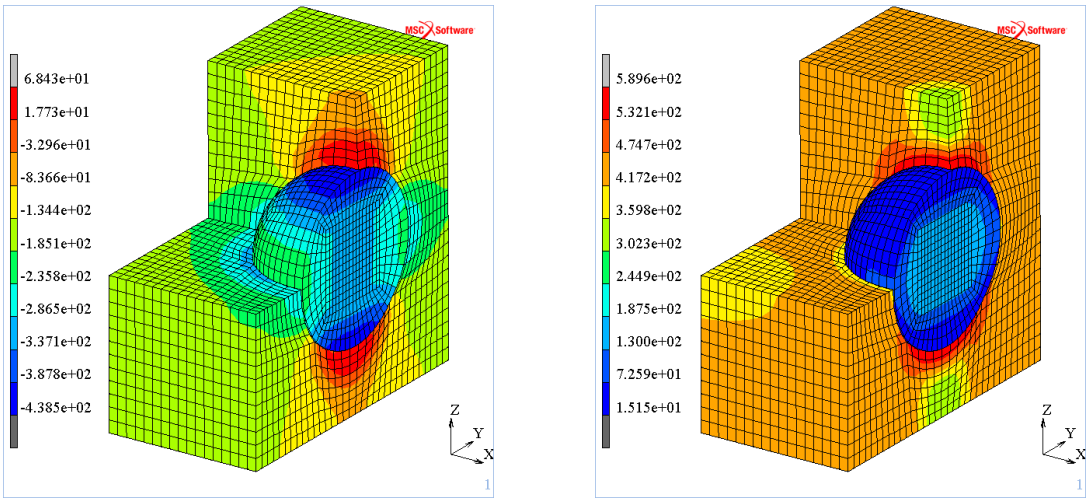

(a) Hydrostatic stress (mean stress) (b) Effective deviatoric stress

FIGURE 5.9: RVE stress distribution at EQPLAS=0.00134 for Dead zone in the compression sample

that the effective deviatoric stress is unremarkable at the outer surface of the nodule and gradually increases to reach its maximum at the center. Therefore, it can be predicted that the center of the nodule undergoes irreversible deformation prior to other parts during compression. Satisfactory results confirm the validity of the assumed material constants as well as nodule elastic properties.

5.4.3 Compression condition: Middle area

This point experiences huge plastic deformation with low amount of shear strain. Therefore, this point is suitable for studying the behavior of the nodule under large strains and characterizing its parameters.

The stress results of the RVE are presented in Fig. 5.10. The RVE hydrostatic stress shows acceptable agreement with the microscale data as seen in Fig. 5.10a. The RVE pressure is consistent with the objective from small deformations to large plastic strains. Although unconvincing results for equivalent plastic strain greater than 1.1 are not avoidable due to the extreme distortion of the elements and the resulting numerical errors. During the optimization, numerical results reveal that the RVE pressure in small deformations depends mainly on the elastic constants of the nodule, while for large deformations it depends mainly on the strength behavior of the nodule. In small strains, increasing the Young's modulus and Poisson's ratio of the nodule and in large strains, increasing $\bar{\eta}$ will increase the absolute values of the RVE pressure. Therefore, it can be concluded that the mentioned nodule constants are reasonably chosen. Fig. 5.10b shows the effective deviatoric stress of the RVE where conformity with the local macro stress is obtained. The results indicate that the effective deviatoric stress of RVE is dominantly controlled by the matrix strength evolution curve. As a matter of fact, due to the low yield strength of the nodule, its effect on the effective deviatoric stress of the RVE is not primary. Therefore, it can be concluded that the proposed stress-strain equation for the matrix is acceptable.

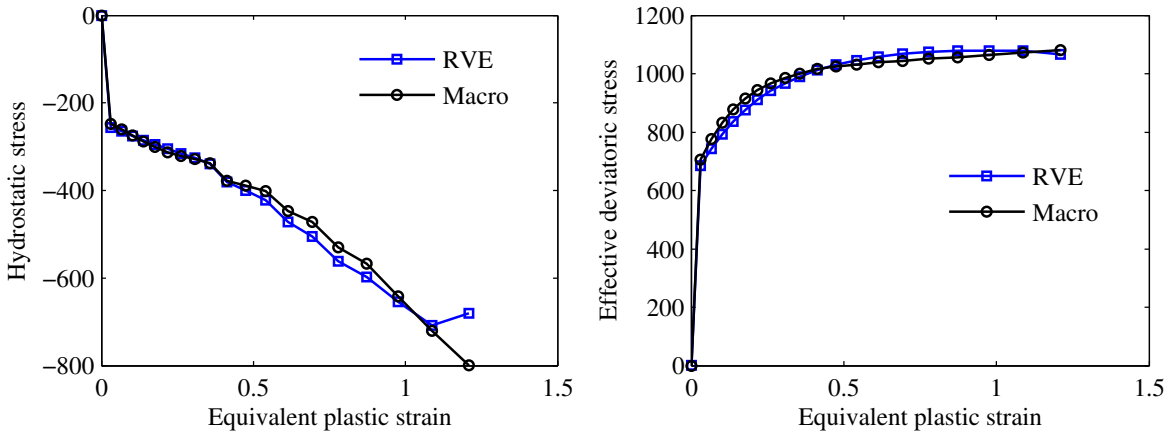

(a) Hydrostatic stress (mean stress)

(b) Effective deviatoric stress

FIGURE 5.10: RVE stress results for Middle area in the compression sample

Nodule deformation and distribution of RVE equivalent plastic strain during compression is depicted in Fig. 5.11. Maximum equivalent plastic strain occurs in the centeral area of the nodule for low levels of compression where outer regions along the direction of compression being subjected to smaller deformations than the other parts (Fig. 5.11a). As compression continues, the nodule loses its spherical shape and becomes more oval. This also happens for the region with maximum equivalent plastic strain inside the nodule, as seen in Figs. 5.11b, 5.11c and 5.11d. For the $\Delta L/L_0$ greater than 0.35, the nodule begins to deform as *UFO* due to excessive deformation of the transverse planes (respect to the direction of compression). It can be seen in the Fig. 5.11e that regions with maximum equivalent plastic strain move towards the edge of the nodule. This phenomenon continues as compression continues and creates a deformed UFO-shape nodule with sharp edge as shown in Fig. 5.11f. It should be noted that due to the huge distortion of the elements, especially at the edge of the nodule at high strains, some unrealistic local data are not preventable and the RVE can not sustain a deformation greater than $\Delta L/L_0 = 0.485$.

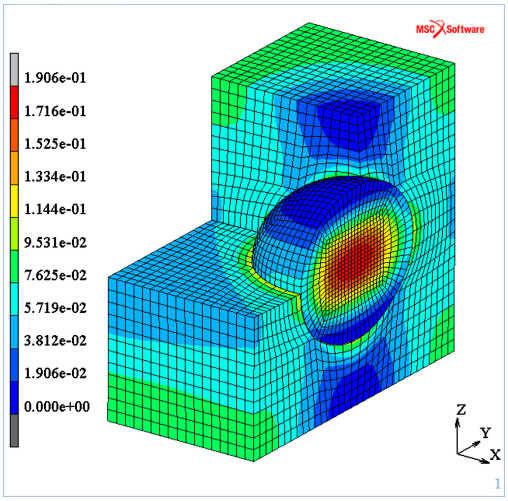

(a) $\Delta L/L_0 = 0.05$

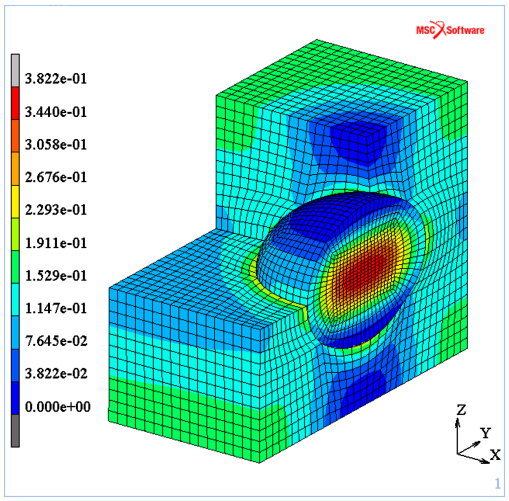

(b) $\Delta L/L_0 = 0.1$

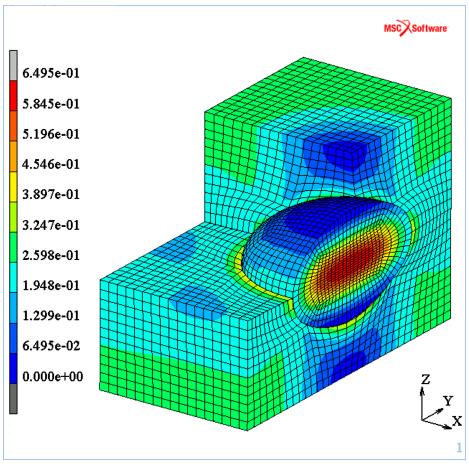

(c) $\Delta L/L_0 = 0.17$

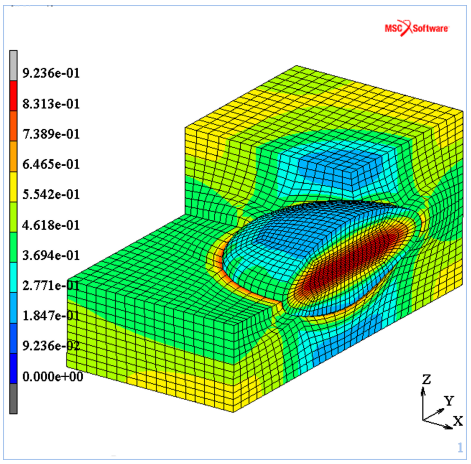

(d) $\Delta L/L_0 = 0.28$

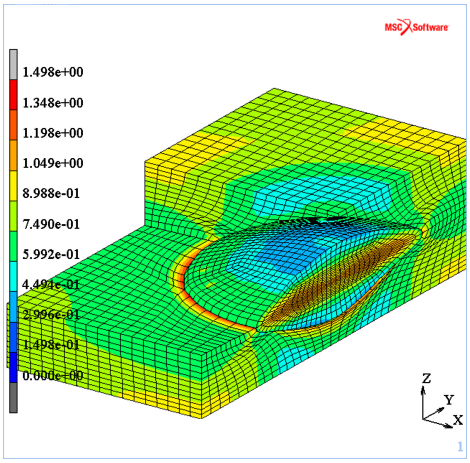

(e) $\Delta L/L_0 = 0.38$

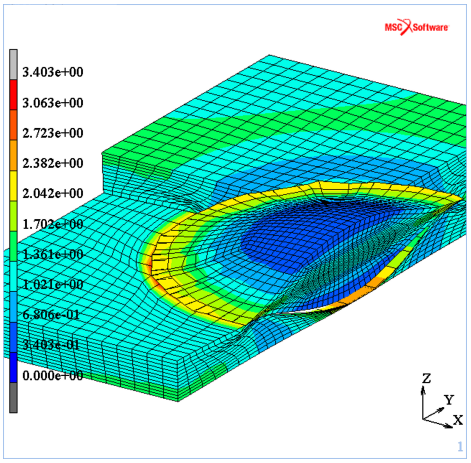

(f) $\Delta L/L_0 = 0.485$

FIGURE 5.11: Nodule deformation and RVE equivalent plastic strain contour during compression of Middle area

5.4.4 Compression condition: Corner area

This location experiences large deformation accompanied by noticeable shear strain. Therefore, the behavior of RVE and the characteristics of nodules can be investigated under huge distortion. Because of the excessive distortion of some elements, the maximum level of compression achievable in simulations is $\Delta L/L_0 = 0.415$.

The RVE stresses are plotted in Fig. 5.12. Despite a disagreement for an equivalent plastic strain greater than 0.6, the hydrostatic part of the RVE stress coincides in a satisfactory manner with microscale results as shown in Fig. 5.12a. The numerical results again confirm the findings that were discussed in section 5.4.3. The RVE effective deviatoric stress is compared to the microscale data in Fig. 5.12b. The harmony between the results indicates that the calibrated RVE can simulate the DCI response in the presence of compressive and huge shear deformation. Therefore, the proposed elastic constants and strength model for the nodule can describe its characteristics.

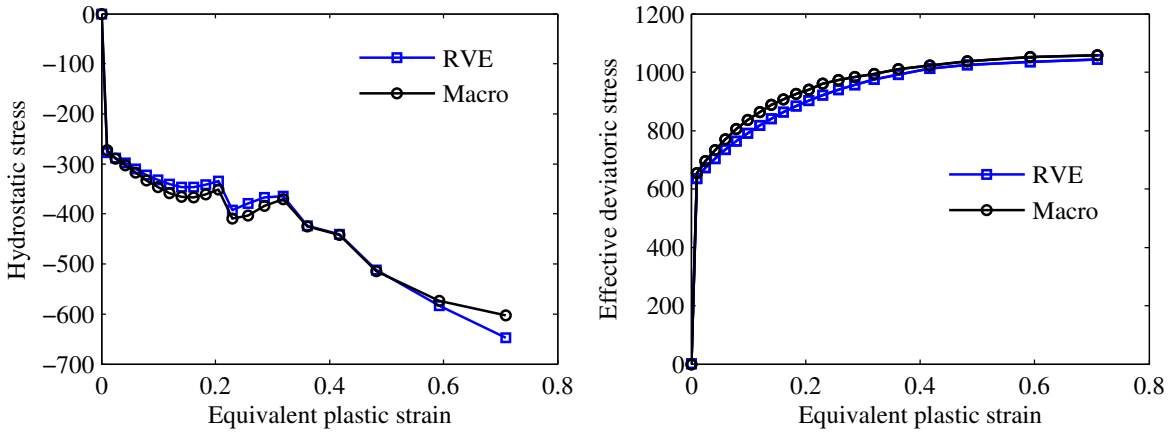

(a) Hydrostatic stress (mean stress)

(b) Effective deviatoric stress

FIGURE 5.12: RVE stress results for Corner in the compression sample

RVE configuration and distribution of the equivalent plastic strain in different levels of the compression is depicted in Fig. 5.13.

From Figs. 5.13a, 5.13b, 5.13c, and 5.13d for the compression levels up to $\Delta L/L_0 = 0.28$ middle area of the nodule has maximum deformation while the nodule loses its spherical shape and becomes more and more oval. For compression levels higher than $\Delta L/L_0 = 0.38$, the nodule starts to distort due to shear deformation of the RVE where, in some regions of the matrix, amount of equivalent plastic strains is greater than nodule's middle area as can be seen in Figs. 5.13a and 5.13b.

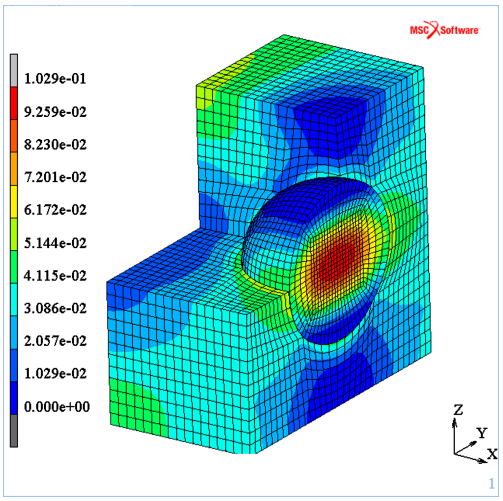

(a) $\Delta L/L_0 = 0.05$

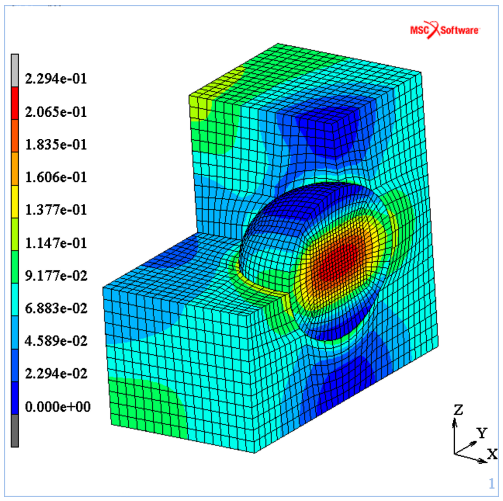

(b) $\Delta L/L_0 = 0.1$

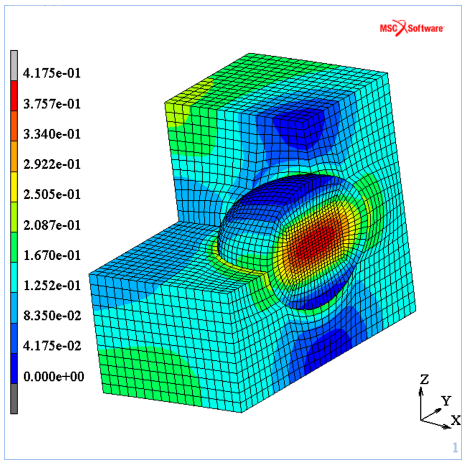

(c) $\Delta L/L_0 = 0.17$

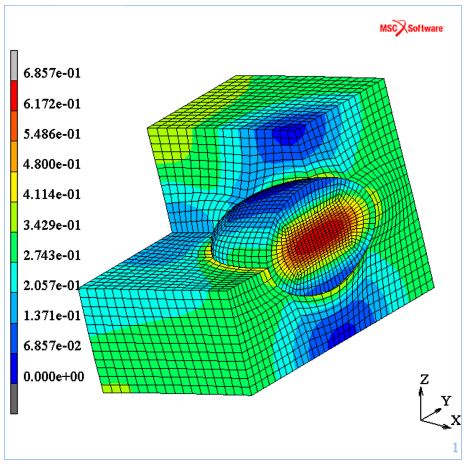

(d) $\Delta L/L_0 = 0.28$

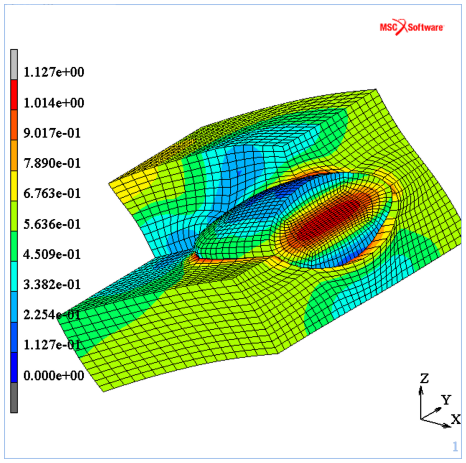

(e) $\Delta L/L_0 = 0.38$

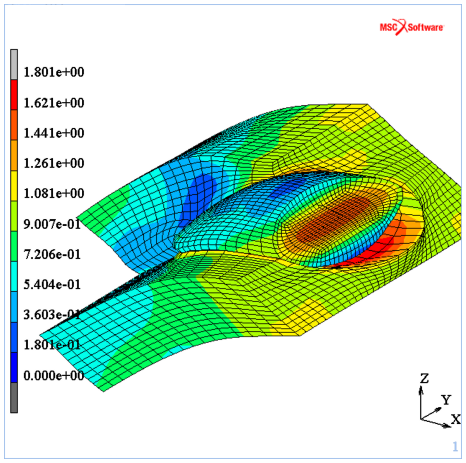

(f) $\Delta L/L_0 = 0.415$

FIGURE 5.13: Nodule deformation and RVE equivalent plastic strain contour during compression of Corner area

5.5 Nodule morphology

Investigating nodule deformation during compression is studied in this section. If the RVE is properly calibrated, the nodule morphology will be consistent with experimental observations. At the microscale, the nodule deformation can be considered as an indicator of the local strains state of macro medium since it is coupled to the global deformation of the DCI (Hervas et al., 2013). Therefore, if the nodule deformation is described correctly, it can be supposed that the nodule constitutive constants are selected reasonably and that the strain distribution throughout the RVE is reliable.

Fig. 5.14a shows the configuration of the RVE in Middle area and at the end of the numerical simulation where its initial configuration is plotted in pink. The shape of the nodule is compared to the experimental observation in Fig. 5.14b.

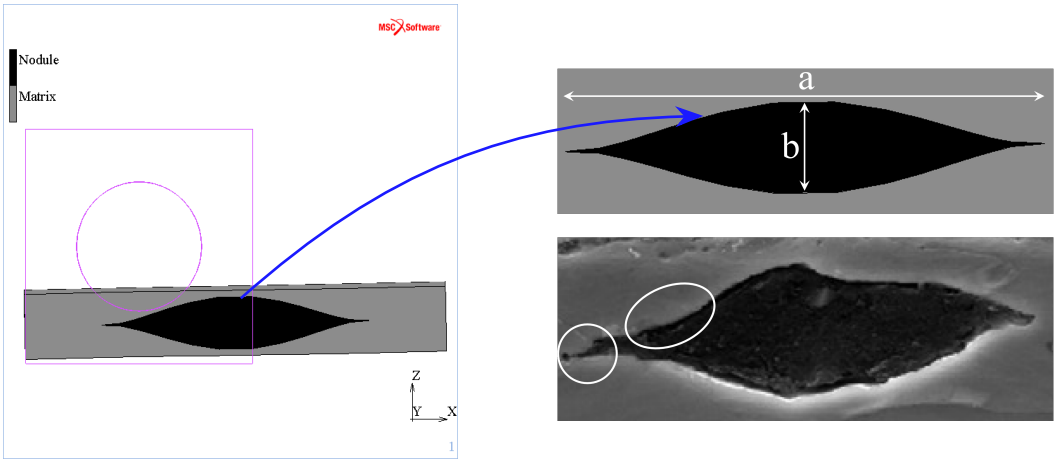

(a) RVE (b) Hervas et al., 2013

FIGURE 5.14: Nodule deformed shape at Middle area

As figure suggests, nodule UFO-shape is close to the experiments. The sharp edge of the deformed nodule (circle) and the indent part between center and the edge (ellipsoid) are also visible in the test. Also, figure indicates that no separation is occurred between the nodule and the matrix interface, which is consistent with experiments. This indicates that the penetration of the nodule edges into the surrounding matrix, due to its lower hardening, is greater than or at least equal to the matrix tearing due to the geometry of deformation.

The final shape of the RVE imposed on the deformation condition of the Corner area is plotted in Fig. 5.15a where its initial configuration is depicted by the color pink. The shape of the deformed nodule is compared to the experimental monitoring in Fig. 5.15b. Despite the premature termination of the numerical analysis due to the distortion of the elements, it can be seen that the shape of the nodule is comparable to the experiment.

The qualitative study through Figs. 5.14 and 5.15 verifies that the nodule shape at different locations in the compression sample is similar to the test.

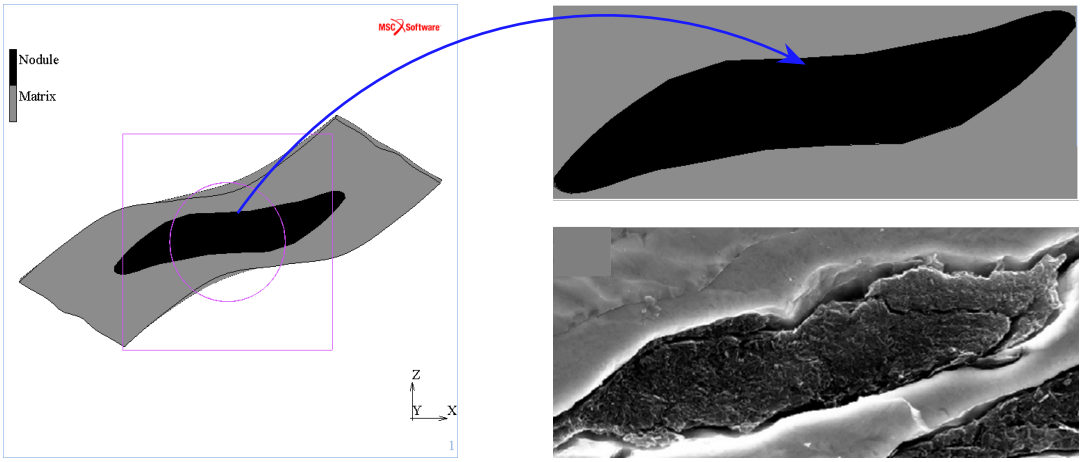

(a) RVE (b) Hervas et al., 2013

FIGURE 5.15: Nodule deformed shape at Corner area

For the quantitative study of nodule morphology, the variation in nodule aspect ratio for two locations in the Middle and Corner areas of the compression sample is shown in Fig. 5.16.

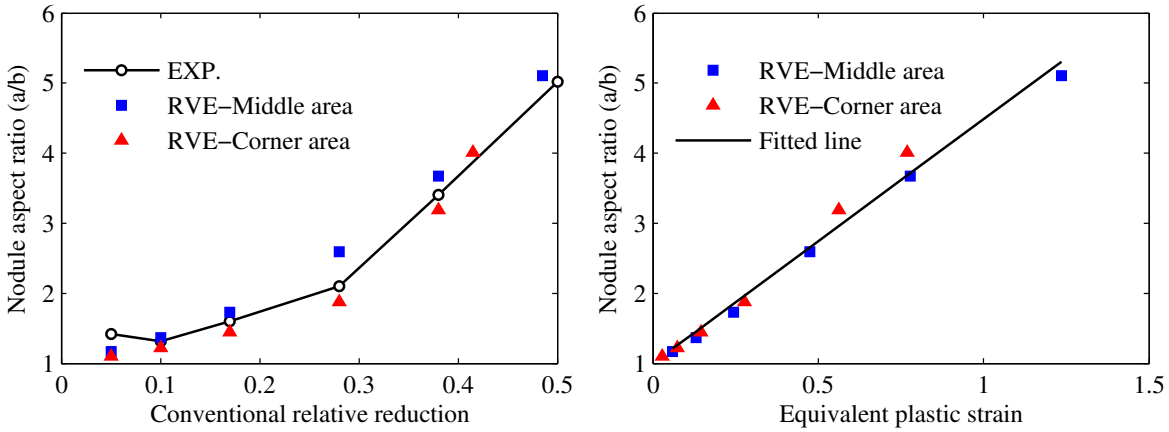

(a) Variation with sample height reduction (b) Variation with local deformation

FIGURE 5.16: Variation of nodule aspect ratio under compression

The nodule aspect ratio is defined by $AR = a/b$ where a and b are the major and minor diameters, respectively as depicted in Fig. 5.14b. Experimental measurements show that nodule aspect ratio is similar for these two locations (Hervas et al., 2013). Fig. 5.16a presents convincing agreement between numerical and experimental results which confirms that the RVE model describes nodule deformation appropriately.

The variation of the nodule aspect ratio with equivalent plastic strain is shown in Fig. 5.16b where the figure suggests a linear relationship between these parameters:

$$AR = 3.486\,\bar{\varepsilon}_p + AR_0 \tag{5.4}$$

where AR_0 is the initial nodule aspect ratio which is unit for spherical nodule.

Based on the Eq. 5.4, amount of nodule deformation is related to the local strain field in microscale. Therefore, the nodule aspect ratio can be directly estimated from the amount of equivalent plastic strain in macro homogeneous medium. Hervas et al. showed that the variation of nodule aspect ratio with strain is independent of the sample geometry (height to diameter ratio of the cylindrical sample) or the measurement location (Hervas et al., 2013). So, Eq. 5.4 can be used to calculate the local nodule aspect ratio in general DCI compression.

Chapter 6

Conclusion

In this thesis, a multiscale numerical study on the different DCIs has been performed to investigate the mechanical properties of these materials and their constituents, matrix and nodule.

6.1 Summary of results

The finite element simulation results showed that DCI is a pressure dependent material. Since no volume increase during cylinder compression was observed in the experiments, a completely unassosciated flow rule can accurately produce its behavior under positive stress triaxiality, such as the uniaxial tensile test, or under negative stress triaxiality, such as cylinder compression. The material constants were obtained by the inverse calibration method and by using a multiplicative formulation in the numerical calculations. The calibrated FE model gave satisfactory agreement with the experimental measurements. It can be concluded that if macro-model is calibrated correctly, the numerical results will be consistent with the objectives and the optimized parameters will be acceptable or even realistic. Therefore, the local strain and stress state of the FE model were used to calibrate the mechanical properties of DCI constituents.

The micromechanical approach was used to analyze the local strain development into a ferritic DCI during solidification and predict the finale state of residual stresses. To make up for the lack of information on the physical–mechanical properties of the constituents, a critical aspect in using the approach, the literature data were supplemented with those derived by adopting the CALPHAD methodology. The method proved to be effective for the determination of thermodynamic and physical properties. As for mechanical properties, the approach is only viable for those of broad application interest for the type of metal alloy considered. The analyses carried out allowed to verify and quantify the effect that viscous creep, active at high temperatures, has on the final state of residual stresses, through relaxation. The results showed a dominant influence of primary creep over secondary creep. Comparison with experimental data demonstrated the need to consider viscous creep in modeling to correctly predict the distribution of residual stresses in the RVE.

To investigate nodule behavior under large deformations, RVE was calibrated to reproduce same properties of the DCI material. An alasto-plastic model was considered for the nodule while nodule strength follows a pressure dependent relationship. Micromechanical analysis results showed that assuming associated flow rule for nodule, results in excessive

pressure into the RVE. Multi objective optimization of material constants, suggested a non-asosciated flow rule with a little of volume increase for the nodule. Numerical resultes confirmed that nodule morphology in high compression levels is comparable with experimental observations. Also, in the compression test, nodule morphology depends on DCI local deformation and is a direct function of equiavalent plastic strain nevertheles of its location in the sample or geometry of the specimen.

This study was performed on two different DCI materials. Apparently, different sets of properties for their matrix materials were considered. Since no significant differences between the composition and microstructure of nodules in different grades of DCI were reported in the literature, only one set of physical and mechanical properties was proposed for the nodules. The results of this thesis confirmed the functionality of the properties presented for nodules.

6.2 Proposals for future developments

In this thesis, the constitutive models of DCI and its components were presented and their mechanical properties at room temperature were investigated. DCI is widely used for the construction of machine parts operating at high temperatures, and one of the topics of interest is the study of its thermomechanical properties at high temperatures. In this regard, knowledge of the behavior of DCI under cyclic thermomechanical loading can be studied. The constitutive models need to be extended to include the cyclic effect of loading and to study the response of the RVE during thermomechanical cycling. This requires to incorporate new features such as the kinematic hardening effect into the constitutive relationships.

Another topic that needs to be explored is the ductile damage of DCI. The integration of the presented constitutive models with Continuum Damage Mechanics (CDM) models can develop the knowledge of DCI failure by the micromechanical method. To this end, a coupled damage-plasticity model can be presented for the constitutive material models of the RVE constituents. If the RVE is calibrated to give acceptable calculations of microstructural damage, the failure behavior of DCI can be predicted even before fabrication.

Studying grain size effect on the DCI behavior is another interesting subject. Investigations show that if grain size is reduced sufficiently, the mechanical properties of the engineering materials improve significantly. Although research has been conducted on some metal forming methods, such as Equal Channel Angular Pressing (ECAP), to study the effect of finer grains on the DCI properties, these attempts have been focused on the macroscale behavior. Studying the mechanical properties of DCI in fine-grained processes using a micromechanical approach opens the door to revealing the effect of nodule shape and size on the final microstructure. In this case, the new microstructure of the fine-grained DCI and its mechanical properties can be predicted even before manufacturing.

Bibliography

American Foundrymen's Society (1993). *Ductile iron handbook.* Inc. Des Plaines, Illinois, p. 277. ISBN: 9780874331240.

Andriollo, Tito, Søren Fæster, and Grethe Winther (2018). "Probing the structure and mechanical properties of the graphite nodules in ductile cast irons via nano-indentation". In: *Mechanics of Materials* 122, pp. 85–95. ISSN: 01676636. DOI: 10.1016/j.mechmat.2018.03.010. URL: https://doi.org/10.1016/j.mechmat.2018.03.010.

Andriollo, Tito, Jesper Thorborg, and Jesper Hattel (2016). "Modeling the elastic behavior of ductile cast iron including anisotropy in the graphite nodules". In: *International Journal of Solids and Structures* 100-101, pp. 523–535. ISSN: 00207683. DOI: 10.1016/j.ijsolstr.2016.09.023. URL: http://dx.doi.org/10.1016/j.ijsolstr.2016.09.023.

Andriollo, Tito et al. (2016). "A micro-mechanical analysis of thermo-elastic properties and local residual stresses in ductile iron based on a new anisotropic model for the graphite nodules". In: *Modelling and Simulation in Materials Science and Engineering* 24.5, p. 55012. ISSN: 1361651X. DOI: 10.1088/0965-0393/24/5/055012. URL: http://dx.doi.org/10.1088/0965-0393/24/5/055012.

Andriollo, Tito et al. (2018). "Uncovering the local inelastic interactions during manufacture of ductile cast iron: How the substructure of the graphite particles can induce residual stress concentrations in the matrix". In: *Journal of the Mechanics and Physics of Solids* 111, pp. 333–357. ISSN: 00225096. DOI: 10.1016/j.jmps.2017.11.005.

Andriollo, Tito et al. (2019). "Impact of micro-scale residual stress on in-situ tensile testing of ductile cast iron: Digital volume correlation vs. model with fully resolved microstructure vs. periodic unit cell". In: *Journal of the Mechanics and Physics of Solids* 125, pp. 714–735. ISSN: 0022-5096. DOI: 10.1016/J.JMPS.2019.01.021.

ASTM (1994). *Standard Specification for Iron-Silicon Relay Steels*. Vol. i. Reapproved, pp. 1–2.

Barrett, C. R. and W. D. Nix (1965). "A model for steady state creep based on the motion of jogged screw dislocations". In: *Acta Metallurgica* 13.12, pp. 1247–1258. ISSN: 00016160. DOI: 10.1016/0001-6160(65)90034-9.

Barrett, Craig Radford (1964). "THE INFLUENCE OF GRAIN BOUNDARIES AND STACKING FAULTS ON HIGH TEMPERATURE PLASTIC DEFORMATION." Ph. D. Thesis. Stanford University. URL: https://apps.dtic.mil/sti/citations/AD0609250.

Bird, J., A. Mukherjee, and J. E. Dorn (1969). *CORRELATIONS BETWEEN HIGH-TEMPERATURE CREEP BEHAVIOR AND STRUCTURE.* Tech. rep. Berkeley, California: University of California, Lawrence Berkeley National Laboratory.

Bonora, Nicola and Andrew Ruggiero (2005). "Micromechanical modeling of ductile cast iron incorporating damage. Part I: Ferritic ductile cast iron". In: *International Journal of Solids and Structures* 42.5-6, pp. 1401–1424. ISSN: 00207683. DOI: 10.1016/j.ijsolstr.2004.07.025.

Brocks, W., S. Hao, and D. Steglich (1996). "Micromechanical modelling of the damage and toughness behaviour of nodular cast iron materials". In: *Journal De Physique. IV : JP* 6.6. ISSN: 11554339. DOI: 10.1051/jp4:1996605.

Cadek, J (1988). *Creep in Metallic Materials*. Vol. 48. Elsevier Science Publishers B.V. ISBN: 0444989161.

Collini, L. and G. Nicoletto (2005). "Determination of the relationship between microstructure and constitutive behaviour of nodular cast iron with a unit cell model". In: *Journal of Strain Analysis for Engineering Design* 40.2, pp. 107–116. ISSN: 03093247. DOI: 10.1243/030932405X7692.

Collini, L. and A. Pirondi (2020). "Micromechanical modeling of the effect of stress triaxiality on the strain to failure of ductile cast iron". In: *Engineering Fracture Mechanics* 238, p. 107270. ISSN: 00137944. DOI: 10.1016/j.engfracmech.2020.107270.

Colonna, F. et al. (2009). "Properties of graphite at melting from multilayer thermodynamic integration". In: *Physical Review B - Condensed Matter and Materials Physics* 80.13, pp. 1–8. ISSN: 1550235X. DOI: 10.1103/PhysRevB.80.134103.

Cottrell, Alan (1995). *An introduction to metallurgy*. London: The institute of materials, p. 548. ISBN: 9780901716934.

Davies, P. W. et al. (1973). "Stress-change experiments during high-temperature creep of copper, iron, and zInc." In: *Metal Science Journal* 7.1, pp. 87–92. ISSN: 00260681. DOI: 10.1179/030634573790445659.

Davies, R G (1963). "Steady-state creep in Fe-2 to 11 at. pct Si alloys". In: *Transactions of the Metallurgical Society of AIME* 227.3, p. 665.

De Souza Neto, E. A., D. Perić, and D. R.J. Owen (2008). *Computational Methods for Plasticity: Theory and Applications*, pp. 1–791. ISBN: 9780470694527. DOI: 10.1002/9780470694626.

Delprete, Cristiana and Raffaella Sesana (2014). "Experimental characterization of a Si-Mo-Cr ductile cast iron". In: *Materials and Design* 57, pp. 528–537. ISSN: 18734197. DOI: 10.1016/j.matdes.2014.01.002. URL: http://dx.doi.org/10.1016/j.matdes.2014.01.002.

Drago, Anthony and Marek Jerzy Pindera (2007). "Micro-macromechanical analysis of heterogeneous materials: Macroscopically homogeneous vs periodic microstructures". In: *Composites Science and Technology* 67.6, pp. 1243–1263. ISSN: 02663538. DOI: 10.1016/j.compscitech.2006.02.031.

Drucker, D . C . and W . Prager (1952). "SOIL MECHANICS AND PLASTIC ANALYSIS OR LIMIT DESIGN". In: *Quarterly of Applied Mathematics* 10.2, pp. 157–165. URL: http://www.jstor.org/stable/43633942.

Ductile Iron Society (1990). *Ductile Iron Data for Design Engineers*. URL: https://www.ductile.org/ductile-iron-data/ (visited on 10/13/2021).

Esposito, Luca and Nicola Bonora (2011). "A primary creep model for Class M materials". In: *Materials Science and Engineering A* 528.16-17, pp. 5496–5501. ISSN: 09215093. DOI: 10.1016/j.msea.2011.03.069. URL: http://dx.doi.org/10.1016/j.msea.2011.03.069.

Evans, W. J. and G. F. Harrison (1976). "The development of a universal equation for secondary creep rates in pure metals and engineering alloys". In: *Metal Science* 10.9, pp. 307–313. ISSN: 03063453. DOI: 10.1179/msc.1976.10.9.307.

Frost, H. J. and M. F. Ashby (1982). *Deformation-mechanism maps : the plasticity and creep of metals and ceramics*. 1st ed. Oxford [Oxfordshire] ;;New York: Pergamon Press, p. 166. ISBN: 9780080293387.

Fukuhara, Mikio and Asao Sanpei (1993). "Elastic Moduli and Internal Friction of Low Carbon and Stainless Steels as a Function of Temperature". In: *Isij International* 33.4, pp. 508–512. ISSN: 09151559. DOI: 10.2355/isijinternational.33.508.

González-Martínez, Rodolfo et al. (2018). "Effects of high silicon contents on graphite morphology and room temperature mechanical properties of as-cast ferritic ductile cast irons. Part I – Microstructure". In: *Materials Science and Engineering A* 712, pp. 794–802. ISSN: 09215093. DOI: 10.1016/j.msea.2017.11.050.

Grimvall, G. (1997). "Cast Iron as a Composite: Conductivities and Elastic Properties". In: *Advanced Materials Research* 4-5, pp. 31–46. DOI: 10.4028/www.scientific.net/amr.4-5.31.

Hervas, Isabel (2013). "Contribution à l'étude des mécanismes d'endommagement des fontes ferritiques à graphite sphéroïdal : influence de la température, du trajet de chargement et rôle des interfaces nodules / matrice". PhD thesis. URL: http://www.theses.fr/2013CAEN2069.

Hervas, Isabel, Mohamed Ben Bettaieb, and Eric Hug (2013). *Damage mechanisms evolution of ductile cast irons under thermomechanical loadings*. Tech. rep., pp. 23–32.

Hervas, Isabel, Anthony Thuault, and Eric Hug (2015). "Damage analysis of a ferritic SiMo ductile cast iron submitted to tension and compression loadings in temperature". In: *Metals* 5.4, pp. 2351–2369. ISSN: 20754701. DOI: 10.3390/met5042351.

Hervas, Isabel et al. (2013). "Graphite nodule morphology as an indicator of the local complex strain state in ductile cast iron". In: *Materials and Design* 52, pp. 524–532. ISSN: 18734197. DOI: 10.1016/j.matdes.2013.05.078.

Hill, R. (1963). "Elastic properties of reinforced solids: Some theoretical principles". In: *Journal of the Mechanics and Physics of Solids* 11.5, pp. 357–372. ISSN: 00225096. DOI: 10.1016/0022-5096(63)90036-X.

Hori, Muneo and Sia Nemat-Nasser (1999). "On two micromechanics theories for determining micro-macro relations in heterogeneous solids". In: *Mechanics of Materials* 31.10, pp. 667–682. ISSN: 01676636. DOI: 10.1016/S0167-6636(99)00020-4.

H.T. Angus (1976). *Cast Iron: Physical and Engineering Properties*. Elsevier. DOI: 10.1016/c2013-0-01035-3.

Hug, E. et al. (2009). "Application of the Monkman-Grant law to the creep fracture of nodular cast irons with various matrix compositions and structures". In: *Materials Science and Engineering A* 518.1-2, pp. 65–75. ISSN: 09215093. DOI: 10.1016/j.msea.2009.04.020.

Hull, F. C. et al. (1987). "Effect of composition on thermal expansion of alloys used in power generation". In: *Journal of Materials Engineering* 9.1, pp. 81–92. ISSN: 09317058. DOI: 10.1007/BF02833790.

Iannitti, G. et al. (2017). "Micromechanical modelling of constitutive behavior of austempered ductile iron (ADI) at high strain rate". In: *Theoretical and Applied Fracture Mechanics*. ISSN: 01678442. DOI: 10.1016/j.tafmec.2017.05.007.

J. Blau, Peter (1992). "Static and kinetic friction coefficients for selected materials". In: *Metals Handbook vol 18-Friction, lubrification, and wear technology*. ASM International- The Materials Information Company, pp. 112–122. DOI: 10.1007/978-0-387-92897-5_724.

Kaibyshev, R. and I. Kazakulov (2004). "Deformation behavior of Fe - 3Si steel". In: *Materials Science and Technology* 20.2, pp. 221–228. ISSN: 02670836. DOI: 10.1179/026708304225010415.

Kaufman, L. and H. Bernstein (1970). *Computer calculation of phase diagrams. With special reference to refractory metals*. Vol. 4. New York: Academic Press Inc, p. 344. ISBN: 0-12-402050-X. URL: http://inis.iaea.org/Search/search.aspx?orig_q=RN:2004171.

Keough, J. R., K. L. Hayrynen, and G. L. Pioszak (2010). "Designing with Austempered Ductile Iron (ADI)". In: *Trans. Am. Foundry Soc.* Pp. 503–517.

Kohout, Jan (2001). "A simple relation for deviation of grey and nodular cast irons from Hooke's law". In: *Materials Science and Engineering A* 313.1-2, pp. 16–23. ISSN: 09215093. DOI: 10.1016/S0921-5093(01)01145-5.

Krasowsky, A. J., I. V. Kramarenko, and V. V. Kalaida (1987). "FRACTURE TOUGHNESS OF NODULAR GRAPHITE CAST IRONS UNDER STATIC, IMPACT AND CYCLIC LOADING". In: *Fatigue & Fracture of Engineering Materials & Structures* 10.3, pp. 223–237. ISSN: 1460-2695. DOI: 10.1111/J.1460-2695.1987.TB00480.X. URL: https://onlinelibrary.wiley.com/doi/full/10.1111/j.1460-2695.1987.tb00480.xhttps://onlinelibrary.wiley.com/doi/abs/10.1111/j.1460-2695.1987.tb00480.xhttps://onlinelibrary.wiley.com/doi/10.1111/j.1460-2695.1987.tb00480.x.

Kuna, M. and D. Z. Sun (1996). "Three-dimensional cell model analyses of void growth in ductile materials". In: *International Journal of Fracture* 81.3, pp. 235–258. ISSN: 03769429. DOI: 10.1007/BF00039573.

Lagneborg, R. and B. Bergman (1976). "The stress/creep rate behaviour of precipitation-hardened alloys". In: *Metal Science* 10.1, pp. 20–28. ISSN: 03063453. DOI: 10.1179/030634576790431462.

Levine, Lyle E., Chukwudi Okoro, and Ruqing Xu (2015). "Full elastic strain and stress tensor measurements from individual dislocation cells in copper through-Si vias". In: *urn:issn:2052-2525* 2.6, pp. 635–642. ISSN: 2052-2525. DOI: 10.1107/S2052252515015031. URL: //scripts.iucr.org/cgi-bin/paper?hf5294.

Li, Shuguang and Elena Sitnikova (2019). "Representative volume elements and unit cells: Concepts, theory, applications and implementation". In: *Representative Volume Elements and Unit Cells: Concepts, Theory, Applications and Implementation*, pp. 1–468. DOI: 10.1016/C2017-0-03559-0.

Lund, R. W. and W. D. Nix (1976). "High temperature creep of Ni-20Cr-2ThO2 single crystals". In: *Acta Metallurgica* 24.5, pp. 469–481. ISSN: 0001-6160. DOI: 10.1016/0001-6160(76)90068-7.

Madelung, O., ed. (1990). *Diffusion in Solid Metals and Alloys*. Vol. 26. Berlin, Germany: Springer-Verlag. DOI: 10.1007/B37801.

Mohamed, F. A., K. T Park, and E. J. Lavernia (1992). "Creep behavior of discontinuous SiC-Al composites". In: *Materials Science and Engineering: A* 150.1, pp. 21–35. ISSN: 09215093.

MSC MARC Vol. A (2019). *MSC Marc Volume A: Theory and User Information*. MSC Software Corporation. URL: www.mscsoftware.com.

Mukherjee, A K, J E Bird, and J E Dorn (1968). *Experimental correlations for high-temperature creep*. Tech. rep. Berkeley, California: University of California, Lawrence Berkeley National Laboratory.

Mukherjee, Krishnendu et al. (2017). "Graphite nodules in fatigue-tested cast iron characterized in 2D and 3D". In: *Materials Characterization* 129.August 2016, pp. 169–178. ISSN: 10445803. DOI: 10.1016/j.matchar.2017.04.024. URL: http://dx.doi.org/10.1016/j.matchar.2017.04.024.

Nelson, J. B. and D. P. Riley (1945). "The thermal expansion of graphite from 15°c. to 800°c.: Part I. Experimental". In: *Proceedings of the Physical Society* 57.6, pp. 477–486. ISSN: 09595309. DOI: 10.1088/0959-5309/57/6/303.

Parker, J. D. and B. Wilshire (1975). "The Effect of a Dispersion of Cobalt Particles on High-Temperature Creep of Copper". In: *Metal Science* 9.1, pp. 248–252. ISSN: 03063453. DOI: 10.1179/030634575790445053.

Pereira, Andre et al. (2018). "Estimating the effective elastic parameters of nodular cast iron from micro-tomographic imaging and multiscale finite elements: Comparison between numerical and experimental results". In: *Metals* 8.9. ISSN: 20754701. DOI: 10.3390/met8090695.

Pierre M. Suquet (1987). "Elements of homogenization theory for inelastic solid mechanics". In: *Homogenization Techniques for Composite Media*. Ed. by Sanchez-Palencia E. and Zaoui A. Berlin, Heidelberg.: Springer. Chap. 4, pp. 193–278. DOI: 10.1007/3-540-17616-0.

Pradhan, S. K. et al. (2009). "Mechanical properties of graphite flakes and spherulites measured by nanoindentation". In: *Carbon* 47.9, pp. 2290–2292. ISSN: 00086223. DOI: 10.1016/j.carbon.2009.04.024. URL: http://dx.doi.org/10.1016/j.carbon.2009.04.024.

Riley, DP (1945). "The thermal expansion of graphite: part II. Theoretical". In: *Proceedings of the Physical Society* 57, pp. 486–95.

Ruggiero, Andrew et al. (2018). "ADI 1050-6 mechanical behavior at different strain rates and temperatures". In: *Materials Science Forum*. Vol. 925 MSF. Trans Tech Publications Ltd, pp. 196–202. ISBN: 9783035710557. DOI: 10.4028/www.scientific.net/MSF.925.196. URL: www.scientific.net/MSF.925.196.

Saunders, N. et al. (2003). "Using JMatPro to model materials properties and behavior". In: *Jom* 55.12, pp. 60–65. ISSN: 10474838. DOI: 10.1007/s11837-003-0013-2.

Sherby, Oleg D. and Peter M. Burke (1968). "Mechanical behavior of crystalline solids at elevated temperature". In: *Progress in Materials Science* 13.C, pp. 323–390. ISSN: 00796425. DOI: 10.1016/0079-6425(68)90024-8.

Speich, G. R., A. J. Schwoeble, and B. M. Kapadia (1980). "Elastic moduli of gray and nodular cast iron". In: *Journal of Applied Mechanics, Transactions ASME* 47.4, pp. 821–826. ISSN: 15289036. DOI: 10.1115/1.3153797.

Stang, R. G., W. D. Nix, and C. R. Barrett (1973). "High temperature creep in Fe-3 pct Si". In: *Metallurgical Transactions* 4.7, pp. 1695–1699. ISSN: 03602133. DOI: 10.1007/BF02666198.

— (1975). "The influence of subgrain boundaries on the rate controlling creep processes in Fe-3 Pct Si". In: *Metallurgical Transactions A* 6.11, pp. 2065–2071. ISSN: 10735623. DOI: 10.1007/BF03161832.

Steglich, D. and W. Brocks (1997). "Micromechanical modelling of the behaviour of ductile materials including particles". In: *Computational Materials Science* 9.1-2, pp. 7–17. ISSN: 09270256. DOI: 10.1016/s0927-0256(97)00053-0.

— (1998). "Micromechanical modelling of damage and fracture of ductile materials". In: *Fatigue and Fracture of Engineering Materials and Structures* 21.10, pp. 1175–1188. ISSN: 8756758X. DOI: 10.1046/j.1460-2695.1998.00078.x.

Sun, C. T. and R. S. Vaidya (1996). "Prediction of composite properties from a representative volume element". In: *Composites Science and Technology* 56.2, pp. 171–179. ISSN: 02663538. DOI: 10.1016/0266-3538(95)00141-7.

Tarasov, Boris and Yves Potvin (2013). "Universal criteria for rock brittleness estimation under triaxial compression". In: *International Journal of Rock Mechanics and Mining Sciences* 59, pp. 57–69. ISSN: 13651609. DOI: 10.1016/j.ijrmms.2012.12.011. URL: http://dx.doi.org/10.1016/j.ijrmms.2012.12.011.

Tian, Wenlong et al. (2019). "Periodic boundary condition and its numerical implementation algorithm for the evaluation of effective mechanical properties of the composites with complicated micro-structures". In: *Composites Part B: Engineering* 162.June 2018, pp. 1–10. ISSN: 13598368. DOI: 10.1016/j.compositesb.2018.10.053. URL: https://doi.org/10.1016/j.compositesb.2018.10.053.

Vander Voort, George F. and Buehler Ltd. (2004). *Metallographic Techniques for Tool Steels*. Vol. 9. ASM International, pp. 644–669. ISBN: 978-0-87170-706-2. URL: https://app-knovel-com.proxy.lib.uwaterloo.ca/web/view/khtml/show.v/rcid:kpASMHVMM1/cid:kt007O80Y6/viewerType:khtml/root_slug:44-metallographic-techniques-for-tool-steels/url_slug:asm-handbo-metallographic-2?b-toc-cid=kpASMHVMM1\&b-toc-title=ASMHandbook%252.

Yi, Yanan et al. (2020). "Investigating the effects of confining pressure on graphite material failure modes and strength criteria". In: *Nuclear Engineering and Technology* 52.7, pp. 1571–1578. ISSN: 2234358X. DOI: 10.1016/j.net.2019.12.005.

You, Mingqing (2010). "Mechanical characteristics of the exponential strength criterion under conventional triaxial stresses". In: *International Journal of Rock Mechanics and Mining Sciences* 47.2, pp. 195–204. ISSN: 13651609. DOI: 10.1016/j.ijrmms.2009.12.006. URL: http://dx.doi.org/10.1016/j.ijrmms.2009.12.006.

Zanardi, Franco, Carlo Mapelli, and Silvia Barella (2020). "Reclassification of Spheroidal Graphite Ductile Cast Irons Grades According to Design Needs". In: *International Journal of Metalcasting* 14.3, pp. 622–655. ISSN: 21633193. DOI: 10.1007/S40962-020-00454-X/FIGURES/13. URL: https://link.springer.com/article/10.1007/s40962-020-00454-x.

Zanardi, Franco et al. (2017). "A contribution to new material standards for ductile irons and austempered ductile irons". In: *International Journal of Metalcasting* 11.1, pp. 136–147. ISSN: 19395981. DOI: 10.1007/S40962-016-0095-6/FIGURES/7. URL: https://link.springer.com/article/10.1007/s40962-016-0095-6.

Zhang, Y. B. et al. (2016). "Three-dimensional local residual stress and orientation gradients near graphite nodules in ductile cast iron". In: *Acta Materialia* 121, pp. 173–180. ISSN: 13596454. DOI: 10.1016/j.actamat.2016.09.009. URL: http://dx.doi.org/10.1016/j.actamat.2016.09.009.

Zhang, Y. B. et al. (2019). "Microstructure and residual elastic strain at graphite nodules in ductile cast iron analyzed by synchrotron X-ray microdiffraction". In: *Acta Materialia* 167, pp. 221–230. ISSN: 1359-6454. DOI: 10.1016/J.ACTAMAT.2019.01.038.